Supramolecular Functional Materials: Teslaphoresis for Achieving Anisotropy and the Effect of Perfluorinated Side Chain Length in Xerogels

Inaugural Dissertation
to obtain the academic degree of
Doctor rerum naturalium / Dr. rer. nat.

submitted by
Tuğrul KAYNAK

to the Department of
Biology, Chemistry, Pharmacy
of Freie Universität Berlin

Berlin, 2021

Declaration

The research presented within this thesis was carried out under the supervision of Prof. Dr. Christoph A. Schalley at the Department of Biology, Chemistry and Pharmacy of Freie Universität Berlin in the time between September 2016 and January 2021.

1st reviewer: Prof. Dr. Christoph A. Schalley
2nd reviewer: Prof. Dr. Rainer Haag

Date of defense: March 10, 2021

I hereby affirm in lieu of oath that I have prepared the dissertation entitled "Supramolecular Functional Materials: Teslaphoresis for Achieving Anisotropy and the Effect of Perfluorinated Side Chain Length in Xerogels" independently and without the help of any impermissible resources. All citations are marked as such. This thesis has not been accepted in any previous doctorate degree procedure nor at any other department or university.

Berlin, 21st January 2021

Tuğrul Kaynak

Acknowledgments

First and foremost, I would like to thank Prof. Christoph Schalley for accepting me into his research group and giving me the opportunity to do this work. The trust that is put in the PhD students and freedom in research makes it possible to explore topics that are off the beaten track.

For taking over the role of second referee, I would like to thank Prof. Rainer Haag very much.

For the great collegial interaction and friendships formed, I thank the current and former members of the AG Schalley. Thanks to Marius Gaedke and Henrik Hupatz for the synthesis of the **NDI-C8**, which was the first own compound responding to the electric field of the Tesla coil. I thank Henrik Hupatz, Chih-Wei "Wilber" Chu and Daniel Stares for helping me correct the thesis. I thank Janos Wasternack for fruitful scientific discussions. Big thanks to Stefan Schoder for being the best lab buddy ever. And I thank the other members of the workgroup for the good times shared and stimulating conversations.

I am very grateful to Pin-Wei Lee. During her research internship and master's thesis, she synthesized the **CF*n*** compounds, assembled and programmed the morphology evolution analysis (MEA), and invented the terms "urban" and "rural" for the differently dense "populated" areas on the surfaces. Without her, this work would be lacking.

Marius Kirsch I thank for the almost complete synthesis of **5TG** during his internship.

I thank the members of the Biosupramol core facility for the acquisition of NMR and mass spectra. I thank the electron microscopy department, namely Andrea Schulz, Anke Schindler, Thorren Gimm and Prof. Christoph Böttcher for the introduction into electron microscopy, advice and the sputtering of the samples.

Thanks to Ievgen Donskyi and Robert Schusterbauer for the synthesis of the CNTs with perfluorinated side chains, even if, for timing reasons, the research could not be further extended.

To Prof. Franziska Emmerling I owe the powder diffractogram of the **NDI-C8** needles and the calculation of the crystallinities of **CF6** and **CF7**. I am thankful for the attempt to calculate the structure from the surface diffractogram of **CF6**.

I thank Thien Ngo for creating the opportunity to work with him two times at the National Institute for Materials Science in Tsukuba, Japan, and for the work that was done together on the Tesla coils. I thank Prof. Ariga for allowing me into his group on the first visit and Prof. Yoshikawa on the second visit. I thank the members of those two groups for their hospitality and their help. I owe my gaijin coffee group and my fellow interns an unforgettable time.

I thank Moritz Morcher for his valuable advice when building the Tesla coils and the fabrication of the antenna of the second model of the Tesla coil.

For the financing of the second half of my thesis I am grateful to the CRC 1349 and the people involved.

Last, but not least, I thank my partner for the scientific discussions and for bearing with me through the stressful phase of thesis writing. And I thank my study buddies for the great times and the fast path when needing help from other sections of the institute.

Abstract

The bottom-up fabrication of coatings consisting of supramolecular compounds—while inexpensive and facile—poses several challenges.

One challenge concerns the creation of anisotropic properties. To provide a directionality in the structures, the utilization of recently developed teslaphoresis is proposed. The high voltage of a TESLA coil generates an alternating electric field that has already been shown to cause aggregation of carbon nanotubes in a directional manner.

The second challenge is the prediction of the surface morphologies of coated supramolecular compounds. This makes empirical studies with slight variation in molecular structure necessary, to generate knowledge for better understanding of the impact of single motifs on the overall aggregation of compounds.

In this work, the assembly of a TESLA coil for utilization in a laboratory setting is demonstrated. Limitations of teslaphoresis are shown and the scope advanced from the sole use of carbon nanotubes to a compound based on naphthalene diimide. This compound precipitates in either spherical or needle-shaped aggregates. If drop-cast in the electric field of the Tesla coil, the material either aggregates or orientates parallel to the direction of the electric field. The prevalent orientation is determined by computational methods. The results advance the utilization of teslaphoresis for the achievement of anisotropic surface coatings consisting of supramolecular aggregators.

Additionally, the impact of the side chain length of low molecular weight gelators with perfluorinated side chains is investigated. The compounds consist of a cyclohexyl diamide core with perfluoroalkyl chains of different lengths. When the substances are drop-cast upon glass surfaces, a variety of different morphologies are observed. For quantification of the different resulting stabilities, an apparatus for repeatable water rinsing is demonstrated. Utilizing the increasing opacity of thicker surfaces, a computational method to estimate changes in surface thickness by evaluation of pixel brightness is shown. With this new method and the evaluation of changes in contact angles, coating weight and other parameters, the respective stabilities on the surface depending on the side chain length are reported.

Kurzzusammenfassung

Die Bottom-up-Fertigung von Beschichtungen aus supramolekularen Verbindungen ist zwar kostengünstig und einfach, birgt aber einige Herausforderungen.

Eine dieser Herausforderungen betrifft die Erzeugung anisotroper Eigenschaften. Um eine Richtungsabhängigkeit in den Strukturen zu erzeugen, wird die Nutzung der kürzlich entwickelten Teslaphorese vorgeschlagen. Die hohe oszillierende Spannung einer Teslaspule erzeugt ein elektrisches Wechselfeld, das erwiesenermaßen bereits Kohlenstoffnanoröhren gerichtet aggregieren ließ.

Die zweite Herausforderung ist die Vorhersage der Oberflächenmorphologien von supramolekularen Beschichtungen. Dies macht empirische Studien mit leichten Variationen in der Molekülstruktur notwendig, um Erkenntnisse für ein besseres Verständnis des Einflusses einzelner Motive auf die Gesamtaggregation von Verbindungen zu gewinnen.

In dieser Arbeit wird der Aufbau einer Teslaspule für den Einsatz im Labor vorgestellt. Einige Grenzen der Teslaphorese werden aufgezeigt und der Anwendungsbereich von der ausschließlichen Nutzung von Kohlenstoffnanoröhren um eine Verbindung auf Basis von Naphthalindiimid erweitert. Diese Verbindung fällt entweder in kugel- oder nadelförmigen Aggregaten aus. Wird sie im elektrischen Feld der Teslaspule auf eine Oberfläche aufgetropft, entsteht eine Aggregation oder Orientierung parallel zur Richtung des elektrischen Feldes. Die vorherrschende Orientierung wird durch computergestützte Methoden bestimmt. Die Ergebnisse entwickeln den Einsatz der Teslaphorese für anisotrope Oberflächenbeschichtungen aus supramolekularen Aggregaten weiter.

Zusätzlich wird der Einfluss der Seitenkettenlänge von niedermolekularen Gelatoren mit perfluorierten Seitenketten untersucht. Die Verbindungen bestehen aus einem Cyclohexyldiamid-Kern, substituiert mit unterschiedlich langen Perfluoralkyl-Ketten. Wenn die Substanz auf Glasoberflächen getropft wird, entstehen verschiedene Morphologien. Zur Quantifizierung der daraus resultierenden unterschiedlichen Stabilitäten wird eine Apparatur zum reproduzierbaren Spülen mit Wasser vorgestellt. Unter Ausnutzung der abnehmenden Transparenz dickerer Oberflächen wird eine rechnerische Methode zur Abschätzung von Änderungen der Oberflächendicke durch Auswertung der Pixelhelligkeit beschrieben. Mit Hilfe dieser neuen Methode und durch Auswertung von Änderungen der Kontaktwinkel, Gewicht der Beschichtungen und anderer Parameter wird die jeweilige Stabilität auf der Oberfläche dargelegt.

Abbreviations

AC	alternating current
BOC	*tert*-butyloxycarbonyl
CA	contact angle
CA_{max}	advancing contact angle
CA_{min}	receding contact angle
CAH	contact angle hysteresis
CDI	1,1′-carbonyldiimidazole
CNT	carbon nanotube
DACH	(±)-*trans*-diaminocyclohexane
DC	direct current
DCE	1,2-dichloroethane
DCM	dichloromethane
Et_2O	diethyl ether
DMF	dimethylformamide
DPTS	4-(*N*,*N*′-dimethylamino)pyridinium-4-toluenesulfonate
EDCl	*N*-ethyl-*N*′-(3-dimethylaminopropyl)carbodiimide hydrochloride
H-bond	hydrogen bond
HFB	hexafluorobenzene
HSB	hue, saturation and brightness
HV	high vacuum
IPA	2-propanol
IUPAC	International Union of Pure and Applied Chemistry
LMWG	low molecular weight gelator
MEA	morphology evolution analysis
MeCN	acetonitrile
MeOH	methanol
NDI	naphthalene diimide

NEt_3	triethylamine
px	pixel
r.t.	room temperature
SD	standard deviation
SEM	scanning electron microscopy/microscope
SCXRD	single crystal X-ray diffraction
SXRD	surface X-ray diffraction
σ	Gaussian window
TA	tilting angle
TC	TESLA coil
TFA	trifluoroacetic acid
THF	tetrahydrofurane
TLC	thin-layer chromatography
XRPD	X-ray powder diffraction

Contents

1 Introduction

In natural materials and living beings, the relatively weak supramolecular modes of binding are strongly represented. While the weak binding seems like a disadvantage at first, it creates reversibility and thus enables error correction. The dynamics of back and forth reactions are needed to create adaptive and self-repairing systems by reorganization of the individual building blocks. Natural selection over millions of years has resulted in highly complex and selective complexes. These complexes serve as inspiration for supramolecular chemists to adapt the same strategies with simplified systems—ideally within less than millions of years.

Excellent adaptation of organisms to different niches has produced many examples for functional materials. A property often copied from nature is (super-)hydrophobicity, with the leaf of the lotus plant (*Nelumbo nucifera*) being one of the most prominent representatives.[1] This plant, namesake of the lotus effect, is a prime example of water repellency. Droplets on the leaf's surface are almost spherical, and roll off the surface at even the slightest tilt. This phenomenon evolved because the droplets remove dirt from the leaf, allowing for a cleaner surface and more efficient photosynthesis. In detail, this effect arises from microscopic epidermal bumps ("papillae"), further covered with nanoscopic wax protrusions. This hierarchical structure leads to the necessary roughness and is imitated by scientists with the aim of creating superhydrophobic surfaces.[2]

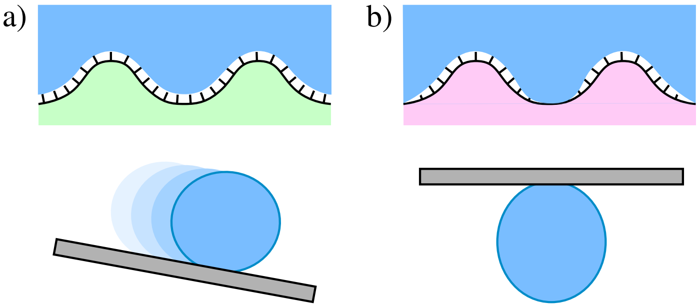

Figure 1.1: Illustration showing (a) the principle of a lotus leaf, with nanoprotrusions on top of micropapillae. Droplets roll off the surface. (b) Rose petals have hydrophilic gaps in between the papillae, making droplets stick even on a inverted surface.

The lotus leaf repels water into arbitrary directions; the surface structure is isotropic. There are other examples where the anisotropy—*i.e.*, the directionality—of surfaces plays a crucial role. The rice leaf (*Oryza sativa*) has a surface resembling that of a lotus leaf but the structure is quasi one-dimensional, allowing water to roll off selectively down the long side of the leaf.[3] This arguably allows for extended contact of the water droplet with the surface and more efficient cleaning of the leaves.

Another example exhibits apparent hydrophobicity, but on closer inspection shows another *modus operandi*. Rose petals show high water contact angles as well, but upon tilting of the surface, do not roll off if the droplet size and therefore the gravitational effect is small.[4] This phenomenon is called the rose petal effect and emerges from a different surface structure. The surface of rose petals is covered in water repelling structures as well, but these are interrupted by areas of hydrophilicity.[5] This leads to the droplet exhibiting high contact angles while simultaneously staying anchored to the hydrophilic areas.

The examples discussed above are attractive to emulate synthetically. When mimicking structures with the nature as template, there are two distinct approaches. Structures can be created top-down, meaning that the desired shapes are worked into the surface directly, for example by molding, etching or abrasion methods. Alternatively, there is the bottom-up methodology. In this case, the creation of patterns is an emerging feature of the interplay of single compounds. By self-assembly and self-organization phenomena the molecules aggregate, with different binding motifs creating different structures. This approach is more empirical, as the initial prediction of the result is practically impossible. The aim is the tailoring of simple molecules and their environments to enable the fabrication of desired aggregates. When the ideal conditions are finally determined, the process is cheaper and instrumentally much easier than top-down manufacturing.

In this work, the bottom-up fabrication of functional surfaces will be presented. For achieving anisotropic surfaces, an apparatus invented over a decade ago is put to new use. This method was only recently devised by the group of P. CHERUKURI.[6] A TESLA coil was utilized for the organization of carbon nanotubes. This technique has so far not been used in other studies concerning the achievement of anisotropic surfaces and will be tested for its functionality concerning a variety of supramolecular aggregators. The created surfaces will be analyzed with optical and electron microscopy and evaluated with computational methods of orientation analysis.

In the second half of this work, it is investigated how small changes on a molecular level translate into changes in the structures of the aggregates. This has an effect on many emerging properties, for example the hydrophobicity or the stability on surfaces. A fluorinated compound known for its supramolecular aggregation as well as for its hydrophobicity will be modified in side chain length. The hydrophobicity, structure, and stability of the resulting surfaces will then be analyzed using contact angle and microscopic measurements as well as a self-devised stability testing method, involving an indirect computational analysis of surface thicknesses.

2 Research Objectives

This work aims to advance the understanding of supramolecular surface coatings. This is addressed in two sub-projects with two different aims.

One sub-project (Chapter 5) deals with the **creation of anisotropic surface coatings**. A novel technology, **teslaphoresis**[6], has shown great potential in influencing carbon nanotubes. On the meter scale, extended linear aggregates of carbon nanotubes formed upon activation of the TESLA coil. The transfer of this technology to other materials than carbon nanotubes has not yet been completed. Therefore, the technology shall be **applied to supramolecular compounds** of other substance classes. This technology might allow for directionally functional surfaces, which exhibit properties like anisotropic wettability.

Following steps will be taken:

- Design and fabrication of a TESLA coil according to the details in the teslaphoresis publication[6].
- Reproduction of previous results to assure the functionality of the self-built system.
- Extension of this concept upon supramolecular aggregators of other substance classes, by drop-casting in the electric field of the TESLA coil.
- Evaluation of the fabricated surfaces by optical and scanning electron microscopy.
- Elucidation of the requirements for the use of this technique: compound shape, conductivity, solvent polarizability, etc.

The second sub-project (Chapter 6) investigates the **effect of the side chain length** in a certain class of supramolecular gelators, which is reported to show intriguing **water repellency** and **stability on glass surfaces**.[7] A compound, consisting of a cyclohexane core, connected via amide groups to two perfluoroheptyl chains, generated a fibrous network when drop-cast from diethyl ether (Figure 2.1). The water contact angles of those surfaces reached into the superhydrophobic region with values above 150°, and were stable against a water stream.

In order to investigate the peculiar stability of those non-polar compounds on polar glass surfaces, derivatives of varying side chain lengths between 3 and 10 fluorinated carbon atoms will be synthesized. Those compounds will be drop-cast from diethyl ether as per the original publication. The structures formed upon drop-casting will be investigated by optical and scanning electron microscopy. Their water repellent properties will be analyzed.

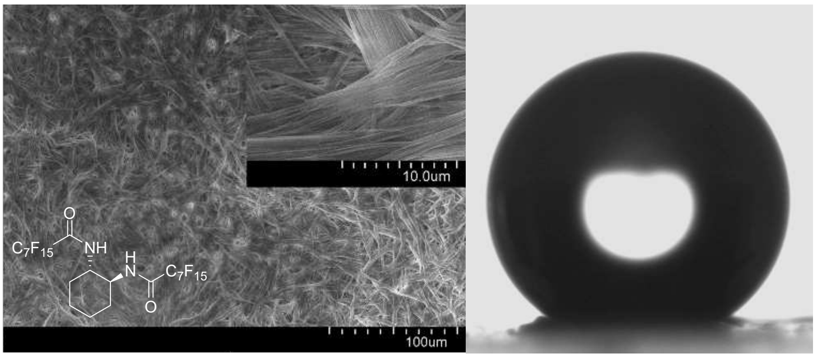

Figure 2.1: Example surface generated with drop-cast **CF7** and the resulting droplet shape.

The stability of the drop-cast surfaces will be tested by utilization of self-devised methods of abrasion and thickness quantification. A systematic effect of the side chain length will be proposed.

3 Theoretical Background

3.1 Fundamentals of Supramolecular Chemistry

3.1.1 Historical Development

Seen through the eyes of a contemporary scientist, it is incontrovertible that life is only possible because of supramolecular interactions. What possibly began as simple self-replicating molecules[8], developed into very complicated systems. Be it our skin, blood, or—the very blueprints of our bodies—the DNA, none of these would exist without the dynamic nature of the non-covalent bond. Considering that the concept is so prominent in biology, it seems surprising that the field of supramolecular chemistry emerged from the shadows of scientific indifference mere decades ago. As progress is not created from nothing, but results proceed from the advancement of previous ideas, it is difficult to define a clear starting point. Yet a significant breakthrough in supramolecular chemistry was the thesis of J.D. van der Waals[9,10], published in 1873, which is seen as the first postulation of the existence of intermolecular forces.[11] In 1894, E. Fischer published research about the enzymatic cleavage of glycosides and used the expression “lock and key” for the first time, suggesting that the shapes of two separate molecules have to complement each other for a successful reaction.[12] This principle, while invalidated in some areas, is one of the first examples where supramolecular chemistry is recognized as part of a reaction progression.[13]

Peculiarly, before modern-day supramolecular chemistry, in the 1920s, H. Staudinger proposed the existence of macromolecules, changing the paradigm from a colloidal model of polymers to a covalent one.[14] It can be argued that before the advent of macromolecules, even polymers were seen as supramolecules, without the term being defined yet.

Broad interest in non-covalent chemistry was kindled by C.J. Pedersen, upon his discovery of crown ethers in 1967.[15,16] He realized that these compounds can selectively bind specific ions. This was the first example of molecular recognition on the basis of synthetic molecules. D.J. Cram extended this concept upon a wide range of other molecules, effectively founding the discipline of host-guest chemistry, where larger “host” molecules accommodate “guests” without the need of covalent bonds.[17,18] J.-M. Lehn categorized these and other examples and coined the term “supramolecular chemistry”.[19] The three aforementioned researchers were awarded with the Nobel prize of chemistry in 1987 for the “development and use of molecules with structure-specific interactions of high selectivity”.[16,18,19]

Since then, different sub-disciplines have emerged. The use of supramolecular methods for coatings, molecular sensors, nanoreactors, catalysis, drug delivery, and many others is investigated.[20] Recently, another Nobel prize was awarded within the field of supramolecular chemistry. In 2016, J.-P. Sauvage, Sir J.F. Stoddart and B.L. Feringa were awarded the honor for “the design and synthesis of molecular machines”.[21–23]

3.1.2 The Intermolecular Bond

J.-M. Lehn described supramolecular chemistry as “chemistry beyond the molecule”, where aptly named “supermolecules” consist of two or more either covalently bound molecules or ions binding together via non-covalent interactions.[19] These interactions can be either of enthalpic nature, *e.g.,* electrostatic interactions, hydrogen bonding, π–π interactions or dispersion forces (also called London dispersion or slightly inaccurately van der Waals forces), or of an entropic nature, as seen in the hydrophobic or solvophobic effect. Normally, supramolecular interactions are weaker, they form and cleave easily, giving the resulting substances a more dynamic nature. To the layman, supramolecular chemistry is therefore often described as building block chemistry, where the individual parts can be reassembled to form a plethora of different bigger structures—most commonly a Danish manufacturer of colorful toy blocks is mentioned.

Table 3.1 shows typical binding energy ranges of exemplary interactions.[24,25] It can be seen that the strength of most of the binding modes is on average much lower than the covalent bond. Many supramolecular compounds make up for this deficit by cooperativity and the formation of several such bonds, which in sum can lead to very stable aggregations.[24]

Table 3.1: Energy ranges of typical chemical interactions:

Interaction	Strength[1] / $\mathrm{kJ\,mol^{-1}}$
Ion–ion	40–360
Ion–dipole	40–200
Dipole–dipole	4–50
Hydrogen bonding	40–120
Cation–π	4–80
π–π	0–50
Dispersion forces	0–20
Hydrophobic / solvophobic interaction	4–40
Covalent bond	160–480
Coordinative bond	80–320

[1] Ranges are given between the highest and the lowest value obtained from two sources.[24,25] Literature values were converted from $\mathrm{kcal\,mol^{-1}}$ to $\mathrm{kJ\,mol^{-1}}$ with the rounded conversion: $1.00\,\mathrm{kcal\,mol^{-1}} \,\widehat{=}\, 4.18\,\mathrm{kJ\,mol^{-1}} \approx 4.00\,\mathrm{kJ\,mol^{-1}}$.

In the present work, hydrogen bonding and π–π stacking will be of most importance. The hydrogen bond (H-bond) is one of the most ubiquitous non-covalent bonds in nature and an important factor in intermolecular interactions, for instance between amides. The bond is formed between a positively polarized hydrogen atom and an electronegative atom bearing at least one electron lone pair, commonly nitrogen, oxygen or fluorine.[26] The strongest hydrogen bonds form linear geometries, with the hydrogen atom in the middle of the two electron withdrawing atoms. Bent geometries are possible as well, but the interactions tend to be weaker with larger angles.[26]

π–π Interactions are another important binding motif for example in nucleobase–nucleobase stacking[27], appearing more often than H-bonds in DNA.[28] π–π Stacking can occur in different conformations, as shown in Figure 3.1.[29,30] The parallel face-to-face stacking mode shown in Figure 3.1 (a) is repulsive if there are two identical aromatic quadrupoles. In the case of benzene, the π cloud is the negative end of the molecular quadrupole, sandwiching the inner σ system, which is the positive component. Therefore, aromatic systems undergo changes in arrangement to compensate for the repulsion. Possible arrangements are offset face-to-face, shown in Figure 3.1 (b), or two possible orthogonal arrangements, namely edge-to-face or T-shaped (Figure 3.1 (c) left and right, respectively). Substituents on the aromatic systems can reverse the polarity of the quadrupole. A popular example is hexafluorobenzene (HFB), where the strongly electronegative fluorine substituents withdraw electron density out of the aromatic system into the σ system and therefore lead to a positive polarization of the π cloud. This in turn leads to a favored parallel face-to-face stacking conformation shown in Figure 3.1 (d). Naphthalene diimide (NDI) and perylene bisimide based compounds behave similarly to HFB in terms of their aggregation. Shown in Figure 3.1 (e) is, that although their quadrupole is geometrically different than that of HFB, the center of the molecule is the negative component of the quadrupole, allowing for parallel face-to-face stacking with benzene.[29]

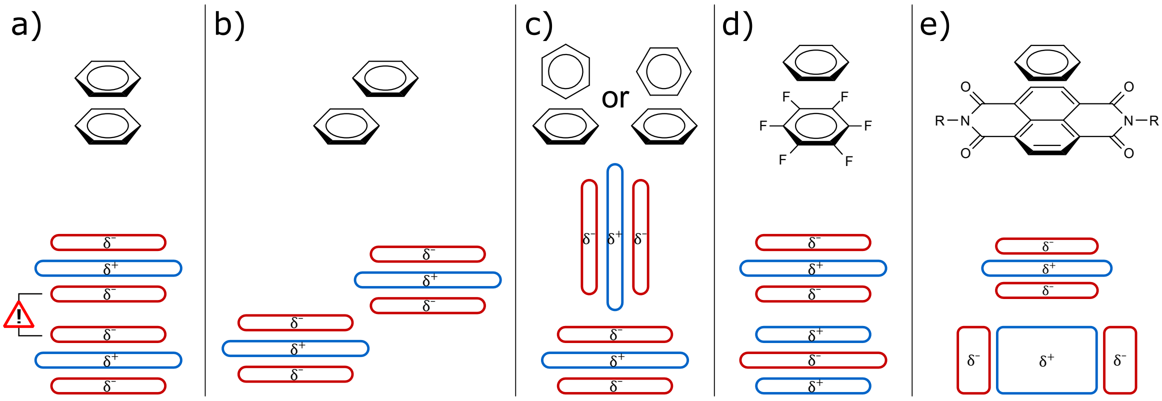

Figure 3.1: Different modes of π stacking: (a) Parallel face-to-face, disfavored with two similar quadrupoles; (b) offset face-to-face; (c) left: T-shaped, right: edge-to-face; (d) parallel face-to-face between benzene and HFB; (e) parallel face-to-face between benzene and NDI.

In larger molecules with aromatic moieties, π–π interactions, with additional other binding motifs, can lead to two different stacking categories.[31] Those two types of aggregates are classified as H- and J-aggregates/stacks, respectively. If there is other no binding interaction counteracting the repulsion between quadrupole ends of identical polarization, the compounds aggregate in a shifted fashion. This is called J-type aggregation, after its discoverer E. JELLEY. They exhibit a bathochromic shift to longer wavelengths with a narrowed band. As opposed to H-stacks, they do fluoresce almost resonantly, with a very small STOKES shift (the wavelength difference between absorbance and fluorescence).[31,32] A non-shifted face to face aggregation is called H-type aggregation. This leads to a shift of the absorption band to shorter wavelengths, the first letter of "hypsochromic" being the namesake of the class of structures. Fluorescence is strongly quenched in this type of aggregation.[33] The type of stacking changes the electronic properties as well. It was reported for a perylene bisimide derivative, which could be switched between the types of aggregation, that H-stacks offer n-type conductivity, while J-aggregates exhibit increased p-type charge carrier mobility.[34] There are also in-between states possible, commonly coined HJ-aggregates.[35]

3.1.3 Self-Assembly and Self-Organization

The organization of molecules into larger aggregates and structures can happen via two different processes, distinguishable by their energy balance. On the one hand, there is self-assembly, which denotes the pathway to lower energies, where molecules converge spontaneously and form thermodynamically more stable complexes. The process is dynamic and the product is in the global minimum of the accessible part of the potential energy landscape. Which part is accessible depends on the temperature: Higher temperature makes barriers of higher energy surmountable, effectively increasing the number of accessible states. The time frame can decide which minimum is the most populated. The structure of the resulting product is determined by the the molecular structure of the monomer and the interacting molecules, like solvents. Therefore, identical combinations lead to the same products. This makes it the archetype process of bottom-up chemistry, where modification of a small building block leads to changes in the higher structure.[36] The products are stable without energy input.

On the other hand, there is self-organization. This process is reliant on continuous energy input from outside the system in the form of thermal energy, photoexcitation or chemical energy (*e.g.,* introduction of oxidizing and reducing agents). The system is open and under constant influx; molecules aggregate into an energetically higher product while the excess energy is dissipated. Factors like the influx/dissipation ratio can alter the resulting structures massively and the whole process is far less predictable than self-assembly. Self-organized aggregates have the tendency to fall victim to entropy when said energy source is removed, and disassemble again.[37]

3.2 Hydrophobicity

3.2.1 Static Contact Angles

Information about the water repellency, or hydrophobicity, of surfaces is most commonly gained by measuring the angles of water droplets on surfaces. This is illustrated in Figure 3.2. If the angle of the droplet profile is smaller or equal to 90°, the surface is hydrophilic, if the angle is larger than 90°, it is hydrophobic. When the angle exceeds 150°, the surface is classified as superhydrophobic.

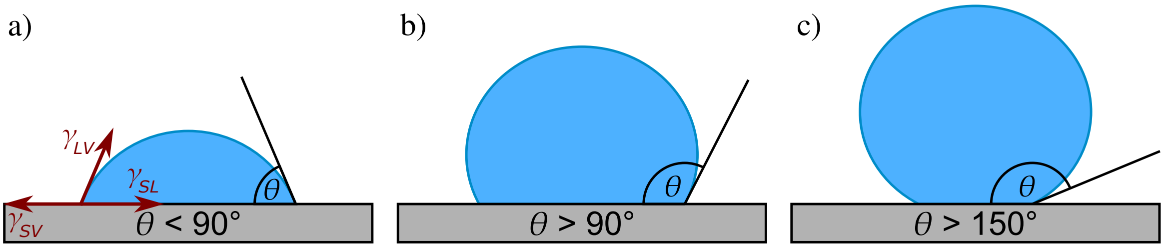

Figure 3.2: (a) A water droplet on a hydrophilic surface with the three underlying interfacial tensions represented by arrows; (b) droplet shape on a hydrophobic surface; (c) droplet shape on a superhydrophobic surface.

The droplet is shaped by the interplay of three interfacial energies, also known as interfacial tensions. These are the solid-vapor (γ_{SV}), solid-liquid (γ_{SL}) and liquid-vapor interfacial tension (γ_{LV}). The interfacial tension can be described as the energy needed to increase the interface between two adjacent phases, and therefore has the unit $\mathrm{J\,m^{-2}} = \mathrm{N\,m^{-1}}$.[38] At interfaces, molecules have fewer neighbors to interact with, resulting in a loss of energy from the incomplete occupation of binding potential. This is in part compensated by reducing the surface. The shape with the smallest surface area is the sphere, therefore, for high energy differences, the droplet becomes spherical.[39]

For ideally flat and chemically homogenous surfaces, the angle θ of the tangent through the three-component-interface is described by YOUNG's equation (3.1) for thermodynamic equilibrium.[40,41]

$$\cos\theta = \frac{\gamma_{SV} - \gamma_{SL}}{\gamma_{LV}} \tag{3.1}$$

On perfectly smooth surfaces, contact angles do not exceed 120°.[42,43] Rough surfaces behave differently and can amplify the effects of surface coatings. Droplets on rough surfaces can be described by different models, the two most popular being the WENZEL and the CASSIE-BAXTER model shown in Figure 3.3.

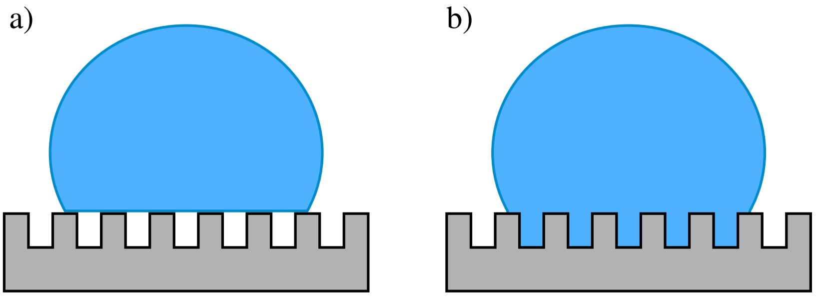

Figure 3.3: Two models describing the interactions of droplets on rough surfaces: (a) Cassie-Baxter model, (b) Wenzel model.

The Wenzel model describes the penetration state of a droplet, where it has sunk in between the asperities. For rough surfaces like these, R. Wenzel proposed adding a roughness factor r, which is the ratio of the actual surface to the geometric surface.[44] This led to a modified Young's equation (3.2).[43] Because r can never be negative, it enhances the hydrophilicity of hydrophilic surfaces, and vice versa the hydrophobicity of hydrophobic surfaces.

$$\cos\theta_W = \frac{r(\gamma_{SV} - \gamma_{SL})}{\gamma_{LV}} = r\cos\theta \tag{3.2}$$

The Cassie-Baxter model, shown in Figure 3.3 (b), describes the suspended state, where the droplet is cushioned on top of a vapor phase trapped within the solid phase underneath. The surface energy of the droplet maintains the shape and prevents it from penetrating the grooves. Because the droplet is effectively sitting on a heterogeneous surface composed of two materials, the Cassie-Baxter state is also known as the heterogeneous state.[45]

$$\cos\theta_{CB} = f_1\cos\theta_1 + f_2\cos\theta_2 \tag{3.3}$$

Equation 3.3 therefore incorporates two surface fractions, f_1 and f_2, with the respective contact angles θ_1 and θ_2. To simplify this equation, a few assumptions can be made. If the second phase is air, the contact angle to water is 180°. If f_1 is the fraction of solid that is wetted by the droplet, the remaining air fraction f_2 is $1 - f_1$. Therefore, a subscript can be omitted and f refers only to the solid. This leads to Equation 3.4.

$$\cos\theta_{CB} = f(\cos\theta + 1) - 1 \tag{3.4}$$

Fraction f denotes the fraction of solid underneath the droplet. The contact angle increases with the proportion of air underneath.

Although the Wenzel model and Cassie-Baxter model are subject to ongoing debate[46–48] and improvement[49], they are sufficient to explain the increasing hydrophobicity induced by the roughness created by fibrous coatings used in this work.

3.2.2 Dynamic Wetting Processes

Although they give a first insight about the wetting behavior, high contact angles are not the only aspect of a superhydrophobic surface. In contrast to the lotus leaf, where a slight tilting of the surface is enough for the droplets to roll off, on rose petals, they will pin to the surface and remain sessile.[5] Yet they exhibit high contact angles (CAs) in both cases. This is based on the fact that in the case of the lotus leaf, the droplet is cushioned on a continuous rough surface, while in the case of the rose petal, the droplet can interpenetrate between the structures and adhere to the surface.

These phenomena can instrumentally be differentiated by taking into account the dynamic droplet behavior. This can be achieved by tilting the surface on which the droplet sits by a certain tilting angle (TA) until the droplet rolls off. The angles of the droplet in the instance before the rolling off can be measured using video capturing. In this state, a droplet exhibits two different contact angles: an advancing contact angle ($\mathrm{CA_{max}}$) at the lower end of the droplet and a receding contact angle ($\mathrm{CA_{min}}$) at the opposite end. This is illustrated in Figure 3.4. Depicted is a surface with a sessile drop, which is tilted to an angle at which a droplet rolls off. The illustration shows the existence of two different contact angles at tilting angle α, where θ_r corresponds to $\mathrm{CA_{min}}$ and θ_a to $\mathrm{CA_{max}}$.

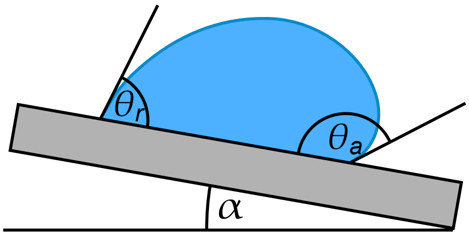

Figure 3.4: Sketch of a droplet during tilting of the surface, immediately before rolling off. $\mathrm{CA_{min}} = \theta_r$, $\mathrm{CA_{max}} = \theta_a$, TA = α.

As tilting a surface and simultaneously keeping a droplet in focus is instrumentally complicated, another method is used which emulates the behavior of a sliding droplet. This is called the “sessile drop (needle in)” method. During this process, a cannula is inserted into a sessile droplet on a surface. Liquid is then either added or removed. Figure 3.5 shows a sketch of this process if liquid is removed. The outer lines represent the droplet in its thermodynamic equilibrium. If liquid is removed, the droplet loses volume, but initially the pinning of the droplet to the surface does not change and the interface retains its area. If a certain lower limit of volume is reached, the droplet unpins and find a new minimum. Directly before that event, the CA$_{\text{min}}$ can be measured. For measurement of the CA$_{\text{max}}$, the same method is used, but liquid is added to the droplet.[50]

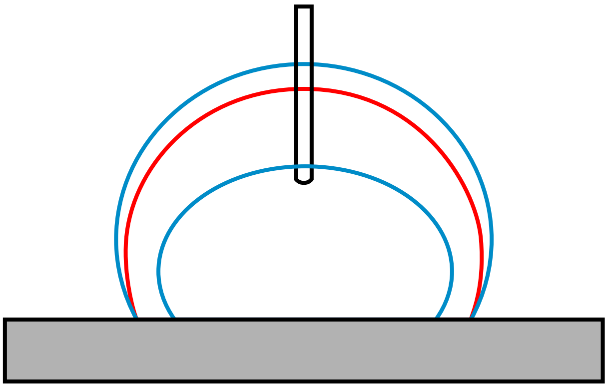

Figure 3.5: Sketch of the sessile drop (needle in) method in the process of liquid removal. The outer blue line represents thermodynamic equilibrium, the red line a metastable state reached during shrinking. Eventually the droplid unpins to reach a new thermodynamic minimum represented by the inner blue line.

3.2.3 Fitting of Droplet Shapes

For the computational fitting of droplet shapes, different methods can be used. The droplet outline can be fitted to a ellipse[51] and the angle measured at the intersection of this calculated ellipse and the baseline. With small droplet volumes, gravity has a small effect on the droplet shape, which is instead governed by interfacial tensions. This method is used in cases when there is the need for little computational effort.

A more accurate fitting method, which takes the gravitational distortion into account, is the Young-Laplace fitting (Equation 3.5).[52,53]

$$\Delta p = \gamma_{LV} \left(\frac{1}{r_1} + \frac{1}{r_2} \right) \tag{3.5}$$

At this point, the complete derivation is omitted. The Laplace pressure Δp corresponds to a change in pressure across the interface caused by surface tension. The liquid-vapor interfacial tension is represented by γ_{LV}; r_1 and r_2 denote the two radii of curvature of the rounded shape. This method is more accurate than ellipse fitting, but consumes more processing power.

3.3 Fluorous Chemistry

One method of achieving high contact angles with water is the utilization of compounds containing perfluorinated moieties.

J. Gladysz *et al.* define "fluorous" compounds as compounds based on saturated/sp^3-hybridized carbon backbones exhibiting a high degree of fluorination.[54] These fluourous compounds are often seen as a third class of compounds, alongside aqueous and organic compounds, owing to a number of differing properties. The polarity of the C-F bond is very high with a dipole moment of 1.41 Debye, compared to the dipole moment of the C-H bond with 0.40 Debye.[55] In perfluorinated compounds, these individual dipole moments cancel each other out, leading to very low to naught dipole moments. The bond lengths differ by only 27 %, with a bond length of 1.38 Å for C-F and 1.09 Å for C-H. The van der Waals radii of F and H differ by 23 % (1.20 Å and 1.47 Å, respectively).[56] These dimensions seem exceedingly low considering the 19-fold mass of the fluorine atom compared to hydrogen. Classical linear alkanes prefer a "zig-zag" conformation, resulting from the antiperiplanar conformation with dihedral angles of 180° between the C^n-C^{n+1} and C^{n+2}-C^{n+3} bonds.[57] In perfluoroalkanes, the increased volume of the fluorine atoms leads to increased steric and electrostatic repulsion of the substituents in 1,3-position and creates a helical conformation in the chain.[55] This common textbook explanation was challenged recently, as quantum mechanical calculations showed that electrostatic and steric repulsion play a surprisingly small role towards the geometry. It is stated that hyperconjugative $\sigma_{CC} \rightarrow \sigma^*_{CF}$ interactions promote the helical conformation.[58]

The low polarizability of fluorine leads to reduced dispersion interactions. The boiling points of fluorous compounds are similar to the hydrocarbons of similar chain length, but much lower when compared to molecules of similar molecular weight. Comparing CF_4 (M_W = 88 g mol^{-1}) and *n*-hexane (M_W = 86 g mol^{-1}), the boiling point of CF_4 (−128 °C) is much lower than that of *n*-hexane (69 °C).[55] Interestingly, branching only has a negligible effect on the boiling points of perfluoroalkanes.

Another phenomenon that differs between alkanes and perfluoroalkanes is the odd-even effect. It was observed in fatty acids over a hundred years ago, that the melting points do not show a linear increase, but rather a stepwise one with increasing chain length. The melting points for compounds with an even number of carbon atoms were relatively higher than those with an odd number. The same effect was proven in the homologous series of *n*-alkanes.[59] Taking into consideration the distinctive zig-zag conformation of linear alkanes, this can be explained by the more efficient packing in the solid state of chains with an even number of members and a therefore increased melting temperature. This is only pronounced in the transition from the solid phase, as the increased conformational mobility in the liquid phase negates the effect. The odd-even effect has since been shown on a variety of different properties of different compounds. For example, it influences the melting points of alkane diamides[60], the packing of alkanethiols tethered to gold surfaces[61] and their charge transport[62], polymerization behavior of diacetylene organogels[63] and others. In perfluorinated compounds, odd-even effects occur less frequently. This is due to the helical and rigid structure of the perfluoroalkyl chain, because of which the chain length has less of an influence on the packing behavior.[54]

Owing to their weak intermolecular interactions, the surface tension of liquid perfluoroalkanes is extremely low, and solid surfaces also show a very low surface energy.[55] This leads to their popular anti-wetting and anti-sticking properties, as seen for example in the commonly used poly(1,1,2,2-tetrafluoroethylene), known better as PTFE or Teflon®.

3.4 Functional Materials

3.4.1 Top-Down and Bottom-Up Methodology

To reach strong hydrophobicity, materials must meet two requirements. One one hand, the materials have to be inherently hydrophobic. However, to surpass a certain threshold of water repellency, the CASSIE-BAXTER and WENZEL models show that surface roughness is essential. There are two fundamentally different approaches to achieve rough structuring. The "top-down" approach is used to create materials from bulk or film by a variety of patterning techniques.[64] One of the most common methods is for example photolithography, and while a number of different methods exist, their unifying aspect is using incident light to create a surface structure, either by abrasion or fortification of patterns.[65] Those lithographically created surfaces can be used directly, or for example be used as templating molds to create topographical negatives out of other materials.[66]

In contrast, there is the "bottom-up" methodology. It requires careful design of small building blocks, which under controlled conditions assemble into the desired shapes. Owing to phenomena like self-assembly and self-organization, addressed in Chapter 3.1.3, the defining moieties of molecules allow for the growth of reproducible patterns, like sheets, porous coatings, rods, or fibers.[67] As the outcome is hard to predict, this methodology is inherently empirical. Interactions between molecules are very dependent on the environmental variables, like solvent, temperature, humidity, and many others. Yet, if the processes and structures are well-documented, bottom-up fabrication offers advantages. Ideally, only a small number of different substances (often only one kind of molecule and a solvent) are needed to achieve desired functionality. This can lead to reduced production costs and facile execution. Instrumentally, a wide variety methods can be used, including electrospinning[68], chemical vapor deposition[68,69], layer-by-layer deposition[70–72], dip coating[73] and spin-coating[74,75]. Arguably the most simple coating method is drop-casting[76]. Here, a solution with the coating agent is applied to a surface and the solvent left to evaporate.

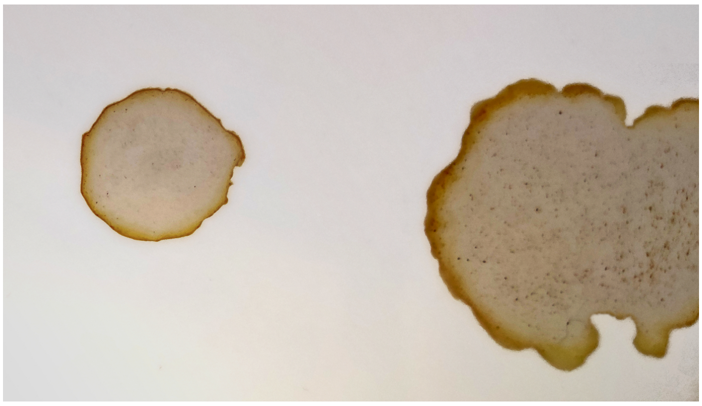

Figure 3.6: The edge of evaporated coffee spills contains more substance and is darker due to the coffee ring effect.

While facile, under some circumstances, this technique suffers from the coffee ring effect. Figure 3.6 shows an image of evaporated drops of coffee on a smooth surface. It can be seen that at the borders of the stains, the concentration of deposit is the highest. This effect is dependent on a large number of variables.[77] Simplified, it stems from the fact that at areas of the droplet with a high curvature—namely the areas close to the underlying substrate—evaporation is enhanced due to the larger vapor-liquid interface. As liquid evaporates, the volume of the droplet is decreased, but due to pinning effects, the contact line does not instantly change. Because of the drive to reduce the contact area between droplet and air, flows occur, which transport particles to the border of the droplet. When CA_{min} is reached, a re-equilibration takes place, during which the contact line recedes. The solid which is at the very border of the droplet is then exposed to the vapor phase and remains stationary. This in summary leads to the accumulation of solid at the outer rim of the drop and the distinctive ring shapes. This phenomenon is most prevalent in suspensions with microscopic spherical particles, because of their unrestrained transport. This effect can be detrimental when either a uniform coating or a visible orientation of the aggregates is intended.

3.4.2 Supramolecular Gels

A class of compounds that can be created either by covalent or supramolecular methods are gels. The IUPAC defines a gel as “non-fluid colloidal network or polymer network that is expanded throughout its whole volume by a fluid”[78]. It is a class of substances between the solid and the liquid state. A commonly cited definition was given by P.J. Flory in the 1970s, where he defined the prerequisites as a continuous structure permanent on an analytical time scale and a solid-like reaction to deformation, elastic in nature.[79,80] Gels are more specifically called organogels if the swelling liquid is an organic solvent, as opposed to hydrogels which form with water.[81] In supramolecular gels, the monomers are most commonly small molecules, which are referred to as low molecular weight gelators (LMWGs)[26] or low molecular mass organic gelators (LMOGs)[82]. In this work, the former designation is used.

These small molecules interact with each other in a variety of ways, like hydrogen bonding, π–π interactions, dispersion forces, solvophobic effects, or metal coordination.[83] These interactions lead to the formation of fibrillar networks (reminiscent of covalent polymers), which in turn can entrap solvent molecules. Gels are prepared by heating a saturated solution of the gelator in a solvent and letting it cool down to room temperature. Upon cooling of the supersaturated solution, the solid can either precipitate, crystallize, or result in a gel.

If gels are left to evaporate their solvent, the remaining structures are called xerogels.[78] Normally, those structures are collapsed compared to the swollen form, but retain their fibrous structure.

3.4.3 Fluorinated Low Molecular Weight Gelators

A foundation of this work is the leading work done by Q. Wei and C. Schlaich.[7] They utilized **CF7** to generate superhydrophobic surfaces on glass by a simple procedure. *N*,*N′*-Diperfluoroalkanoyl-1,2(*R*,*R*)-diaminocyclohexane compounds were used, shown in Figure 3.7.

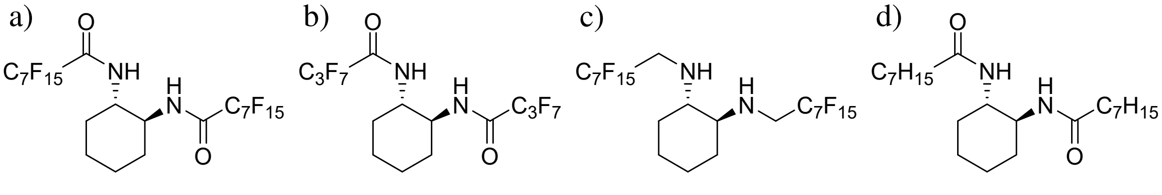

Figure 3.7: The compounds utilized in the study of Wei and Schlaich, (a) **CF7**, (b) **CF3**, those two compounds will be used in this work as well. (c) A derivative without carbonyl groups for hydrogen bonding and (d) the non-fluorinated analogon to **CF7**.

CF7 was dissolved in diethyl ether, where it created a gel. This gel was then drop-cast onto glass surfaces. After evaporation, the fibrous structure remained as a xerogel. This structure, consisting of long, fibrous aggregates, was surprisingly stable on the glass surfaces and would generate the necessary roughness for CAs over 150°. It was compared to surfaces generated similarly by utilization of **CF3**, which did not generate fibers, but shorter aggregates. Those were initially superhydrophobic as well, but easily washed off the surface. Furthermore, it was compared to surfaces drop-cast from molecules structurally related to **CF7**, but lacking the amide bonds, shown in Figure 3.7 (c). These compounds would not create fibrous coatings at all and the received surfaces were in the hydrophilic regime. If the side chains were non-fluorinated, as shown in Figure 3.7 (d), the surface was not porous, but fibrous and only slightly hydrophobic.

The **CF7** coatings were used as a basis for lubricant infusion. As shown before in the work group of J. AIZENBERG[84], they were treated with Fluorinert FC-70® (tris(perfluoropentyl)-amine), which was trapped within the fibrous networks. This created slippery surfaces with low TAs. The entrapment of the lubricant in the fibrous network led to the infusion being stable against water flow.

Extensive work on this class of compounds was carried by H. SATO and co-workers.[85–87] It should be noted, that in their work the series of compounds is numbered differently, as the carbonyl group is included in the counting. Therefore, **CF3** in this work relates to **CF4** in the work of SATO and co-workers. For easier understanding, the descriptors will be transferred to the system of the present work, which is shown in Figure 3.8.

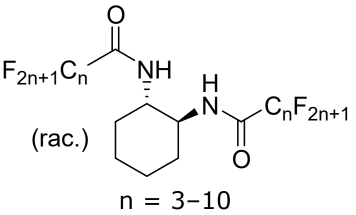

Figure 3.8: The numbering scheme used for **CF*n*** compounds in this work, ranging from three perfluorinated carbon atoms per side chain (**CF3**) to ten (**CF10**).

The research of SATO and co-workers focuses mainly on the chiral effects of enantiopure compounds. In this work, solely the racemates of the (*R*,*R*)- and (*S*,*S*)- enantiomers will be addressed. Additionally, their work included a plethora of different solvents, but not diethyl ether, which makes a direct comparison of the morphologies impossible. They speculated that there might be an odd-even effect for the critical gelation temperature of enantiopure (*R*,*R*)- or (*S*,*S*)-**CF6–CF9**. In hexafluorobenzene, the gelation temperature **CF6** was comparatively low, for **CF7** high, for **CF8** low and for **CF9** high again. In the case of the racemic compounds, there was no such effect involved. For explanation, the discovered crystal structures for racemic and (*R*,*R*)-**CF3** are used. The crystal structures show that the enantiopure **CF3** stack with their cyclohexyl moieties parallel to each other. That way, the perfluoropropyl groups are neighboring intermolecularly and interact with each other. In the case of racemic **CF3**, the molecules stacked alternatingly. That way, the fluorine chains are close to the cyclohexyl groups of the neighboring molecules and the only fluorine-fluorine interaction happens between the far ends of the chains of diagonally opposed molecules.[86] With the help of vibrational circular dichroism spectroscopy, which gives information about the conformation of the molecules in the gel phase, they induce that the same might hold true for molecules of longer side chains. They claim that for an odd-even effect to be noticeable, the perfluorinated chains need the potential to interact with each other, which is missing in the racemic compounds.

In another study, the structure of enantiopure (*R*,*R*)-**CF7** was discovered, where the cyclohexyl moieties again stack parallel.[87] The helicities of the side chains exhibit an irregularity. In the case of (*R*,*R*)-**CF7**, one chain has right handed (P) helicity, with dihedral angles of $-171°$, $-160°$, $-161°$, $-156°$, and $-149°$ along the bonds of C1–C2–C3–C4, C2–C3–C4–C5, C3–C4–C5–C6, C4–C5–C6–C7, and C5–C6–C7–C8, with C1 being part of the carbonyl group and C8 the last carbon atom of the perfluorinated chain. Surprisingly, the other perfluorinated chain exhibits pseudo-racemic hybrid right and left handed (M) helicity. The dihedral angles are $+124°$, $+159°$, $+154°$, $-150°$, and $-131°$, respectively. It can be seen that the direction of helicity shifts on C5. In between the molecules, only one carbonyl group creates hydrogen bonds with two amide groups of the same neighboring molecule.

There are no further crystal structures of compounds **CF3–CF10** available so far. The results of SATO and co-workers show that there might be odd-even-effects present, depending on the kind of aggregation. Due to the lack of crystal structures from diethyl ether, for the present work, no assumptions can be made.

3.4.4 Anisotropic Materials

There is a variety of different approaches to achieve anisotropy of surface properties. There are top-down methods like etching and lithographic methods, where the bulk material is modified directly.[88] A facile example of bulk modification is the use of diamond lapping films to scratch liquid crystal surfaces and thus achieve patterning.[89] There are mixed methods, combining properties of top-down and bottom-up methodology. For example, the surface of an elastic polymer was hardened in a uniaxially stretched state. Upon release, the material contracted and the more rigid surface formed a wavy pattern, on which hydrophobic particles were deposited.[90] This created anisotropic properties similar to the ones of the rice leaf. Methods that can be classified as bottom-up are abundant as well. Anisotropy in organogels was created by gelating under shear stress within a rheometer.[91] Cellulose nanofibrils were ordered by spraying the solution onto a surface at an oblique angle.[92] Very strong magnetic fields have been utilized, and influenced gelating materials in their directionality via their inherent diamagnetic susceptibility[93,94], the property that was used to levitate frogs[95]. Electric fields have been used to create an order in organogelators as well. For example an alternating current (AC) electric field between two gold electrodes was utilized, with a voltage of $1\ \mathrm{V\ \mu m^{-1}}$ at a frequency of 1 kHz.[96] It was shown that this causes organogel fibers to connect the two electrodes, but the technique is limited to the micrometer scale, with gaps of about 30–60 µm between the electrodes. For methods including electrical fields, this is so far the limiting factor, as (di-)electrophoretic methods are only applicable in the micrometer range.[97]

3.5 Teslaphoresis

One novel method to achieve anisotropic materials was developed in the group of P. Cherukuri.[6] It is based on the phenomenon of dielectrophoresis, where particles can become polarized and move in a nonuniform electric field. The electric fields generates charges on the interface between the substance and the solvent and exerts a force depending on that generated charge. This only occurs in inhomogeneous electric fields: The gradient is needed for a net movement on the time average, as the force on either side of the particle needs to differ. The force generated is called ponderomotive force. It is the net force that remains when most of the forces of opposing polarity have canceled each other out and is proportional to the gradient of the square of the electric field: $F_p \sim \nabla \vec{E}^2$.[98]

The principle is illustrated in Figure 3.9. Charges form in the area of the particle close to the interface. If the particle is more polarizable than the suspending medium, the net charge has the same direction as the electric field. This is shown in Figure 3.9 (a). If the particle is more weakly polarizable, seen in Figure 3.9 (b), the net charge is opposed to the electric field. This causes the effective dipole moment to be opposite as well. Close to the more concentrated charge of the pointed electrode, the electric field is stronger. Therefore the Coulomb forces are stronger in the right hand side of the pictures. This leads to the more strongly polarizable particle to move to the right, and to the more weakly polarizable particle to move to the left. Dielectrophoresis is limited to the micro- to millimeter scale, as it is only over this distance that electrodes have a kinetic effect on the particles.

Because of the aforementioned spatial restrictions, industrial application of dielectrophoresis is impractical. These limitations were overcome by utilization of a Tesla coil. This device is most commonly known as a popular exhibit in science museums, where it can create spectacular arcs of “lightning” (more precisely termed streamer discharge). It is named after its inventor, N. Tesla, who envisioned wireless energy transport with it, and in esoteric circles it is claimed to generate “free energy” from the environment. While those claims fail to be scientifically viable, the effects of the electric field on nanomaterials are very much reproducible. The group of Cherukuri chose single-walled carbon nanotubes (CNTs) for their initial study, as it is a highly polarizable material consisting of anisotropic molecules. When suspended in water with the help of one percent of the block copolymer Pluronic

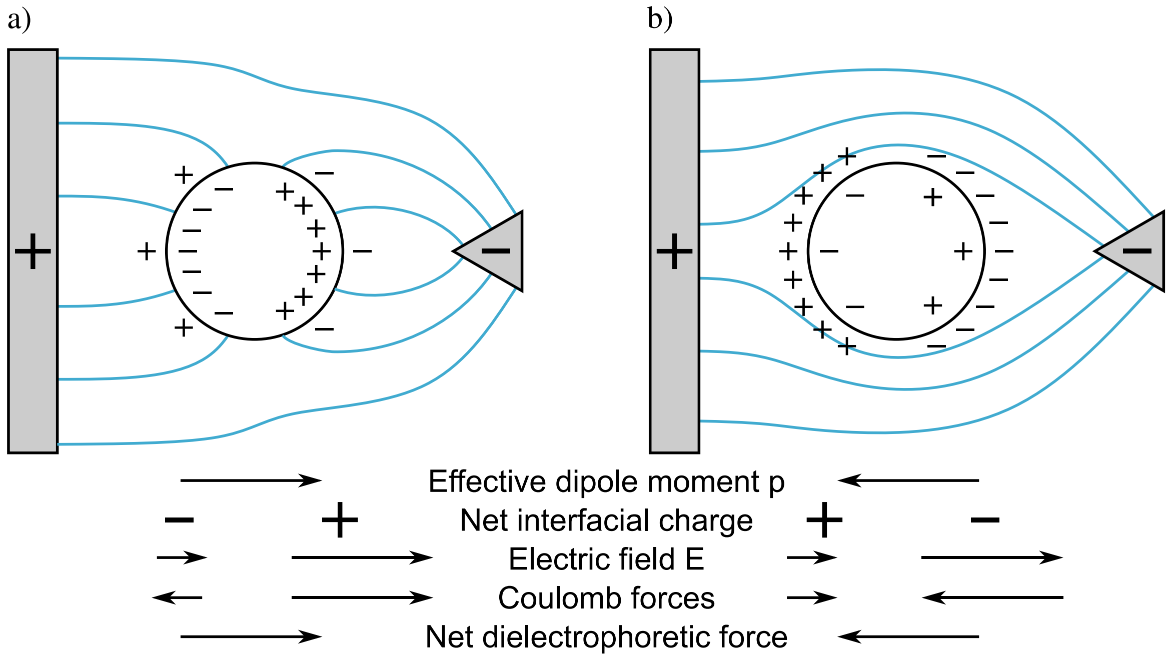

Figure 3.9: The illustrated principle of dielectrophoresis. Displayed are two cases, (a) where the particle is more polarizable than the solvent and (b) where the medium is more polarizable than the particle. The strength of the electric field and the resulting Coulomb forces in the different areas are indicated by the length of the arrows. The image is recreated from literature.[98]

F-108, the CNTs quickly assembled into elongated wires in the direction parallel to the electric field lines.

Figure 3.10 shows the working principle of an idealized LC circuit, as a basis for understanding the functioning principle of a Tesla coil. An LC circuit is a circuit consisting of an inductor (*e.g.,* a coil, abbreviated L) and a capacitor (abbreviated C). Both a capacitor and an inductor can store electric energy. The capacitor stores energy in an electric field that is generated between oppositely charged ends; an inductor stores energy in its magnetic field. An LC circuit has a certain frequency with which the energy oscillates between those two states. In the beginning (marked as state 1), the entire energy is stored in the electric field between the capacitor plates, representing the state of maximum voltage / potential energy. This voltage causes a current, which leads to discharge of the capacitor. A change in current also causes a change of the magnetic field within the inductor. Therefore, the magnetic field builds up as the electric field in the capacitor is reduced. When the capacitor is fully discharged, the magnetic field is at its maximum (state 2). Because of the inertia of such electronic systems, the flux does not stop immediately, but leads to a build-up of voltage in the capacitor, opposite to the beginning, while the magnetic field decreases again. When the capacitor is at its maximum and the magnetic field at zero again (state 3), the whole process starts in the opposite direction.[100]

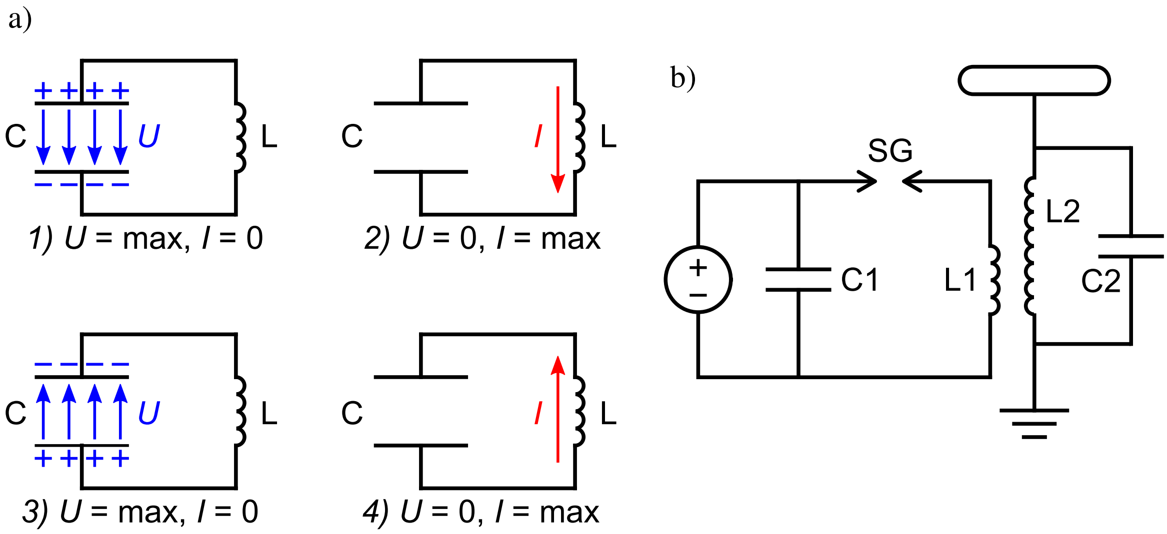

Figure 3.10: Electronic circuits showing the operating principle of a TC; C: capacitors, L: inductors, SG: spark gap. (a) The different states of an ideal LC circuit, modified from a public domain picture[99]. (b) A simplified circuit of a spark gap TC; C2 represents the capacitance originating from the windings of the second coil.

The operating principle of a TC is shown in Figure 3.10 (b). A direct current (DC) power source feeds into a capacitor C1. This increases the voltage up to a certain value, until it is high enough for a spark gap (SG) to close. This integrates the primary coil L1 into the circuit, creating an LC circuit and sending energy through the primary inductor. The primary coil is coupled to the secondary (L2) and therefore induces a current in the second circuit. In this circuit, the conditions are more intricate and deviate from secondary school physics.[101] It is based on the fact that an inductor consists of insulated wire coiled with the same regular distances between the windings. This creates a capacitance between the windings (implied with C2). Therefore, there is again a combination of capacitor and inductor, ergo a LC circuit, present. This LC circuit has a certain resonance frequency. If the resonance frequency of the first circuit and the second circuit are integer multiples of each other, this leads to constructive interference, raising the potential in the second circuit further and further. This does not correspond to the coupling of coils that is known from electrical transformers! There, the coils possess a ferromagnetic core and the quotient of the number of windings determines the output voltage. Here, the coils are coupled through air and resonance phenomena lead to the output voltage. This voltage generates an electric field emanating from the antenna of the TC. If the output voltage is strong enough, lightning-like corona discharges are created. These look similar to the closing of spark gaps. But in the case of sparks, the air along the discharge is thermally turned into plasma. In the case of corona discharge, the average temperature of the air stays mostly stable, while only a small number of molecules is ionized, allowing for the discharge.

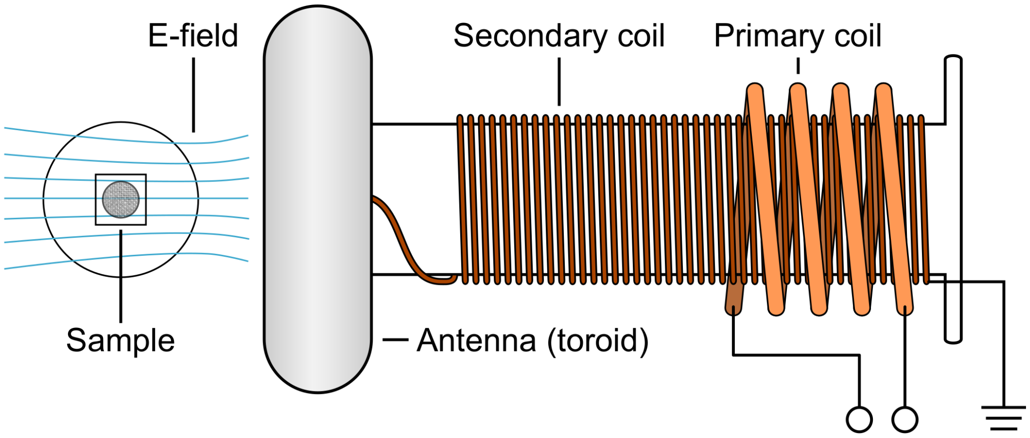

Figure 3.11: An overview of the parts of the teslaphoretic apparatus. The electric field lines are recreated from calculations of the Cherukuri group for a toroidal antenna.[6] The coil is aligned horizontally and the samples are placed before the antenna. The figure is a modified picture from the public domain.[102]

The spark gap Tesla coils explained above are popular among hobbyists. An alternative is the solid state Tesla coil[101], which was also used in the group of Cherukuri, where the first circuit does not include a spark gap and LC circuit, but instead consists of an inductor and a function generator, powering the system with a certain AC frequency to constructively induce the second coil. By Cherukuri and co-workers, for this purpose a plasma generator was used, which created a 2 MHz oscillation. The TC was put in a horizontal alignment and samples placed before the toroidal antenna, as seen in Figure 3.11.

The Cherukuri group undertook a variety of analyses, measurements and calculations concerning this technique. With the boundary element method, they calculated the electric field lines of the electric field E, as well as the gradient force field lines of the corresponding function E^2 mentioned earlier. As those lines are approximately parallel close to the TC's antenna, this is where their experiments took place. The aforementioned experiments concerning wire growth of CNTs in Pluronic water were "the longest directed self-assembled structures made to date"[6], as the authors claim, owing to the unconfined character of the Teslaphoretic field. Depending on the output power of the plasma generator supplying the TC, rapid assembly of nanowires was documented 30 cm away from the antenna and slower growth up to 50 cm away. If the nanotubes were suspended in one single spot, a thick wire formed; when they were dispersed throughout the container, many parallel thin wires formed. Those thin wires often snapped together with neighboring filaments when the oppositely charged heads and tails came close to each other, forming broader aggregates.

The authors hypothesize that the assembly of the CNTs takes place because of charge separation along the conducting paths, leading to induced dipole moments and thereby strongly interacting electric fields. It is mentioned in a footnote that materials other than

CNTs have been tried as well, namely glass beads, polystyrene, carbon black, gold, graphite, wax, and silica beads. It is said that those materials aligned as well, yet, no details are shown. Materials formed by the supramolecular stacking of small molecules have not been tried.

As a side note: While the authors of the paper call this process self-assembly, it can be argued whether or not that is the case. Self-assembly refers to the pathway down into thermodynamic minimum. The activation of the TC represents an energy influx, without which the CNTs would not assemble. Therefore, the process should rather be categorized as self-organization. If a suspension of CNTs is used, upon deactivation of the TC the suspended nanotubes slowly rearrange again due to convection of the water. Brownian motion might play a role in the re-equilibration as well[103], although it is unclear whether the mostly large separate aggregates are small enough to fall into its regime, as the nanotubes are not individually dissolved. The entropic rearrangement is a clear aspect of self-organization as opposed to self-assembly.[37]

Table 3.2: Exemplary polarizabilities of solvents used in this work.

Solvent	Polarizability[104] / $Å^3$
Water	1.50[105]
Methanol	3.21[106]
Acetonitrile	4.28[106]
Dichloromethane	6.66[106]
2-Propanol	6.67[106]
1,2-Dichloroethane	8.00[106]
Carbon disulfide	8.75[104]
n-Hexane	11.63[106]
Toluene	11.86[106]

Because of its similarity to dielectrophoresis, it is hypothesized that the requirements to solvents and compounds are similar. One main requirement might be that the polarizability of the compound has to be greater than that of the solvent[98], as described earlier in Figure 3.9. The solvents used in this work are shown together with their respective polarizabilities in Table 3.2. Determining the polarizability of the compounds that need to be aggregated is not trivial, as it depends on the exact aggregation, shape, internal defects and other properties.

3.6 Instruments

3.6.1 Optical Microscopy

Optical microscopy has become a standard technique for visual evaluation of surfaces. While classical microscopes are diascopal (meaning that the light source and objective are on opposite sides of the specimen), episcopal illumination is possible as well. This means that the light is emitted of the same side of the specimen, through the objective. This allows for evaluation of opaque or thick samples. As optical microscopy is ubiquitous, the basic schematics shall be omitted at this point.

One advanced contrasting method shall be addressed. The standard illumination method for episcopal optical microscopy is the brightfield illumination, where the light shines vertically upon the specimen, is reflected and the direct reflection is observed. This allows for observation as-is, and can be compared to observation with the naked eye. For enhanced contrast of borders and therefore structured surfaces, darkfield illumination was developed. Here, the incident light is shone in at an oblique angle, while the centrally arriving light is blocked. Only the light portion that is scattered on corners of the specimen and then enters the pathway is observed. This leads to different coloration than is observable to the naked eye. Background appears dark, while the specimen appears in brighter colors. In this work, mainly this contrasting method will be used as it is superior for imaging of phase boundaries and microscopic objects.[107]

3.6.2 Scanning Electron Microscopy

Scanning electron microscopy can be used as a method to obtain images of higher resolution and magnification than optical microscopy, while being flexible concerning the choice of substrate. Contrary to atomic force microscopy, which needs perfectly flat surfaces, and transmission electron microscopy, which can only be used with specimens embedded within a specialized grid, SEM has the advantage that it allows for measurement of coated substance on standard glass platelets. If non-conductive, the samples have to be covered in a thin overcoat of conductive material, for example a gold coating of approximately five nanometers in thickness. This on the one hand reduces charging phenomena, which present themselves as fluctuations of contrast and brightness. On the other hand, it enhances the yield of detected secondary and backscattered electrons.[108]

The basic schematics of a scanning electron microscope can be seen in Figure 3.12. From the electron gun containing a tungsten filament, the electrons emanate. They pass through an anode, are focused by magnetic lenses and reach the sample. On the sample, a number of scattering phenomena happen. In standard SEM, mainly the secondary electrons and the backscattered electrons are detected. Secondary electrons are the product of inelastic interaction, where electrons within the sample are excited, and those close to the surface of the specimen can escape the sample. Backscattered electrons on the other hand are the result of an elastic interaction, where the electrons retain their energy and scatter directly back from the sample. Another detection method modern SEMs can be equipped with, is

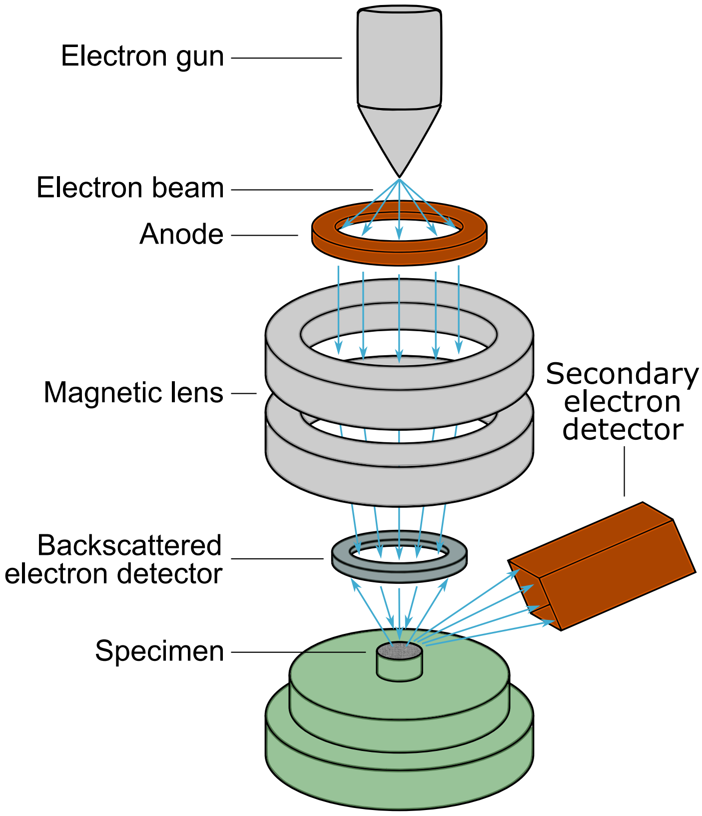

Figure 3.12: The schematics of a SEM.

the cathodoluminescence detector. Certain specimens can release excess energy as photons spanning from infrared to ultraviolet upon relaxation of excited electrons. With a specialized detector containing a photomultiplier, these signals can be used for additional morphology information.[108]

4 Methods of Computational Analysis

4.1 General Remarks

In this work, specific requirements made special computational analyses necessary. These were utilized to quantify phenomena observed by microscopy. To allow for reproducibility, the programs, procedures and parameters used are given.

4.2 Computational Analysis of Structure Orientation

For the analysis of the orientation of fibers and other structures, the OrientationJ plug-in (Version 2.0.4)[109,110] for ImageJ (Fiji distribution, Version 1.53c)[111,112] was used. The plug-in offers a variety of tools. Specifically "OrientationJ Analysis" and "OrientationJ Distribution"[113] were used. The former gives a visual representation by analyzing structures and coloring them depending on their global angle, generating a hue, saturation and brightness (HSB) picture. The hue is the color used for different alignments, the saturation depends on the coherency (a value gathered by the algorithm which quantifies the "obviousness" of the alignment) and the brightness stems from the source picture. Figure 4.1 shows an example of the colors used to highlight structure orientation. In the case of horizontal alignment, the angle is 0° and then increases in counterclockwise direction.

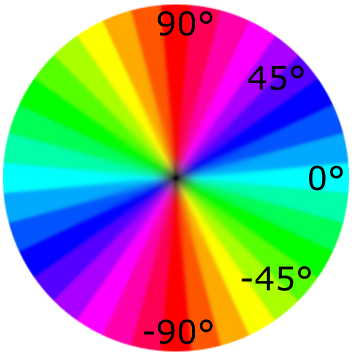

Figure 4.1: Example of the colors generated by the "Orientation Analysis" function of the plug-in OrientationJ for ImageJ.

"OrientationJ Distribution" creates a histogram of the data and plots the abundance against the angle. The abundance is measured in pixels (that "point" into a certain direction based on their environment) and is strongly dependent on the composition of the image file. For the generation of the histogram, a minimum coherency and a minimum energy can be set. The coherency is an indicator for the directionality: A value of 0 indicates that the feature is isotropic while a value of 1 indicates a strong anisotropy. In most sources, this minimum is set to 0.7 to exclude false positives,[114–117] and for this work, the same value was chosen. The minimum "energy" can be adjusted to neglect weak borders and thus avoid false values generated by noise in the picture. Here, aforementioned sources vary in values between 0.02 and 0.10. Testing showed that varying the minimum energy between those values did not cause a significant difference, so a value of 0.05 was chosen. In this work, the term "orientation analysis" refers to the process combining the orientation-dependently colored pictures and the histograms plotted from the acquired data.

The Gaussian window (σ) and the shape of the structure tensor can be adjusted as well.[118] The Gaussian window was varied depending on the structure size (of the aggregates formed on surfaces) and is mentioned in company of the evaluated images. For very narrow structures, a σ value of 1 px was set, while for broader structures and higher magnifications, this value was increased to a maximum value of 5. The optimal value was determined from the "OrientationJ Analysis", whether the structures were perceived as being colored correctly. The shape of the structure tensor was set to "cubic spline", as this offers a good compromise between speed and accuracy.[118]

Before the orientation could be analyzed, the image file was prepared. The contrast was set to a minimum value of 70 to minimize noise. The image file then had to be set to a 32 bit gray-scale format. Afterwards, a circular image window was generated with the plug-in *Windowing* (Version 3b0.x)[119], the options were set to "Percentage Flat = 80" and "Mean Value: Keep", with the remaining settings left at default. The circle was cropped from the center of the image with the circle diameter set to the height of the picture. The process was semi-automated with a macro, allowing for the execution of the single steps by keystrokes. The macro is given in the appendix of this work.

Orientation analysis for SEM images was done by slight modification of the macros. Because the output images of the SEM are more grainy, they were first smoothened, using the "Smooth" function of ImageJ three times. Otherwise, this led to false analysis of orientation. The remaining procedure was similar to the optical microscope images.

This method was used in connection with samples generated by teslaphoresis described in Chapter 5.2. In addition, it was used in Chapter 6.9 to demonstrate the orientation of the fibers, where surfaces were spin-coated with a hydrophobic gelator.

4.3 Morphology Evolution Analysis of Coated Surfaces

Determining the thicknesses of the surfaces created in Chapter 6 posed a problem. Because the coatings were uneven, measuring thickness by tilting the coated substrates vertically under a light microscope would not deliver reliable values. It was impossible to focus the edge of the coating and the glass substrate simultaneously. For more advanced thickness determination methods like ellipsometry, the coatings were too thick and irregular.

Thus, another method was devised. It was observed that thicker coatings of the used compounds were opaque, while thin coatings were nearly transparent. This allowed for the comparison of thicknesses by evaluating the “whiteness” of the surfaces. In a darkened container, a LED strip of constant brightness and a sample holder with a black surface as background were installed. A camera was attached to the box to take photographs of the sample on the inside from a top view, while being able to operate it from the outside. Shutter speed and aperture of the lens were set to constant values to make the captures comparable:

Shutter speed: $\frac{1}{100}$ s
Aperture: F/8.0
Film speed: ISO 1600/33°

With these photographs, an automated analysis was undertaken, which performed the following steps. The image was converted to 8 bit gray-scale, which gives each pixel a brightness value between 0 (black) and 255 (white). The picture was then masked, leaving only a square area with side lengths of 1305 px, which corresponds to the surface without background for the evaluation of the picture. In this area, a script written in Python counted the number of pixels for each brightness between 0 and 255. The script was written by Pin-Wei Lee and is documented in her master’s thesis.[120]

Considering the transparency of the thin layers and the black background of the sample holder, thin layers of coating are close to black and have low brightness values, while the densely coated, opaque surfaces have higher values. Pictures of clear glass were taken and evaluated for comparison and the results shown along with the coated surface. The intensity of the peaks translates to the amount of pixels of that brightness that were measured and is therefore called abundance. Because the control value of empty glass would clearly surpass the values of the coated surfaces, as all measured pixels fall within a narrow brightness range, the control peak was manually lowered in intensity. This was done by dividing its values by a number between two and six, depending on the distribution of the sample peaks.

The method was termed morphology evolution analysis (MEA). The values have to be interpreted cautiously, as the method is not very well calibrated due to the lack of comparable prior experiments. The material on the surface might cause neighboring areas to illuminate due to light scattering, returning higher minimum values than the glass reference peak. Starting at a certain coating thickness, the opacity might not be increased anymore and the brightness recorded at this maximum opacity does not correspond to a brightness value of 255. The purpose of the method is to give a rough estimation of the thicknesses of the different regions of the surface, and thus give some insight into the abrasion mechanisms during stability testing.

5 Teslaphoresis for Achieving Anisotropy in Supramolecular Materials

5.1 Design and Assembly of the Teslaphoretic Apparatus

5.1.1 First Tesla Coil Design

To attempt the anisotropic self-organization of materials, a first working model of a Tesla coil was build in resemblance to the model used in the group of P. Cherukuri. This was done in collaboration with Thien Ngo from the National Institute for Materials Science in Tsukuba, Japan. The details given in the original publication[6] are presented in Table 5.1. As a power source, a 2.5 kW plasma generator (MKS Nova-25A) had been used. The values mostly had to be converted from imperial to metric numbers, as most components were only available in metric scale. Several TC prototypes were built to determine and optimize parameters, partially not given in the original publication, and partially due to conversion changes from the imperial to the metric system. The determined detailed parameters can be seen in Table 5.2.

Table 5.1: Parameters and dimensions given in the original publication[6]:

Primary coil	Helical shape, hollow copper tubing, diameter 0.25 in	
	Diameter	5 in
	Height	5 in
	Pitch	0.25 in
Secondary coil	Helical shape, 18 AWG magnet wire around polycarbonate cylinder	
	Inner diameter	2 in
Top load	Aluminum toroid capped with an aluminum disk	
	Toroid diameter	8 in
	Disk diameter	7.5 in

A 2 MHz plasma generator from Noda RF Technologies was used to create the AC current needed to power the apparatus. With the values presented in Table 5.2, a working configuration was achieved. Pictures of the assembly process are given in the appendix of this work.

The output power was adjustable in the range of 0–500 W. Power in the range of 10–50 W was usually enough to see an effect on CNTs.

Table 5.2: Parameters and dimensions used in the construction of the first TC prototype:

Primary coil	Helical shape, hollow copper tubing with 6.35 mm outer diameter	
	Outer diameter	110.5 mm
	Inner diameter	97.1 mm
	Mean diameter	103.8 mm
	Coiling height	133.8 mm
	Number of windings	12
	Spacing	5 mm
Secondary coil	Helical shape, 18 AWG (1.024 mm) copper wire on PMMA cylinder	
	Outer diameter	52.2 mm
	Inner diameter	50.0 mm
	Mean diameter	51.1 mm
	Coiling height	259 mm
	Offset from ground	10 mm
	Distance to top load	40 mm
Top load	Aluminum toroid capped with an aluminum disk	
	Toroid height	50.4 mm
	Toroid outer diameter	200 mm
	Toroid inner diameter	98 mm
	Disk offset from toroid center	20 mm
	Disk diameter	120 mm
	Disk thickness	1.5 mm

Whether or not the electric field was of adequate strength was determined in two ways, shown in Figure 5.1. One method was holding a household neon tube in front of the TC antenna in a distance of about 0.5–0.8 m. The tube would then illuminate without contact, and the qualitative assessment of the brightness was used to estimate the relative field strength (and whether a modification afforded an improvement). The second method was a reproduction of the CNT-trials done in the Cherukuri group. CNTs immersed in 1 % Pluronic water were poured into a Petri dish, which was put in front of the antenna. When the TC was switched on, the aggregation speed was judged qualitatively. With this TC model, aggregation of the nanotubes was obvious within 1 min. Efforts to measure the electric field with a hand-held device for quantitative evaluation were unsuccessful, as the field strength extended the possible range of the devices that were tried.

The details and parameters of this TC configuration are shown in Table 5.2. It will be referred to as the first model of the TC and was used in the trials presented in Chapters 5.2.3.1–5.2.3.3.

Figure 5.1: The strength of the electric field was qualitatively estimated by two methods: (left) by household neon tube illumination and (right) by the aggregation speed of CNTs suspended in Pluronic water.

5.1.2 Second Tesla Coil Design

Trials were undertaken by Thien H. Ngo, whether TCs of broader commercial availability would yield the same results. Several models were tested. Specifically, the TC model “PLLSSTC TSL002” by Sunnytech[121,122] proved to be effective, if the pointed antenna (originally used for the production of streamers/“lightning”) was exchanged for one of plate-capped toroidal shape. In this work, first prototype antennae were made out of conductive adhesive tape around a wire template. After successful trials with this prototype, a solid antenna was turned from aluminum alloy (EN AW-2007, technical drawing in the appendix of this work). A wooden scaffolding was built to suspend the apparatus in a horizontal position for it to be applicable to drop-casting procedures. It had to be ascertained that no electrically conductive parts were incorporated, therefore the scaffolding consisted of particle board and wooden dowels and was fixed with adhesive. Figure 5.2 shows the final setup.

After adjustment of the spark gap, strong fields could be generated, as determined from trials with CNTs. The nanotubes oriented in the field more quickly than in the work done in the group of P. Cherukuri, as estimated by comparison with the videos provided with their publication[6]. One advantage of this modified setup is its much lower cost. No plasma generator is needed to power the apparatus, which lowers the price from over ten thousand to hundreds of euros/dollars. It is also more facile to set up, as only a wooden scaffolding for horizontal positioning and a custom antenna had to be fabricated. A disadvantage is that this model is prone to burning out; the cable between the secondary coil and the antenna had to be repaired several times. Additionally, the input power can not be adjusted and is fixed. This model of TC is used in most trials described in this work, unless otherwise noted.

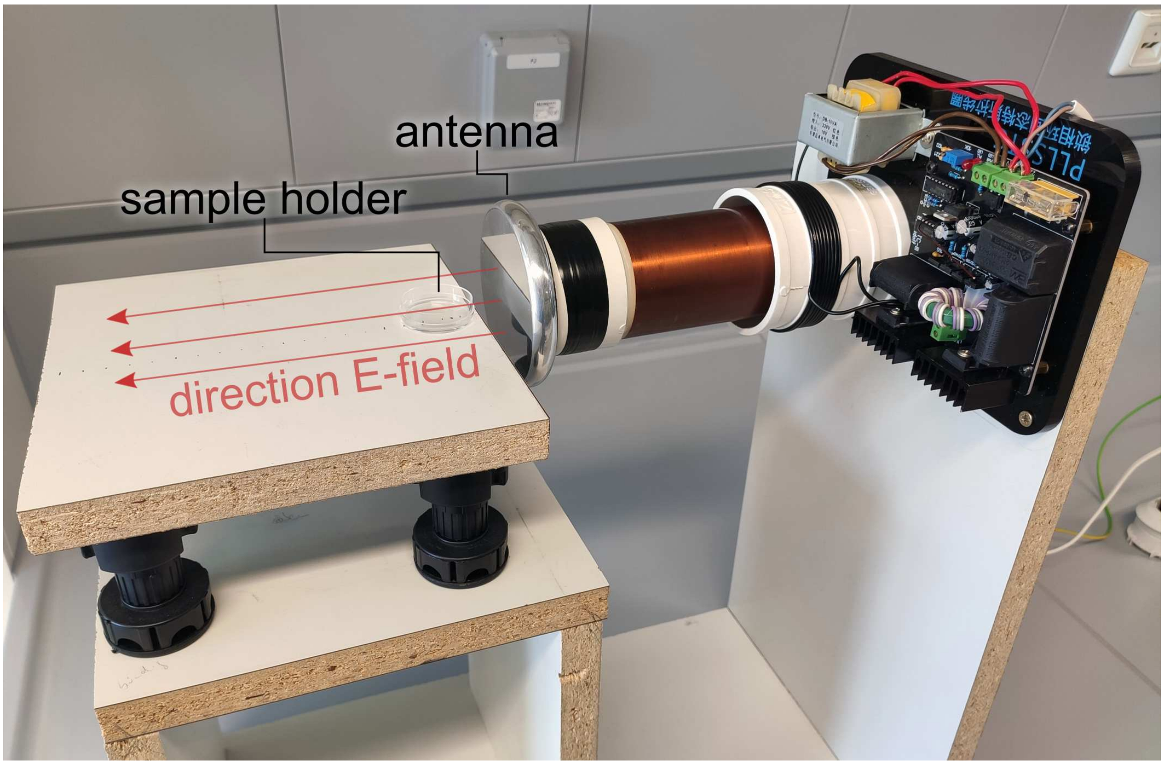

Figure 5.2: The horizontally aligned TC.

5.1.3 Safety Measures

The antenna of the TC possesses a very high potential V in the order of magnitude of 10^5 to 10^6 V. The current I is low, reducing the risk of adverse health effects, but nonetheless safety precautions were taken:

- Whenever not in operation, the TC was disconnected from the power.
- The TC was only operated under close supervision, and temperature checked with a laser thermometer.
- While in operation, swift access to the power main was secured to be able to disable the coil if need be.
- If streamers were observed, the spark gap was varied to reduce the field strength. Initial, short-lived streamers upon activation of the coil were accepted.
- A second person was in close proximity for supervision, but it was made sure that no other person approached the area of the TC while in operation.
- The TC was set up in careful distance to electrical appliances and ferromagnetic materials. The scaffolding was fabricated without metal screws or other ferromagnetic materials to avoid grounding and thus redirection of the electric field or the closing of spark gaps. No metal accessories were worn on parts of the body in direct vicinity of the antenna.

- The area in front of the coil was not accessed and no metal tools were used while the TC was active. Drop-casting was done prior to activation of the coil and sample retrieval after disconnecting the power.
- Solvent amounts while drop-casting were small (10–100 µL) to reduce the risk from accidental ignition of organic solvents. Although ignition was never observed personally.
- Nitrile gloves were worn to reduce the conductive exposure of the body.

5.2 The Influence of the Teslaphoretic Field on Different Materials

5.2.1 Overview of the Used Compounds

In the following section, teslaphoretic studies with a variety of different compounds will be shown. The compounds were chosen on one hand for reasons of availability. On the other hand, different representative motifs were selected to investigate the effect of the electric field of the TC on different classes of supramolecular compounds.

Carbon nanotubes are a first stepping stone, as the foundation of teslaphoresis had been laid in the group of P. Cherukuri with work on these compounds. Based on this, CNTs with perfluorinated side chains were envisioned to create the possibility of anisotropic wettability, as the high fluorine content enhances the water-repellent properties. These will be discussed in Chapter 5.2.2.

CF7 (Figure 5.3) was chosen as a low molecular weight gelator without aromatic moieties or a large permanent dipole and will be discussed in Chapter 5.2.3.1.

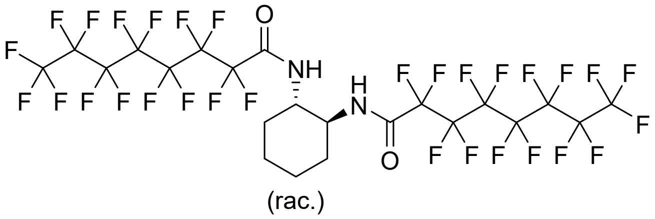

Figure 5.3: Low molecular weight gelator **CF7**.

Compound **1** aggregates supramolecularly and forms π-donor-π-acceptor aggregates in the form of filaments. Alternating intermolecular stacking of the aromatic moieties might allow for charge transport along the supramolecular stacks. Also, the internal permanent dipole

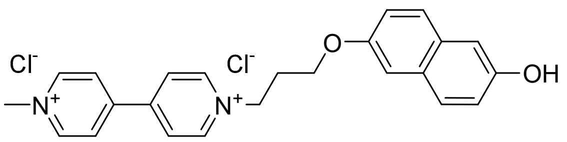

Figure 5.4: π-Donor-π-acceptor compound **1**.

might enable a susceptibility to the electric field of the TC. This compound is covered in Chapter 5.2.3.2.

The pyrene containing compounds **2**, **3** and **4** were chosen because the non-polar aromatic group might offer enough polarizability for the electric field of the TC to have an effect. Compound **2** is a known gelator, forming fibrous aggregates[123], which were envisioned to align in the field. Compounds **3** and **4** are fluorinated derivatives, again with the aim to create anisotropic hydrophobicity. This class of compounds is discussed in Chapter 5.2.3.3.

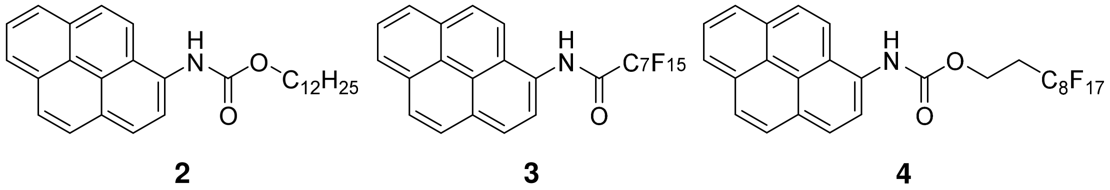

Figure 5.5: Pyrene-based gelator **2** and fluorinated derivatives **3** and **4**.

4TG and **5TG** are literature-known oligothiophene compounds, which gelate and form fibrous aggregates. While **4TG** creates coatings that are non-conductive, coatings form **5TG** were reported to show semiconductivity.[124] Therefore they will be used to investigate organic π stacks and the role of conductivity when using the electric field of the TC. This is covered in Chapter 5.2.3.4.

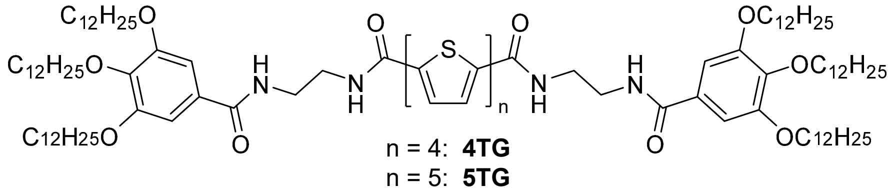

Figure 5.6: Oligothiophene gelators: non-conductive **4TG** and conductive **5TG**.

Certain NDI compounds are known to create semiconductive aggregates as well.[125] **NDI-C8**[126] was chosen because of the observed ability to form needles upon evaporation of the solvent. These high-aspect-ratio aggregates in combination with a certain electron mobility might exhibit ordering in the teslaphoretic field. This compound is covered in Chapter 5.2.4.

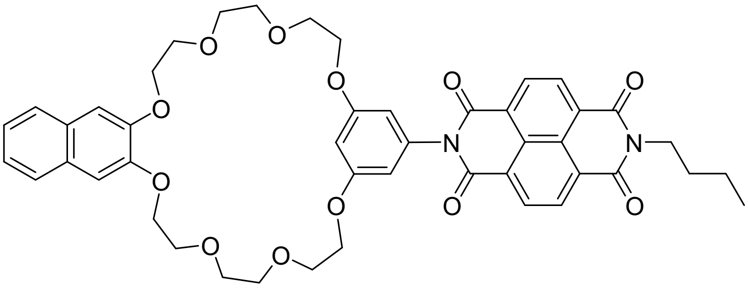

Figure 5.7: Naphthalene diimide compound **NDI-C8**.

5.2.2 Teslaphoresis on CNT Derivatives

The foundation of teslaphoresis had been laid in the group of P. Cherukuri with work on CNTs. Alignment experiments with nanotubes have been recreated in this work, with two intentions. It provides an immediate qualitative estimation about the effectiveness of the TC whilst also indicating the direction of the electric field lines, and proves that they are close to parallel in the area that is used for drop-casting. A solution of water with 1 wt% Pluronic® P-123 was prepared. An arbitrary amount of CNTs was added. The mixture was dispensed into a large glass Petri dish. This was placed in front of the TC, which was then switched on. Within approximately three seconds, the nanotubes aligned into parallel shapes, as depicted in Figure 5.8 (left).

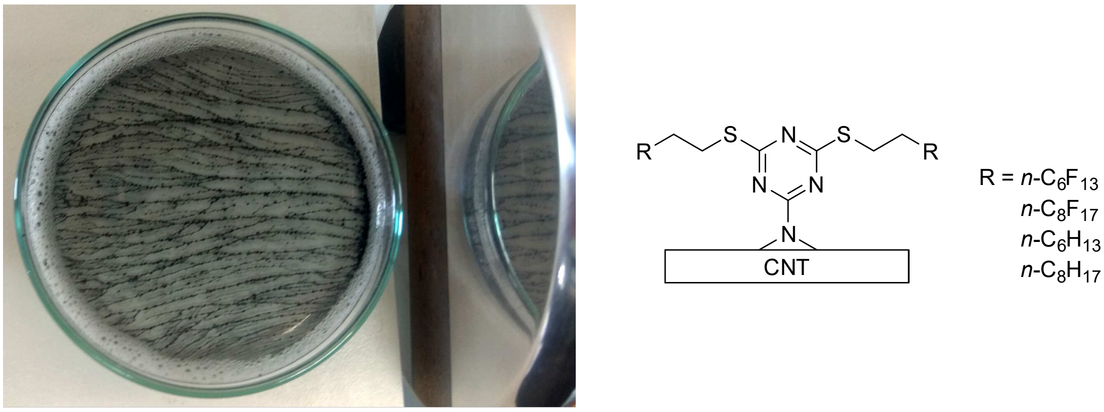

Figure 5.8: Left: Unsubstituted, pristine CNTs in 1 % Pluronic water, aligned in the electric field of the TC. Right: Structures of the fluorinated and non-fluorinated CNT derivatives synthesized under supervision of I. Donskyi for teslaphoretic trials.

Based on these initial results, carbon nanotube derivatives provide an obvious stepping stone on the path towards anisotropic functional materials by utilization of a TC. CNTs substituted with perfluorinated chains and their non-fluorinated analogues were synthesized by R. Schusterbauer and I. Donskyi for investigation in the electric field of the TC. The structures are shown in Figure 5.8 (right). Due to their expertise in graphene and CNT functionalization with triazine spacers, these spacers were used for tethering the fluorinated or non-fluorinated side chain to the CNTs.[127]. The side chains were connected by using thiols, so they contain a sulfur atom attached to the triazine, then two non-fluorinated methylene groups attached to either C_6F_{13}, C_6H_{13}, C_8F_{17} or C_8H_{17} chains.

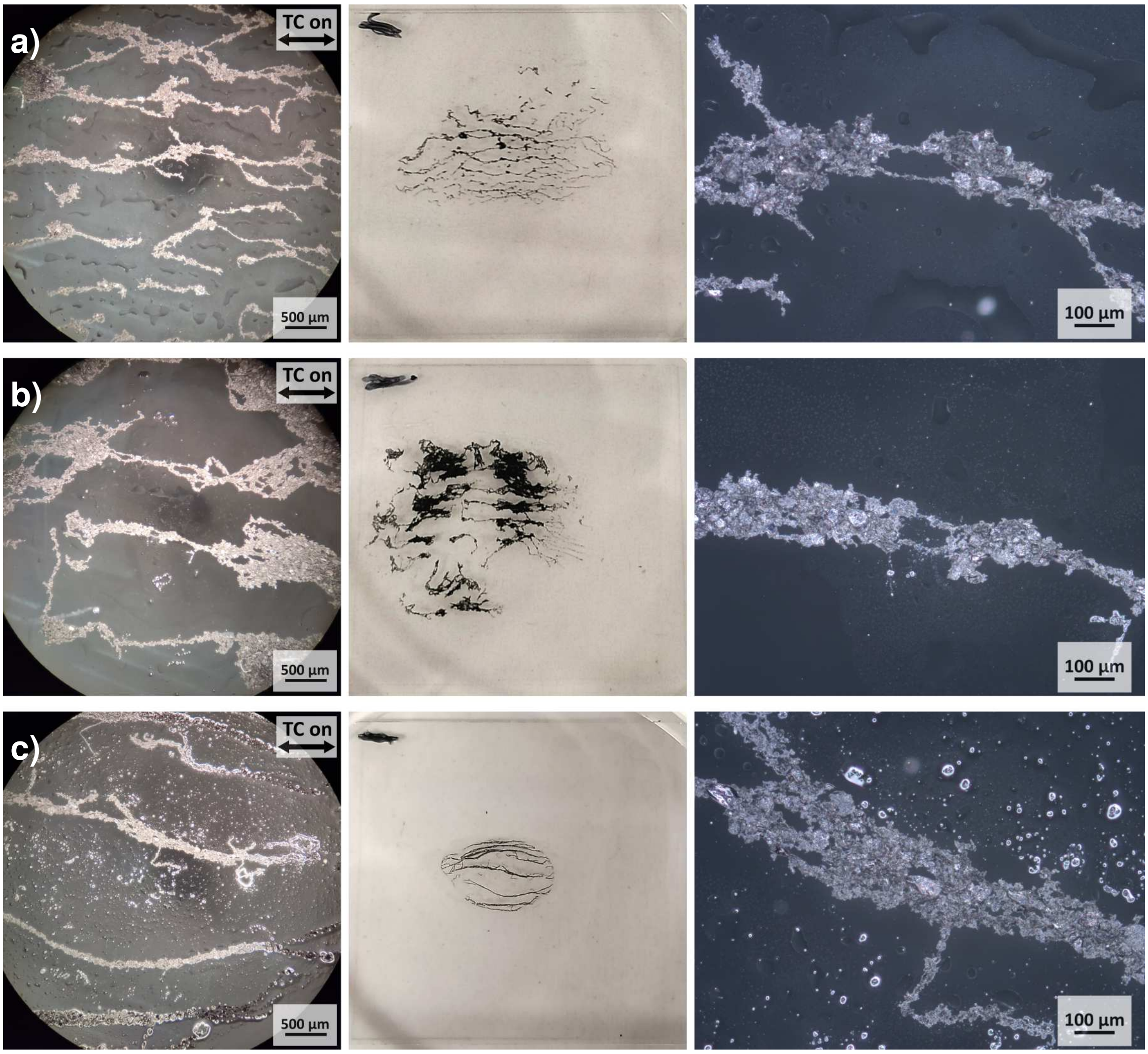

Figure 5.9: C_8F_{17}-CNTs drop-cast in the electric field of the TC. Shown are a picture through the ocular, a macroscopic picture of the coated glass surface and an optical microscope image (10x magnification), respectively; (a) cast from 1 % Pluronic acetonitrile (MeCN), TC on for 2 s, (b) for 5 s and (c) drop-cast from 1 % Pluronic water, TC on for 20 s. The scale bars on the ocular pictures are recreated from the optical microscope images. The glass cover slips are 22 mm × 22 mm in size.

Acetonitrile (MeCN) was deemed the most suitable choice for teslaphoresis experiments. It evaporates quickly enough to allow drop-casting in a short time frame to reduce the risk of TC overheating. In addition, it is only little polarizable (Table 3.2) to enable the movement of the drop-cast compound itself. It the case of (fluorinated) CNTs, MeCN proved to be a poor solvent; aggregates of nanotubes would not suspend, even through sonication. Therefore, Pluronic was added to enhance the solubility in MeCN, with positive results. Suspensions similar to the ones in Pluronic water were created.

Images of drop-casting experiments are shown in Figure 5.9. To get a better overview, photographs taken with a camera through an ocular of the optical microscope are displayed as well. These offer a larger field of vision compared to the standard camera mount, but suffer from diminished focus/resolution, improper lighting and a scale bar which has to be determined manually by comparison with images taken in the conventional way. An amount of 1 mg mL^{-1} of C_8F_{17}-CNTs was suspended in either 1 % Pluronic MeCN or 1 % Pluronic Milli-Q water, and then drop-cast in the electric field of the TC. Upon switching on of the TC, the structures is the suspension quickly aggregated, in MeCN quicker than in water. The TC was thus switched off before the complete droplet evaporation. In water, the TC was left running for 20 s, while with MeCN it was only activated for either 2 s or 5 s. The longer exhibition time already led to a visible broadening of the formed strands of CNTs and they were pulled either towards or pushed away from the antenna of the TC. The most regular strands were formed in Pluronic water, where the nanotubes aggregated more slowly but more orderly.

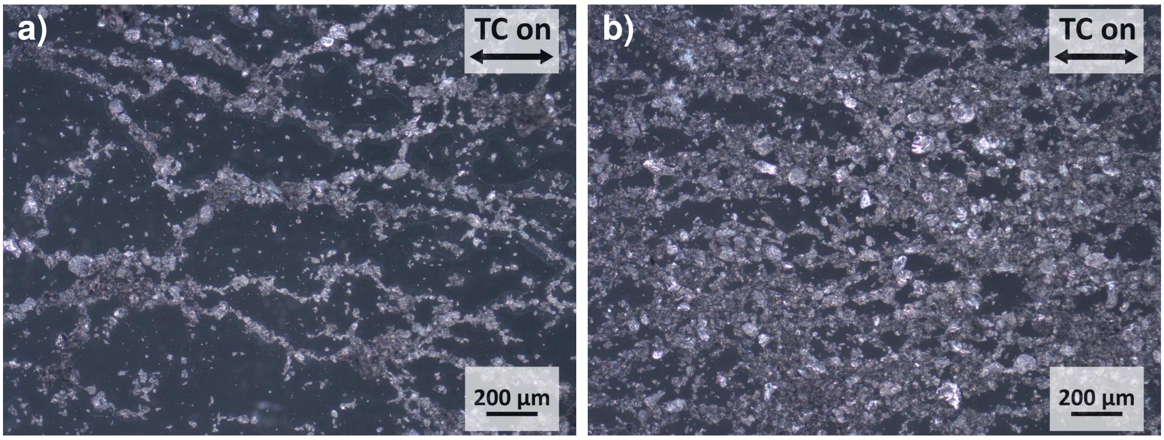

Figure 5.10: CNT derivatives drop-cast in the electric field of the TC, from a 1 mg mL^{-1} suspension of carbon disulfide; (a) C_6H_{13}-CNTs, (b) C_6F_{13}-CNTs.

The polarizability of carbon disulfide appears to be a cut-off point, starting from which teslaphoresis works poorly, even with as strongly polarizable substances such as carbon nanotubes. Suspensions of C_6H_{13}- and C_6F_{13}-substituted CNTs were prepared in carbon disulfide in concentrations of 1 mg mL^{-1} and drop-cast in the field of the TC. Compared to the nanotubes in Pluronic water and acetonitrile, case the TC had to run much longer, and was left on until complete droplet evaporation (45 s). Figure 5.10 shows order in the C_6H_{13}-substituted nanotubes, but not in the C_6F_{13}-substituted ones. This might result from a decreased polarizability of the fluorinated alkyl chains, lowering the overall polarizability of the molecule.

5.2.3 Materials Without a Reaction to the Teslaphoretic Field

5.2.3.1 Amide Gelator Without an Aromatic System

In the beginning of the teslaphoretic trials, after assembly of the first TC, the limitations of the technique were unclear. Therefore an explorative study was conducted, which materials are receptive to the electric field of the TC. The compounds in this and the following two sections were used in connection with the first TC design described in Chapter 5.1.1.

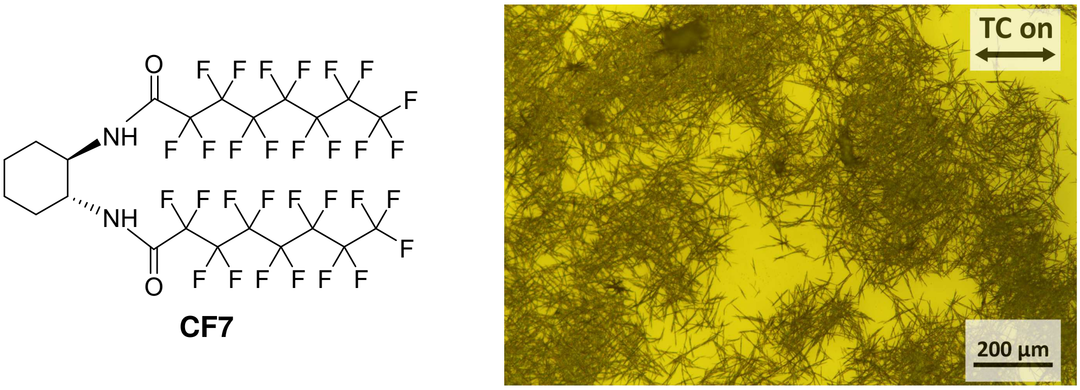
CF7

Figure 5.11: Left: The structure of **CF7**, a perfluorinated LMWG; right: surface created by drop-casting the substance from Et_2O in the field of the TC. No influence of the electric field is visible.

CF7 is a known gelator which can form superhydrophobic xerogels and is discussed thoroughly in Chapter 6 of this work. It was chosen for its ability to form fibers, but possesses no π cloud or (semi-)conductive properties. The polarizability is estimated to be low, because of the high fluorine content. It was drop-cast in the field of the TC from diethyl ether (Et_2O) in concentrations of 0.5 wt% and 0.2 wt%. Figure 5.11 shows the surface resulting from a concentration of 0.2 wt%. It can be seen from the micrograph that there was no obvious effect of the TC. Suspecting the structures hinder each other in their mobility, the 0.2 wt% solution was diluted to one tenth of the concentration. Although in that case, no fibers or sticks formed when drop-casting and no effect of the TC was visible.

5.2.3.2 Polar Molecule Forming π-Donor-π-Acceptor Aggregates

Compound **1** forms π-donor-π-acceptor aggregates in the form of fibers when exceeding a certain concentration or when exposed to a sodium chloride crystal, as shown by L. Cera *et al.*[128] It is soluble in water and other polar solvents. It was chosen for two reasons: For one, the π-systems stack alternatingly and might allow for charge transport along the π-stacks and therefore efficient charge separation along the supramolecular aggregates. On the other hand, it possesses an intramolecular permanent dipole created by the electron-poor methyl viologen group and the electron-rich naphthol moiety. It was unclear whether this dipole

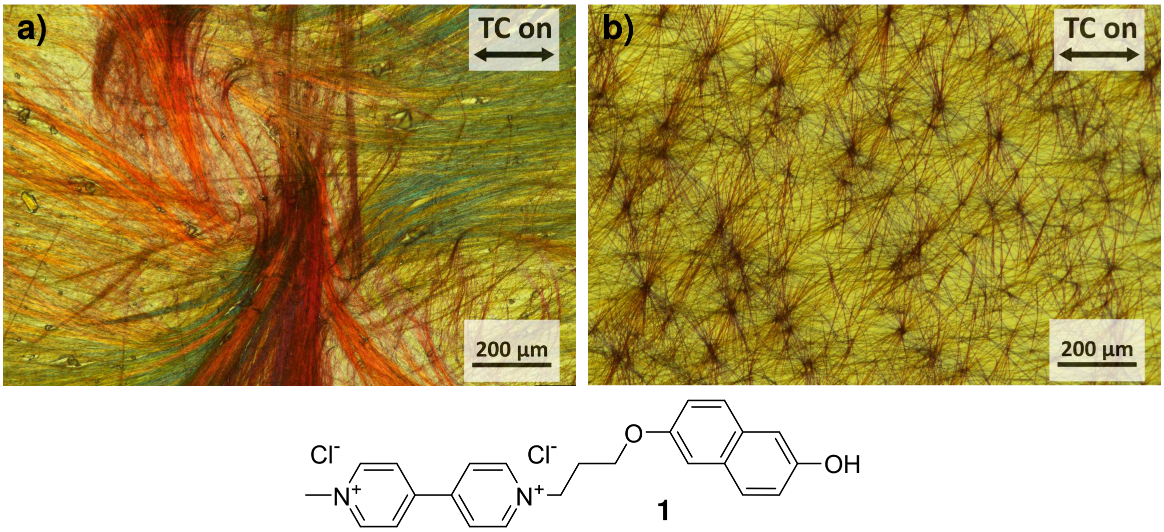

1

Figure 5.12: Structures formed by drop-casting **1** in the electric field of the TC, no influence of the electric field is visible; (a) 1 wt% in water, (b) 0.5 wt% in MeOH.

would be influenced by the electric field of the TC. The synthesis of the compound is reported elsewhere.[128]

The compound was used in connection with the first TC design described in Chapter 5.1.1; the molecular structure and microscope images are shown in Figure 5.12. When drop-cast from water in 1 wt% concentration, fibers grow from the edge of the droplet to the inside, and are apparently not influenced by the external electric field. When drop-cast from methanol in 0.5 wt%, rigid sticks of about 200 µm length were formed, growing outside in random directions from many nuclei. The difference in color depending on the orientation is explained by the polarized light contrasting method used in this particular case.

Drop-casting from water proved to be inconvenient when using teslaphoresis, as the evaporation time for a single droplet was between 20 and 30 min, making either low input power (first TC model) or intermittent cooling periods (second TC model) necessary. In methanol, the structures were not of satisfying length and did not seem receptive to the electric field. Therefore, work with this compound was discontinued in favor of other compounds which are better soluble in organic solvents.

5.2.3.3 Non-polar and Polarizable Aromatic Systems: Pyrene Derivatives

Because of the hypothesis that an extended π system could be susceptible to the electric field of the TC, a literature-known pyrene-based gelator[123] was synthesized. For increased hydrophobicity, fluorinated derivatives were synthesized as well, with the goal to achieve anisotropic hydrophobicity. The structures are shown in Figure 5.13. Compound **2** is the known gelator, compound **3** is a fluorinated analogue developed as part of this project.

Because of the rigidity of the fluorinated *n*-perfluoroheptyl chain directly attached to the gelator, a more flexible analogue **4** was devised.

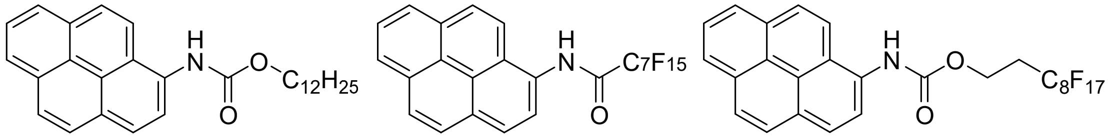

2 **3** **4**

Figure 5.13: Pyrene derivative envisaged for application in the electric field of the TC. Compound **2** is a literature known gelator, **3** and **4** are fluorinated analogues.

The strategies for the syntheses of the different compounds are shown in Scheme 5.1. The synthesis of **2** was carried out according to a modified procedure by D. AWASTHI and co-workers.[129] As carbonyl source and coupling reagent, 1,1′-carbonyldiimidazole (CDI) was added to 1-aminopyrene in dichloromethane. After heating for 4 h, 1-dodecanol was added and the mixture stirred for 16 h. After workup, 26 % of pyrene derivative **2** were isolated.

The synthesis of **3** was done via a modified method by L. XU and co-workers.[130] To a solution of 1-aminopyrene and triethylamine in tetrahydrofurane, perfluorooctanoyl chloride was added at 0 °C. After 2 h at room temperature and workup, compound **3** was received in 97 % yield.

Synthesis of **4** was done following a modified procedure by P. BABU[123]. Triphosgene was added slowly to the fluorinated side chain in chloroform at 0 °C, and under the presence of pyridine, 1-aminopyrene was added. After workup, pyrene derivative **4** was received in 70 % yield.

Gelation studies were undertaken to find a suitable solvent in which fibrous aggregates form. Solutions with 2 wt% of the substances were prepared by heating, and then cooled either at room temperature or in an ice bath. The cooling rate only made a difference for compound **2** in *n*-butanol, where solely with rapid cooling a very weak gel with leaking solvent formed. Cooling slowly in that case did not afford any gel. Cooling with ice was not practically possible in the case of *tert*-butanol, because the solvent freezes below 26 °C. The results are presented in Table 5.3 and surprisingly, the results vary from the literature. P. BABU *et al.* reported gelation for compound **2** in *tert*-butanol, *n*-butanol and *n*-hexane; this could only be reproduced without doubt for *n*-hexane. As stated before, the gel formed in *n*-butanol was very weak and the substance forming in *tert*-butanol could only be called a gel by stretching the definition, as only small gel-like flakes of around 1 mm in diameter formed. All of the gels formed were turbid.

Coating experiments were carried out with the first model of the TC. The goal was to achieve structures with high aspect ratios like fibers or needles, to investigate the influence of the

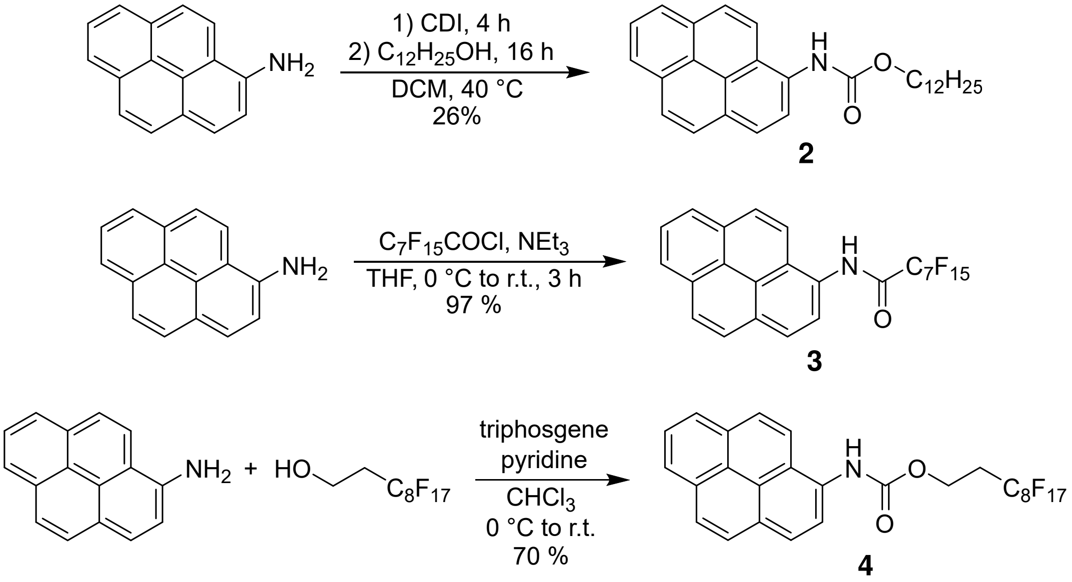

Scheme 5.1: The syntheses of the different pyrene derivatives **2**–**4**. Compound **2** was synthesized via a less toxic method[129] with CDI instead of triphosgene, albeit with lower yield. Therefore, different strategies were implemented for the syntheses of compounds **3** (via the acid chloride)[130] and **4** (carbamate synthesis with triphosgene)[123].

Table 5.3: Gelation studies of the pyrene derivatives. All compounds were prepared with 2 wt% of compound. All gels formed were turbid. G: gelates, S: stays in solution, I: insoluble, P: precipitates as solid.

Compound	*tert*-Butanol	*n*-Butanol	Butanone	2-Propanol	*n*-Hexane	Diethyl ether
2	G[a]	S / G[b]	S	G	G	G[c]
3	I	I	S	I	I	I
4	P	P	S	P	I	P

[a] Only forms small local flakes of gel-like substance. [b] When an ice bath is used for cooling, forms a weak gel with leaking solvent. [c] Gelates only upon sonication.

electric field. Because of the very poor solubility of compound **3** in most solvents, trials were only done with compounds **2** and **4**. Solvent choices were made depending on solubility, availability and evaporation speed. Concentrations were chosen lower than in the gelation trials, to dissolve the compound also at room temperature. Higher concentrations would necessitate a controlled regulation of the temperature, which is instrumentally impossible within the electric field.

The electric field of the TC did not have an effect on either of these substances when drop-cast. Figure 5.14 (a) shows a coating done from 0.25 wt% compound **2** in *n*-hexane, resulting in thin needles roughly 60 µm in length. These were ordered in random directions. Figure 5.14 (b) shows the same compound in the same concentration in 2-propanol (IPA). The peculiar surface generated resembles slightly thicker needles of again approximately 40 µm

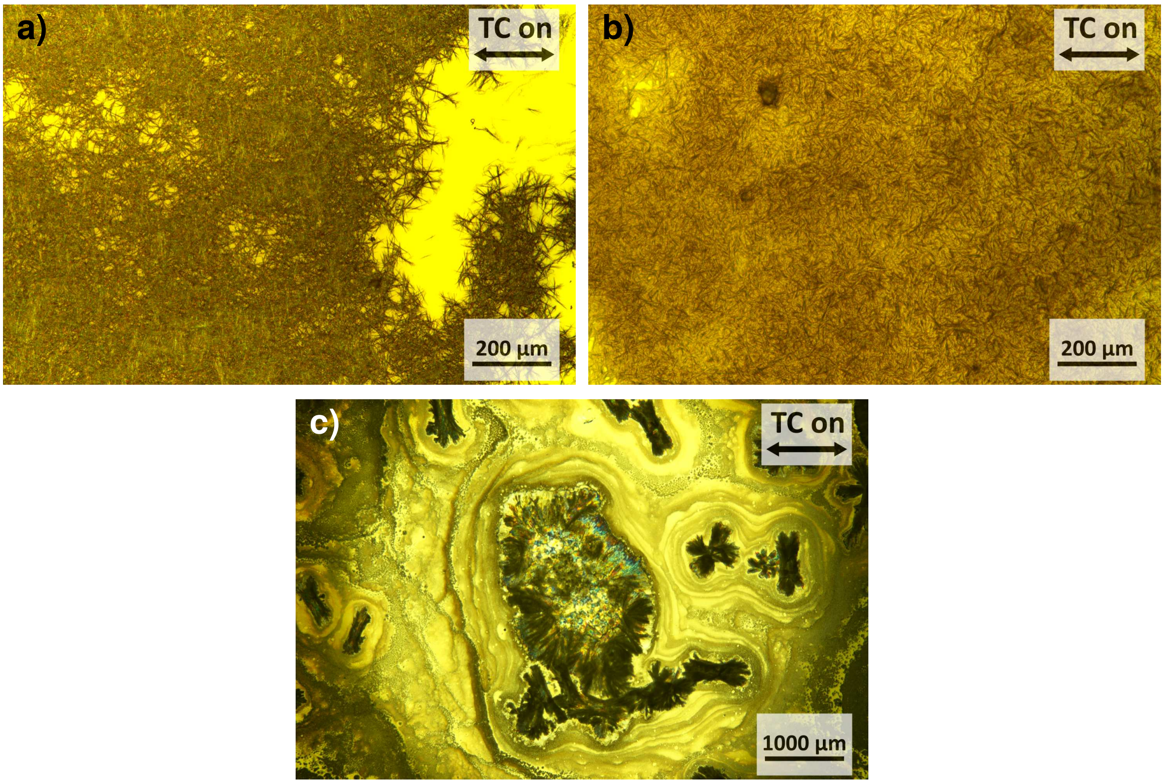

Figure 5.14: Surfaces drop-cast within the electric field of the TC; (a) 0.25 wt% compound **2** in *n*-hexane, (b) 0.25 wt% compound **2** in 2-propanol (IPA), (c) 1 wt% compound **4** in Et_2O.

in length, that seem to be enclosed in glassy/amorphous residue. The needles are oriented at random angles. Figure 5.14 (c) shows a microscopic image obtained from a 1 wt% solution of fluorinated compound **4** in Et_2O after drop-casting in the field. This experiment resulted in a crystalline residue on the surface without any influence of the electric field visible. Other concentrations and combinations of *n*-hexane, Et_2O and IPA led to structures without any aspect ratio, where an effect of the field was not visible.

This project helped interpret the requirements for drop-casting in the field of the TC. A relatively small (compared to carbon nanotubes) π system alone was not sufficient for being influencable by the electric field. It was hypothesized that the aggregates which are formed require suitable intermolecular stacking to emulate the behavior of CNTs, not along the axis of the molecule, but along the stacking axis.

5.2.3.4 The Role of Conductivity: Oligothiophene Gelators

A systematic comparison between conductive and non-conductive substances was envisaged for the following project. Oligothiophenes **4TG** and **5TG**, depicted in Figure 5.15 were to be synthesized and tested for their susceptibility to the electric field of the TC. Oligo- and polythiophenes are known for their conductivity under certain circumstances, for examples depending on the number of repeating thiophene groups and the overlap when stacking.[131] According to work done in the group of S. Stupp, **4TG** and **5TG** create organogels in a variety of solvents.[124] When evaporated, a fibrous coating remains. This coating exhibits conductivity in its dry state for the molecule with five repeating thiophene groups (**5TG**). However, the compound with four thiophene repeating groups (**4TG**) does not exhibit any conductivity under the same circumstances. It was envisaged that **5TG** might be receptive for the electric field of the TC, while **4TG** would not be influenced. This would shed light onto the properties needed of molecules and their aggregates to be able to form anisotropic coatings in the field of the TC.

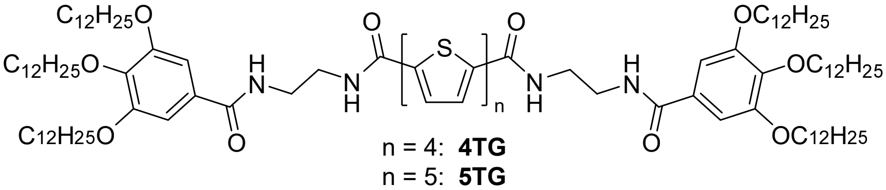

Figure 5.15: Structure of oligothiophene derivatives **4TG** and **5TG**.

The synthetic pathway is shown in Scheme 5.2. The first step was a threefold nucleophilic substitution to exchange the phenolic hydroxy groups of methyl gallate with long alkyl chains. Potassium carbonate and 18-crown-6 as a phase transfer reagent for higher basicity in acetone were used together with 1-bromododecane to afford methyl 3,4,5-tris(dodecyloxy)benzoate (**5**) in 94 % yield. The long alkyl chains serve to increase the solubility of the final compound, as oligo- and polythiophenes are known for their poor solubility.[132] In the next reaction, a saponification was carried out with sodium hydroxide in the first step and hydrochloric acid for reprotonation. A mixture of THF and water in 1:1 volume ratio was used as solvent. 3,4,5-Tris(dodecyloxy)benzoic acid (**6**) was received in 98 % yield. This compound was activated with *N*-ethyl-*N′*-(3-dimethylaminopropyl)carbodiimide hydrochloride (EDCl) and reacted with *tert*-butyloxycarbonyl (BOC)-protected ethane-1,2-diamine. 4-(*N*,*N′*-Dimethylamino)-pyridinium-4-toluenesulfonate (DPTS) was used as a weak proton donor. *tert*-Butyl(2--(3,4,5-tris(dodecyloxy)benzamido)-ethyl)-carbamate (**7**) was received in 90 % yield. In the next step, the protecting BOC group was removed by addition of trifluoroacetic acid (TFA) in chloroform and yielded the unprotected amine *N*-(2-aminoethyl)-3,4,5-tris(dodecyloxy)-benzamide (**8**) in 86 % conversion. For synthesis of the final building block for addition to the thiophene, again an EDCl-mediated peptide coupling was undergone, this time with 5-bromothiophene-2-carboxylic acid in dichloromethane. 5-Bromo-*N*-(2-(3,4,5-tris(dodecyl-oxy)benzamido)ethyl)-thiophene-2-carboxamide (**9**) was obtained in 88 % yield.

To undergo Stille coupling, a $SnBu_3$-substituted core part was required.[133] The thiophene derivative was commercially available in the case of two thiophene groups, but with three thiophene groups, it had to be synthesized (Scheme 5.3). This was done according to a

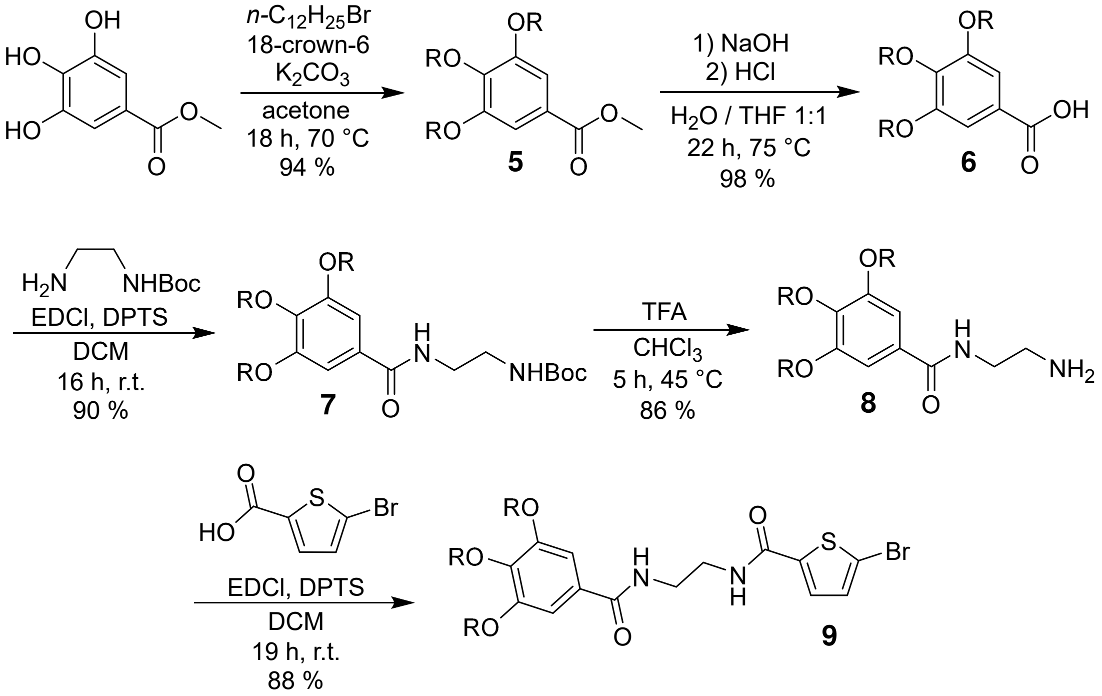

Scheme 5.2: Reaction scheme from the commercially available methyl gallate to the shell precursor **9** of compound **5TG**.

modified procedure by G. Brotas *et al.*[134] Under dry conditions, 5,5″-dibromo-2,2′:5′,2″-terthiophene was treated with *tert*-butyllithium in tetrahydrofurane at −78 °C and tributyltin chloride was added in excess. Although the crude product was purified, a mixture of approximately two parts 5,5″-bis(tributylstannyl)-2,2′:5′,2″-terthiophene (**10**) and one part tributyltin chloride was received. The product fraction corresponds to a yield of 63 %. Because the impurity should not hamper the following reaction, the compound mixture was used as is.

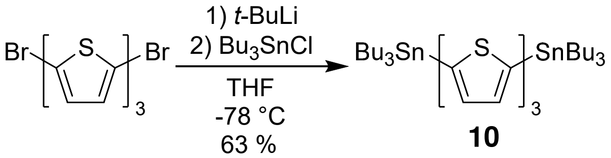

Scheme 5.3: Synthesis of core precursor **10** for the synthesis of **5TG**.

In the following step, the core precursor **10** was connected to shell compound **9** (Scheme 5.4). Under dry and degassed conditions the Stille coupling was carried out with tetrakis(triphenylphosphine)palladium^0 as the catalyst. Recrystallization afforded 59 % of the final product **5TG**. Because of its high affinity for aggregation, analytics and especially purity determination were impeded, as NMR afforded only broadened peaks. Because ESI-MS supported the existence of the product and the aggregation (and later fiber formation) was similar to the literature[124], a sufficient purity for further experiments was assumed. Synthesis of **4TG** as control compound was deferred due to its reliance on successful alignment of **5TG**.

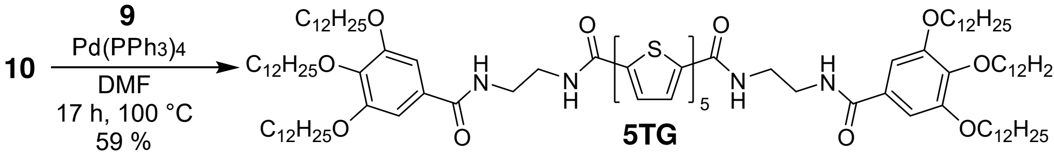

Scheme 5.4: The final step in the synthesis of **5TG** by Pd^0 catalyzed Stille coupling of compounds **9** and **10**.

As reported in the Stupp group, the compound gelated in a variety of solvents. Namely, the list comprises chlorobenzene, chlorocyclohexane, 1,2-dichloroethane, styrene, tetrahydrofurane (only **5TG**), thiophene (only **4TG**) and toluene as possible gelating solvents. Out of these, DCE and toluene were chosen because of their availability and because the time until droplet evaporation is short enough to not cause overheating in the TC.

Solutions of 5 mg mL^{-1} were prepared in each solvent. In the case of DCE, the 5 mg mL^{-1} solution created a strong gel unsuited for drop-casting, so it was diluted by one fifth, resulting in a concentration of 1 mg mL^{-1}. Upon drop-casting in the electric field of the TC, the toluene solution produced an amorphous precipitate on which the electric field seemingly had no influence, as seen in Figure 5.16. No distinguishing features were visible. Attempts to produce SEM images were not fruitful, as the coating appears to be too thin and devoid of distinct structures that could be focused on.

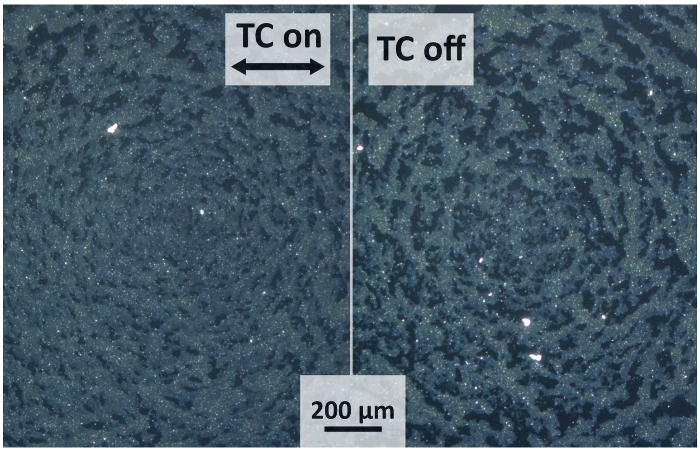

Figure 5.16: Coatings done with 5 mg mL^{-1} **5TG** in toluene (left) with and (right) without the electric field of the TC.

The castings done from the 1 mg mL^{-1} **5TG** solution in DCE initially seemed unpromising: On first glance, the microscope images taken of the surface cast in the electric field of the TC did not give the impression that the fibers were influenced by the electric field. Figure 5.17

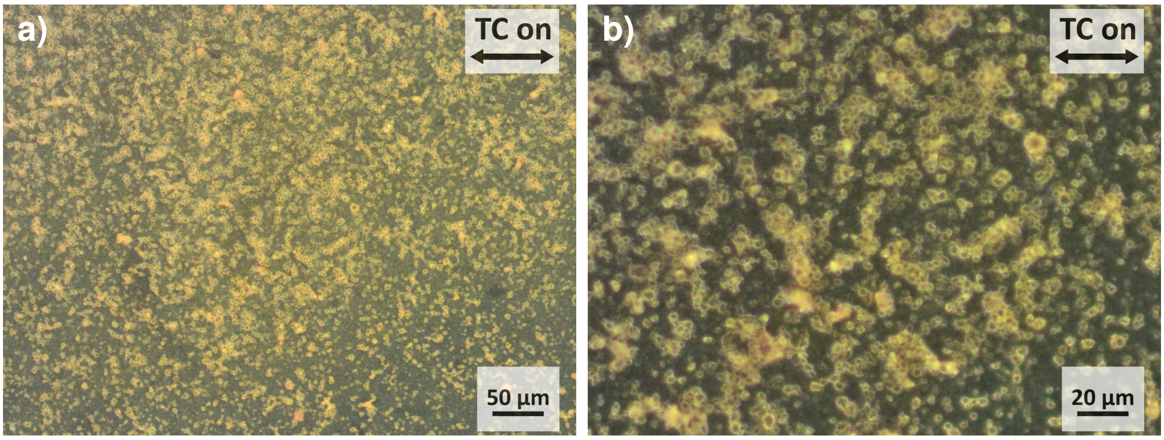

Figure 5.17: Drop-cast coating with 1 mg mL^{-1} solution of **5TG** in DCE in the electric field; (a) 20x (b) 50x.

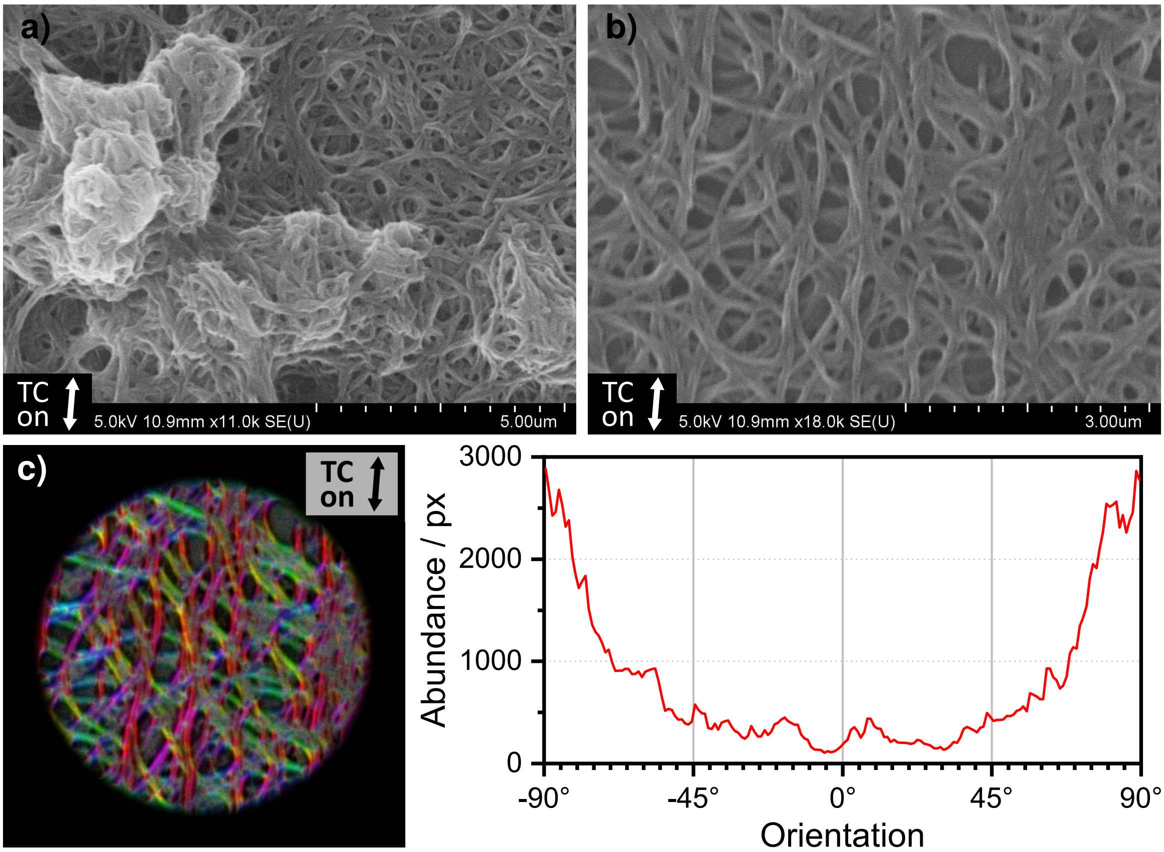

Figure 5.18: SEM images of the **5TG** coating depicted in Figure 5.17, the direction of the former electric field is nearly vertical, depicted in the lower left; (a) the particular shapes from the optical microscope images are hills of fibers, (b) the area in between is comprised of a flatter coating of fibers, (c) orientation analysis of image b) reveals a prevalent vertical orientation.

shows microscope images of the coating; they invoke the impression that particles are isotropically spread across the surface.

SEM images changed that impression, as seen in Figures 5.18 (a–b). Higher magnification revealed that the surface consists of fibrous structures, and the particles apparent by optical microscopy proved to be accumulated piles of fibers. As an exception, the electric field direction during drop-casting is approximately in the vertical (85°) in these cases. While orientation analysis showed a random orientation for Figure 5.18 (a), it revealed that indeed there is a prevalent orientation in the vertical direction in the case of Figure 5.18 (b). This has to be interpreted cautiously, as the prevalent orientation might result by chance. It was hypothesized that the aggregates were too dense to show a more expressed preferred orientation, so these solutions will have to be diluted further for more meaningful results. Unfortunately, **5TG** proved unstable under bench conditions, as the substance did neither dissolve in nor gelate DCE anymore, and the trials could so far not be repeated.

5.2.4 Teslaphoresis of NDI-C8

5.2.4.1 The Different Phases of NDI-C8

The compound **NDI-C8** was chosen because NDI-based compounds are often semiconductive.[125] The molecular structure is shown in Figure 5.19. It consists of a naphthalene diimide moiety, terminated on one end with a butyl chain. On the other end is a naphtho-crown-8 group connected to the molecule via a benzene spacer. The synthesis of the compound was done by H. Hupatz and M. Gaedke and is reported elsewhere.[126]

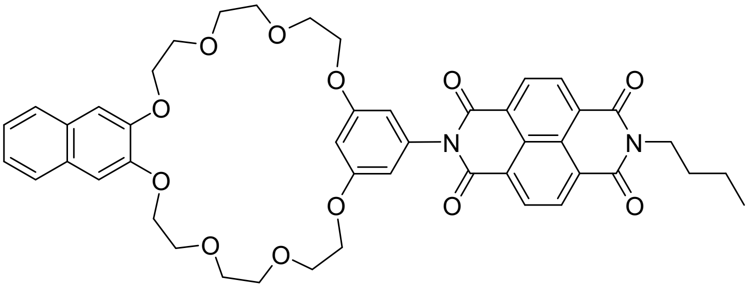

Figure 5.19: Structure of the naphthalene diimide derivative **NDI-C8**.

The compound offers interesting structural diversity depending on the solvent that is used to precipitate it from. If dissolved in a mixture of dichloromethane and methanol and precipitated by evaporation of the solvent mixture, it forms structures that comprise of micrometer-sized spheres. This structure is used in TC experiments in Chapter 5.2.4.2. If the compound is dissolved in pure MeCN and precipitated by evaporation of the solvent, much thicker, rigid needles form. These structures with a high aspect ratio are used in the electric field of the TC in Chapter 5.2.4.3.

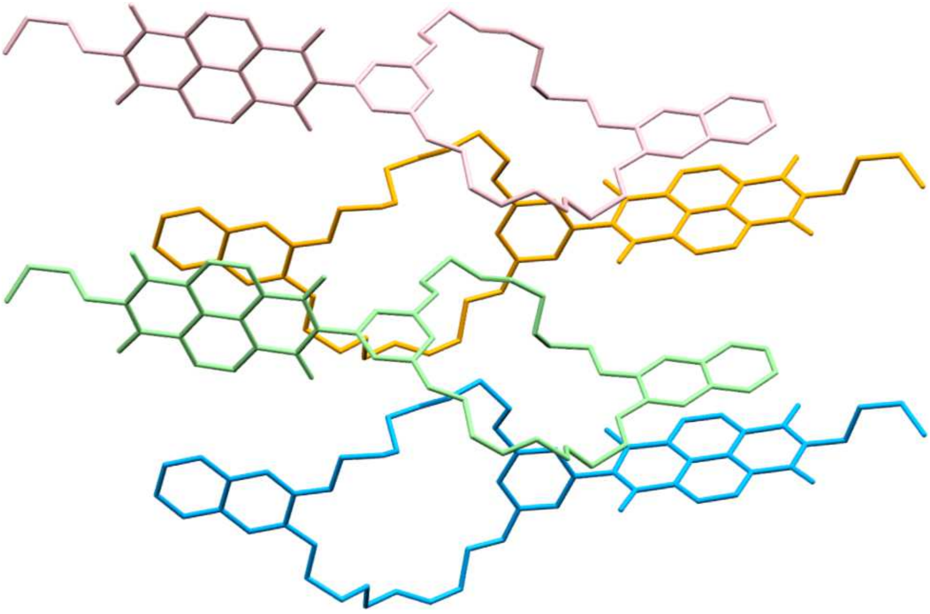

Figure 5.20: The structure of the naphthalene diimide derivative **NDI-C8**.[126] Shown are four molecules in different colors. Hydrogen atoms are omitted for clarity.

A crystal structure of **NDI-C8** was reported.[126] This was achieved by evaporation of a dimethylformamide (DMF) solution, which afforded orange single crystals. Four molecules are displayed in different colors in Figure 5.20. It can be seen that a naphthalene group interacts with the NDI moiety of the neighboring molecule. The naphthalene group of that molecule in turn interacts with the naphthalene moiety of the next molecule and so forth. The π dimers created in this fashion are offset from each other and there is no continuous π system.

The needles created by evaporation of an MeCN solution were not orange, but pale yellow. This is an indicator for crystallization in another phase than in DMF. The needles appeared very crystalline, but were too small for traditional single crystal X-ray diffraction (SCXRD). Instead, X-ray powder diffraction (XRPD) was measured. As comparison, a spectrum was calculated from the SCXRD results in DMF. Calculation and measurement were done by Prof. F. Emmerling. The comparison of the two diffractograms can be seen in Figure 5.21. It is obvious that the reflections differ drastically in their 2θ values. Therefore the conclusion can be drawn that the needles from MeCN exist in a different phase than the single crystals from DMF, although the exact structure remains unclear.

5.2.4.2 Teslaphoresis of NDI-C8 Spheres

Solutions of **NDI-C8** in DCM/MeOH 5:1 with a mass concentration of $1\,\mathrm{mg\,mL^{-1}}$ and volumes between $0.5-1.0\,\mathrm{mL}$ were created by aiding the dissolution with ultrasonication

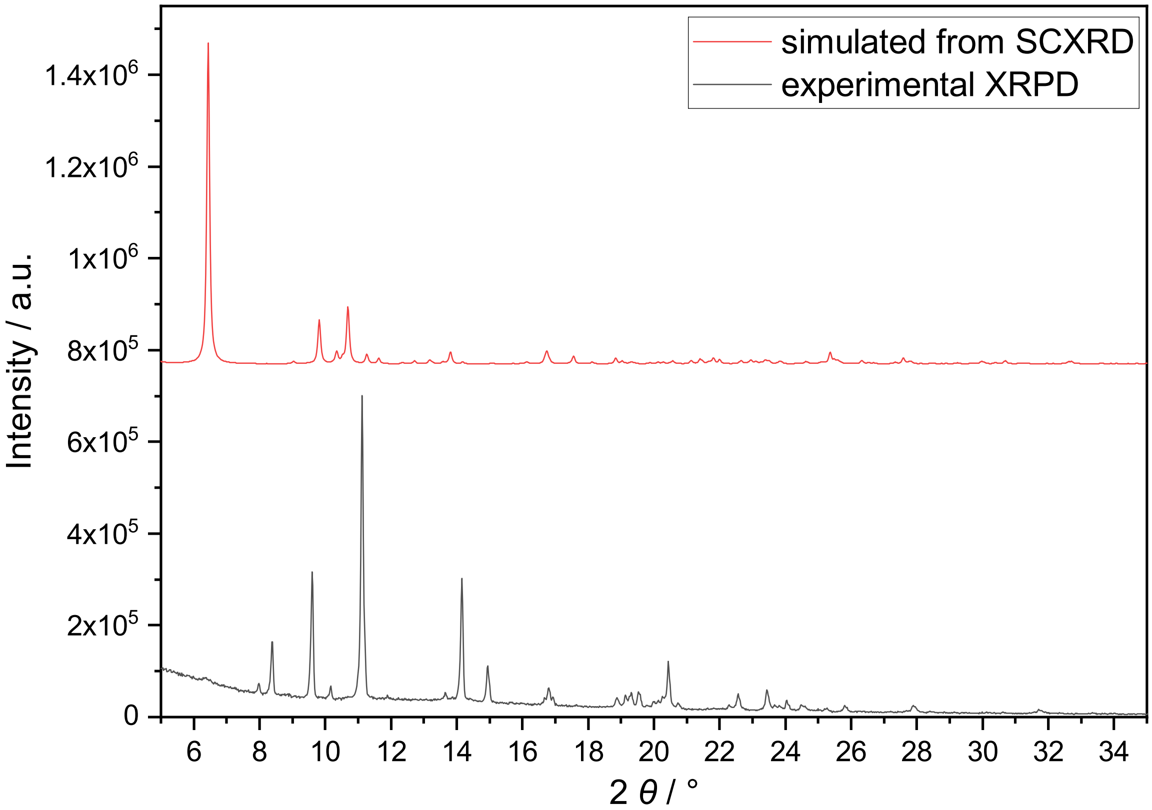

Figure 5.21: Comparison of the diffractogram simulated from the SCXRD of **NDI-C8** crystallized in DMF (red) and the experimental XRPD of **NDI-C8** needles from MeCN.

and heating. The vials were sealed, apart from a small puncture in the cap, and let stand for about 1 h under ambient conditions, until small aggregates formed visibly to the eye. Of the resulting mixtures, 20 µL were then drop-cast on glass cover slips. First shown are castings done without the TC being switched on. All other conditions were exactly the same as later with the powered TC.

Optical micrographs are shown in Figure 5.22. Upon higher magnification, it is apparent that the structures which—to the naked eye—appear fibrous, are actually conglomerates of separate microscopic spheres attaching to each other. This superstructural aggregation is either random or tangential to the outlines of the evaporating droplet. Around the center of the droplet, elliptical patterns are visible. This is shown in Figure 5.22 (a). These concentric ring-like formations presumably stem from the evaporation process. Figure 5.22 (b) shows the very edge of the droplet. Structurally dense areas reminiscent of headland are pointing inwards from the edge towards the center. Figures 5.22 (c) and (d) show an area of less density in higher magnification. Here, aggregation becomes more sparse, and aggregates are oriented randomly.

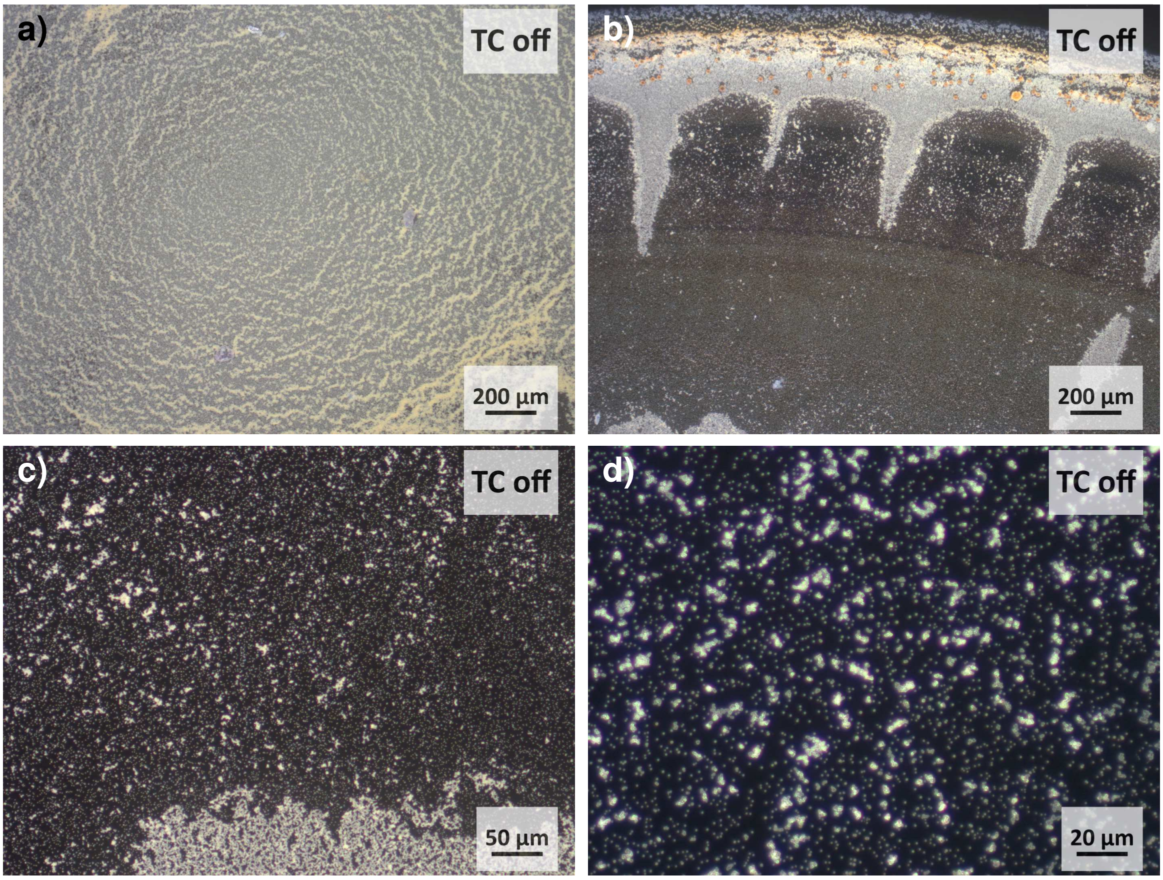

Figure 5.22: Shown are (a) the center of the droplet in 5x magnification, (b) the edge of the droplet in 5x magnification, (c) an area of less density between the center and the edge of the droplet in 20x magnification and (d) this less dense area in 50x magnification.

The image depicted in Figure 5.22 (c) was used for an exemplary orientation analysis, shown in Figure 5.23. It should be noted that, when observing an area away from the center of the droplet, structures created by evaporation can also appear as (local) anisotropy. This is the case for example when examining only parts of circular structures created by the droplet evaporation. Therefore, unless otherwise noted, the center of the droplet is used for orientation analysis, as it remains mostly free of such effects.

When the TC was switched on during the evaporation of the droplet, the morphology of the surface was different. Shown in Figure 5.24 is a panorama picture that was taken along the full width of the evaporated droplet for a better overview. The surface has areas of lower and higher structural density, with a denser strip spanning along the direction of the electric field. Figures 5.25 (a–c) show an area of lesser density at the left end of the droplet. Figure 5.25 (d) shows the structure in the center of the evaporated droplet, within a dense area. The direction of the electric field lines is horizontal in respect to the picture, with the TC antenna on the right side of the picture. It can be seen that the spheres aggregate primarily in horizontal direction, and form structures parallel to the electric field lines emanating from the TC.

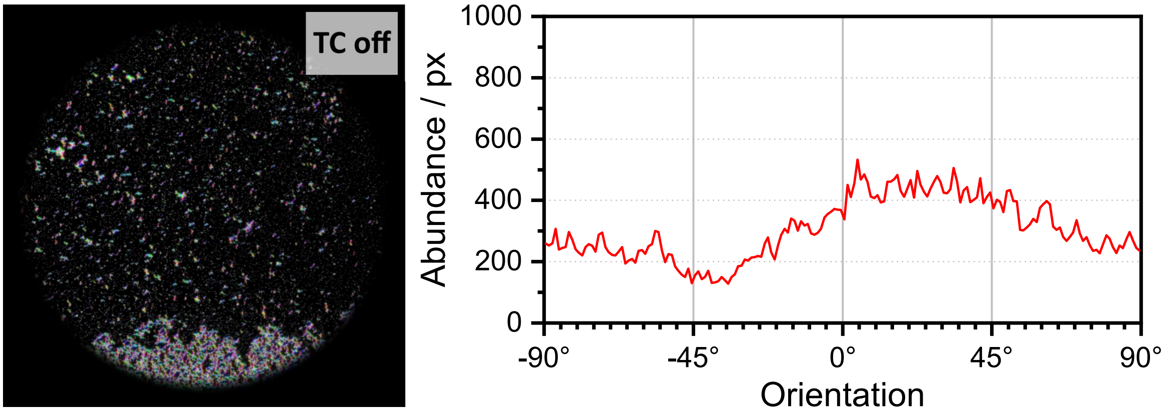

Figure 5.23: Exemplary orientation analysis of the surface achieved without the influence of the TC, shown in Figure 5.22 (c), Gaussian window σ = 2 px.

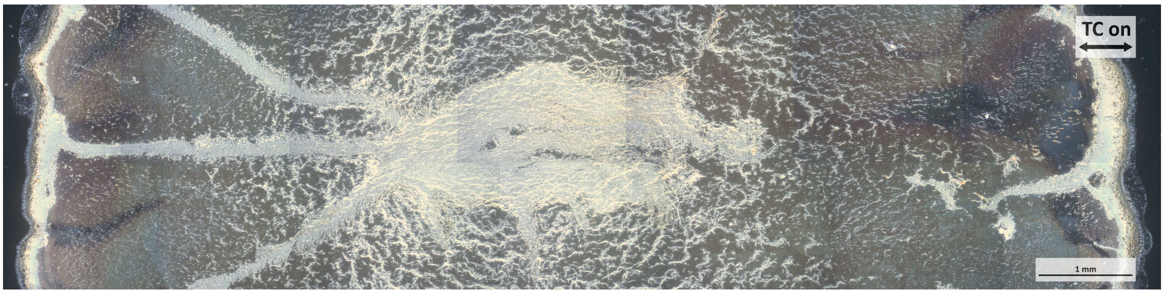

Figure 5.24: A panorama picture, tiled together from separate images taken at 5x magnification, showing a surface created by drop-casting **NDI-C8** spheres in the electric field of the TC. The electric field direction is in the horizontal.

To quantify this effect, orientation analysis of the images was carried out. In higher magnifications, the Gaussian window had to be set sufficiently high to avoid predominantly measuring the outside edge of the individual spheres, and to rather receive information about the orientation of the superstructures. The HSB maps are shown left of the orientation histograms in Figure 5.26. In all cases, the prevalent orientation was around 0°, which corresponds to the direction of the electric field lines. In the less dense area (shown in (a–c) of Figure 5.25 and Figure 5.26), the peak was comparatively sharp, while in the dense area—(d) in both Figures—a wave-like pattern formed, with equally prevalent angles between around −20° and 20°.

SEM images revealed an intriguing detail (Figure 5.27). Without the influence of the electric field, the spherical structures can be seen aggregating in random directions. This is shown in Figures 5.27 (a–b). Under the influence of the electric field, they do not just aggregate next to each other. They rather fuse together to create chains of capped sections of spheres, as seen in Figures 5.27 (c–d).

It is not clear what causes this fusion of the spheres. However, also for the surfaces cast without the influence of the TC, a similar effect could be observed in areas close to the

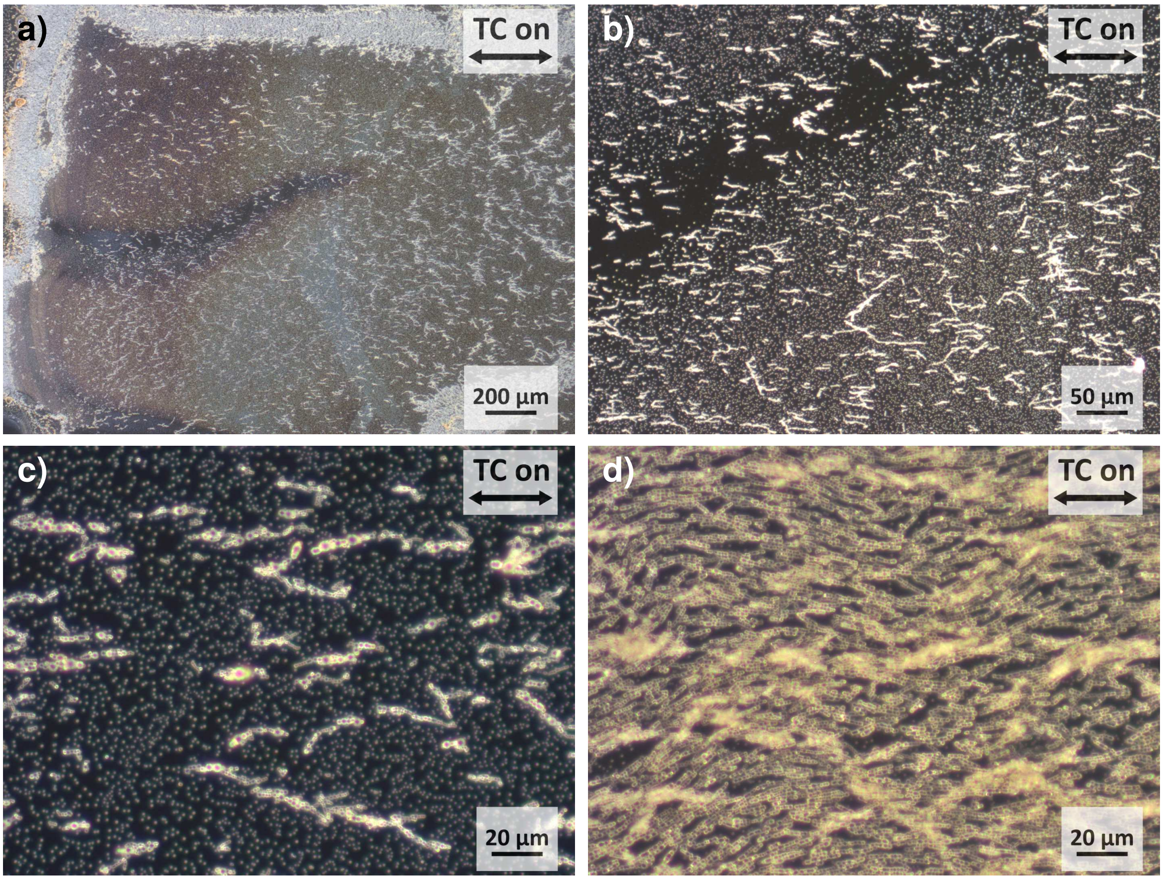

Figure 5.25: Drop-casting was repeated in similar conditions as in Figure 5.22, apart from the electric field being switched on. Detail images showing a surface created by drop-casting **NDI-C8** spheres in the electric field of the TC; (a-c) 5x, 20x, 50x magnification of a low-density area; (d) 50x magnification of a high-density area.

edge of the surface (Figure 5.28). In those areas, the coffee ring effect presumably caused a higher local concentration before complete evaporation of the droplet. On the basis of these observations, it seems that the fusion of the spheres stems from different local concentrations, and can be enhanced by the electric field of the TC.

Another finding from the SEM images was that the ability to either orderly aggregate or fuse the spheres is dependent on the sphere size. This was already indicated in optical microscope images, but SEM images allowed for a quantification of this phenomenon. Figure 5.29 shows an image of a fused chain of spheres and surrounding unconnected spheres. Manual measurement of the particles with ImageJ revealed that the unconnected particles have diameters 0.46–0.86 µm and an arithmetic mean diameter of 0.60 µm. The diameters of the fused particles are in the range of 0.58–4.32 µm and have a mean diameter of 1.21 µm. Therefore, the minimum size is only marginally different, while the maximum diameters differ vastly. Above 0.86 µm, all of the particles are aggregated.

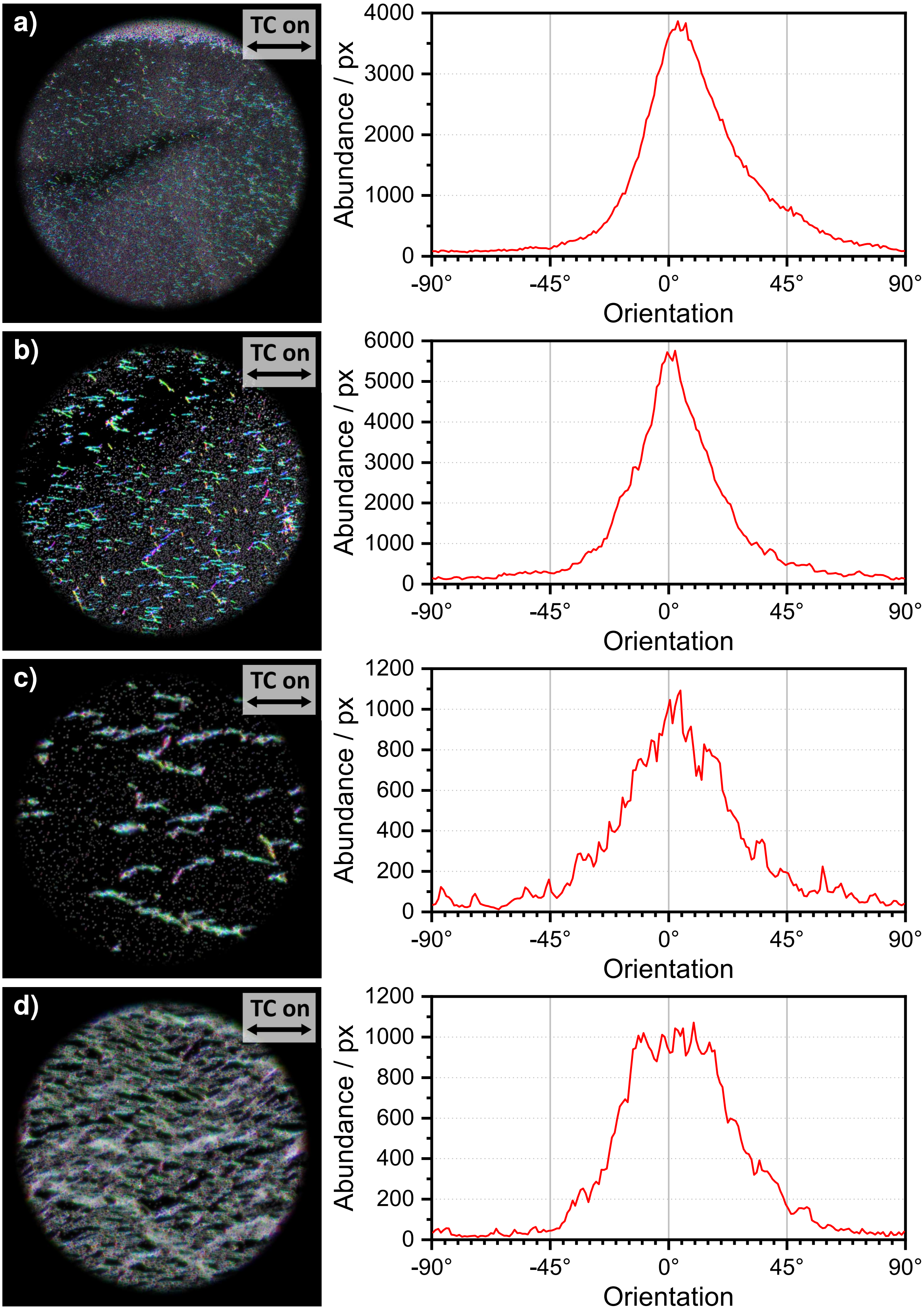

Figure 5.26: HSB maps and histograms of **NDI-C8** spheres drop-cast in the electric field, with the Gaussian window set to (a) σ = 1 px, (b) σ = 2 px, (c) σ = 3 px, (d) σ = 2 px.

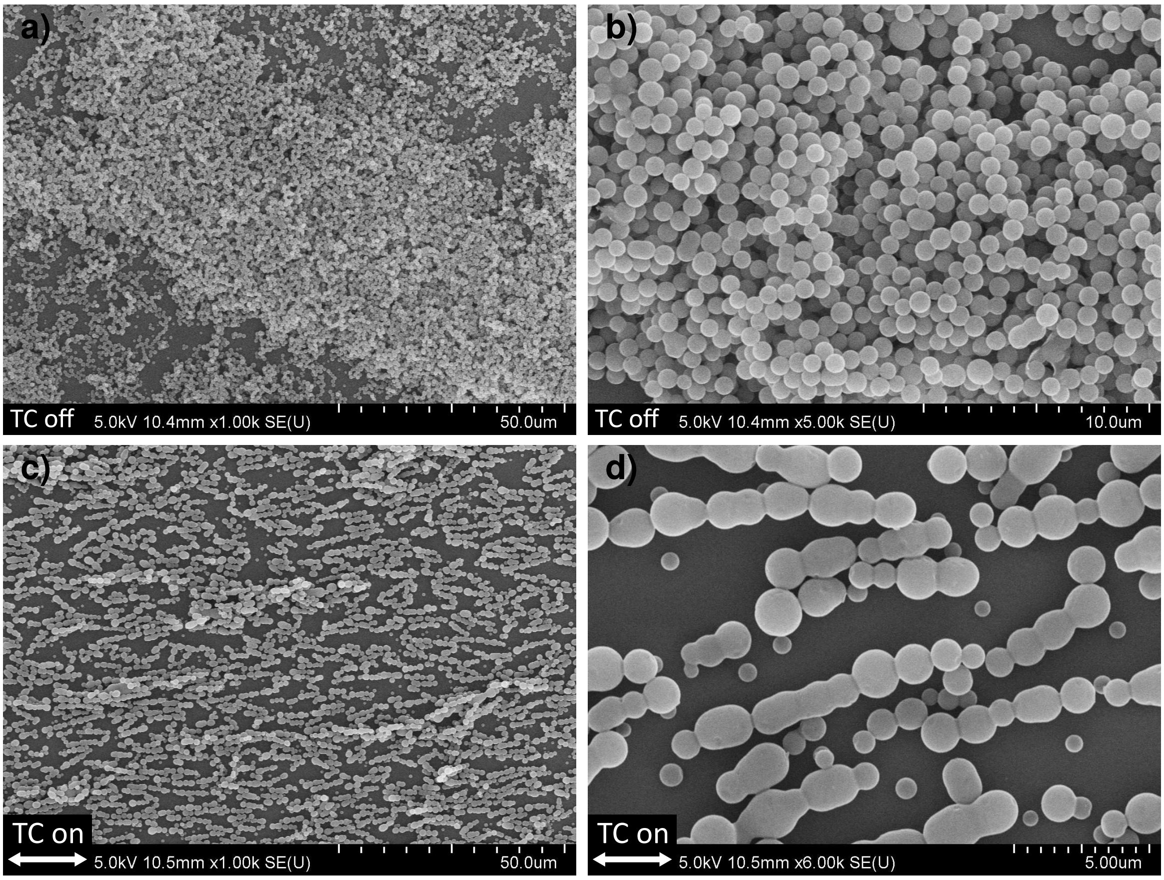

Figure 5.27: SEM images taken near the center of **NDI-C8** sphere surfaces created either a–b) without and c–d) with the influence of the TC. It becomes clear that in the ordered surfaces, the spheres do not just aggregate next to each other, but rather fuse into chains of capped sections of spheres.

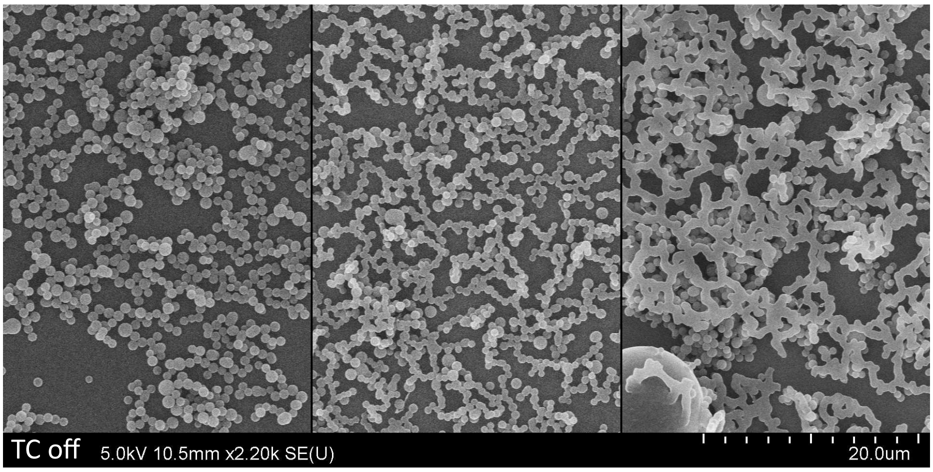

Figure 5.28: SEM images taken of the **NDI-C8** sphere surface created without an electric field. Left: center of the dried droplet; middle: area close to the edge; right: edge.

A process which might explain the elongated shape of the larger particles is Ostwald ripening. It denotes a phenomenon where small particles shrink and large particles grow, due to diffusion of molecules onto the larger aggregates. This takes place for two reasons. One is, that smaller particles are more soluble (this is called the Kelvin effect).[135] In addition, the process leads to lower overall interfacial energy in the system.[136] If particles are aligned next to each other, the crevices in between the spheres might offer a better position for redeposition, as there is less contact area with the solvent and more with the substance. Ultimately, this might lead to the fusion of the spheres.

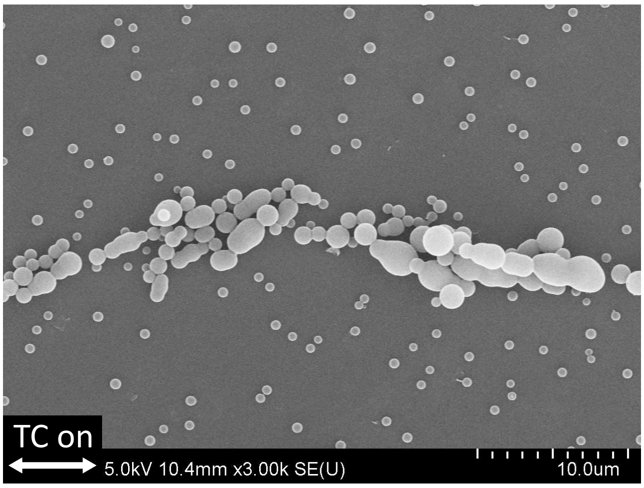

Particles	d_{min}	d_{max}	$\overline{d}$
Single	0.46	0.86	0.60 ± 0.08
Connected	0.58	4.32	1.21 ± 0.49

Figure 5.29: SEM images of fused and non-fused **NDI-C8** spheres and size comparison of the structures, numbers in µm.

5.2.4.3 Teslaphoresis of NDI-C8 Needles

When changing the solvent, **NDI-C8** did not precipitate as microscopic spheres but as elongated, rigid needles. **NDI-C8** was suspended in acetonitrile (1 mg mL^{-1}), dissolved by sonication and heating and let cool to room temperature. Sealing the container apart from a small puncture in the cap and letting it stand overnight produced precipitation in the form of pale yellow needles. Of this mixture, 20 µL were drop-cast on glass cover slips. Microscope images of the structures can be seen in Figure 5.30. The larger needles, that were precipitated overnight, are accompanied by amorphous precipitate and smaller needles growing concentrically outwards of several separate nuclei. These presumably grew during the drop-casting process. Figure 5.30 (a) shows the needles cast without the influence of the electric field. Figure 5.30 (b) shows a surface with needles cast with the TC active. When comparing the two images and their orientation analyses, no effect of the electric field of the TC can be seen.

However, while the large needles did not align, medium sized needles formed by the same process showed a higher inclination to align parallel to the electric field. Figure 5.30 (c)

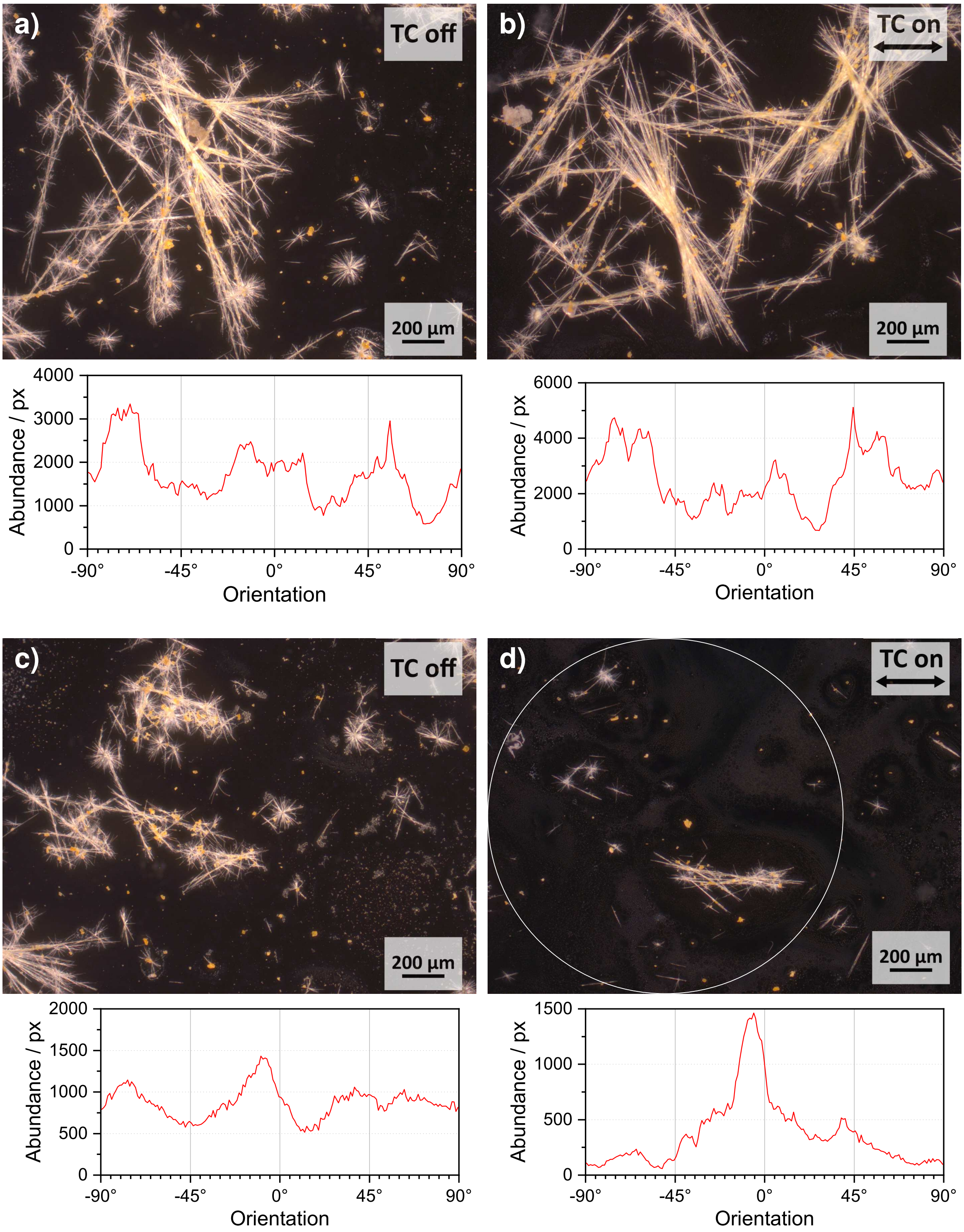

Figure 5.30: **NDI-C8** needles generated by ultrasonic and heat assisted solvation in MeCN, subsequent precipitation by slow evaporation of solvent and drop-casting in the electric field of the TC. Shown are the micrographs and their orientation analysis underneath. (a) Larger needles generated in this fashion, without the influence of an electric field, 5x magnification, σ = 2 px, (b) large needles drop-cast within an electric field, 5x magnification, σ = 2 px, (c) smaller sized needles without an electric field, 5x magnification, σ = 1 px, (d) smaller sized needles in the electric field, 5x magnification, σ = 1 px. In the last case, orientation analysis was not carried out within a circle fitted to the center of the image, but within a left-bound circle, as illustrated.

shows medium sized needles cast without the electric field, while Figure 5.30 (d) shows the result of casting in the electric field. The orientation histogram quantifies what is visible to the eye, that the needles of this certain size are predominantly aligned parallel. This indicated that the larger needles might be too heavy to move in the electric field, and a reduction of the needles to smaller pieces could yield the desired results.

Therefore, the prepared mixture with the precipitated needles was sonicated for 2 s and immediately afterwards drop-cast. The results are shown in Figure 5.31. Without the electric field, the shortened needles were in a disordered state throughout the surface, as seen in Figure 5.31 (a). With the electric field active, and all other conditions identical, the needle fragments ordered themselves preferentially parallel to the electric field lines, as seen in Figure 5.31 (b). To illustrate that this effect is consistent in a large area, Figure 5.31 (c) shows a photograph taken through the ocular of the microscope.

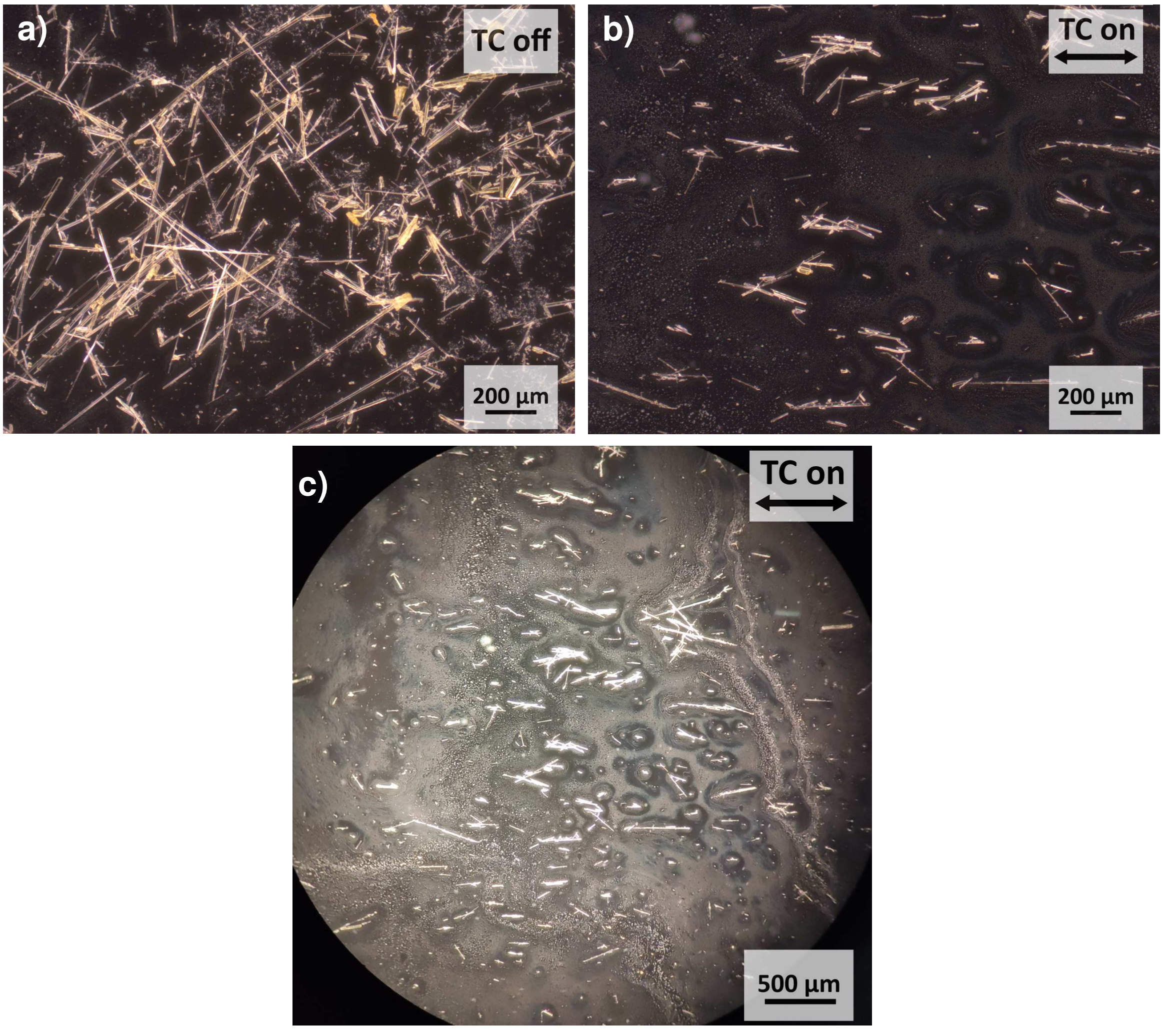

Figure 5.31: Control experiment to illustrate the difference between a sample of **NDI-C8** needles sonicated for 2 s, 5x magnification, (a) without the influence of the electric field, (b) under the effect of the TC. (c) A photograph was taken through the ocular to illustrate the scale of the visible effect.

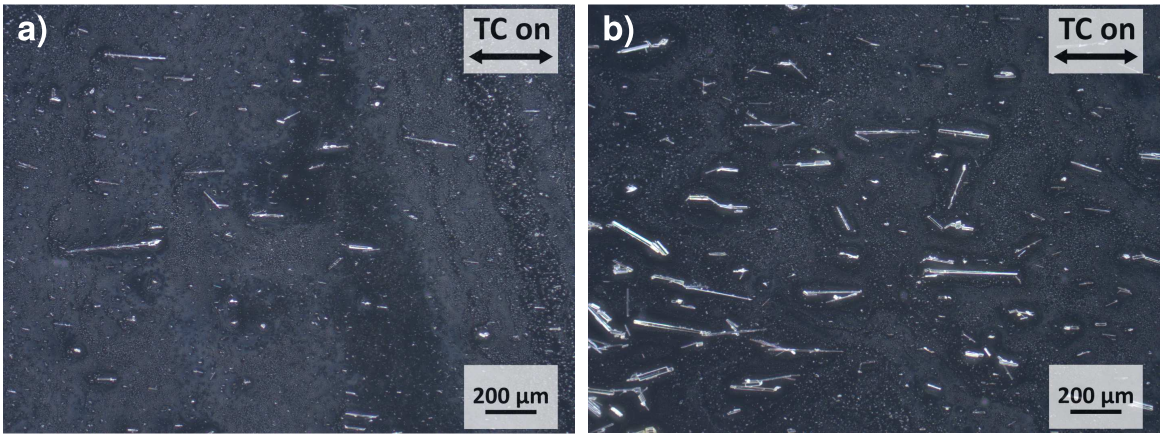

Figure 5.32: The precipitated **NDI-C8** needles were sonicated for 2 s to reduce their size and weight. Drop-casting in front of the TC showed a repeatable obvious effect of the electric field, 5x magnification; (a) surface cast with a medium amount of broken needles from the middle of the vial, (b) a sample with more precipitate from the bottom of the vial, showing higher structural density.

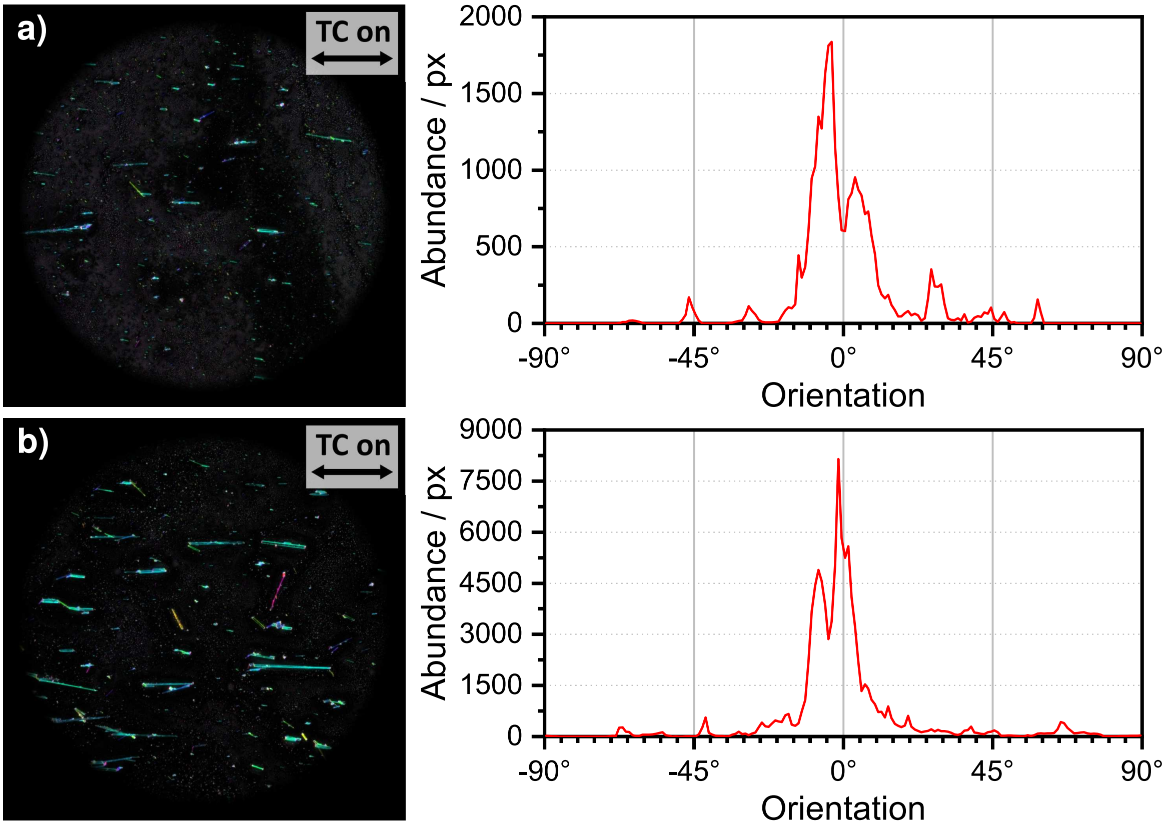

Figure 5.33: HSB maps and histograms of drop-cast **NDI-C8** needles after sonication, with the Gaussian window set to 3 px, 5x magnification; (a) with less precipitate, (b) with more precipitate.

It was tried to vary the structural density of the surfaces by transferring substance from different areas of the vial. Figure 5.32 (a) shows a surface created by drop-casting a lower amount of sonicated needles from the middle of the vial, while in Figure 5.32 (b) the precipitate from the bottom of the vial had been transferred, yielding more substance on the surface. Figure 5.33 shows the orientation analysis of the structures. The histograms show consistent maxima in the area of around −10° to 10°, which is in line with the electric field direction.

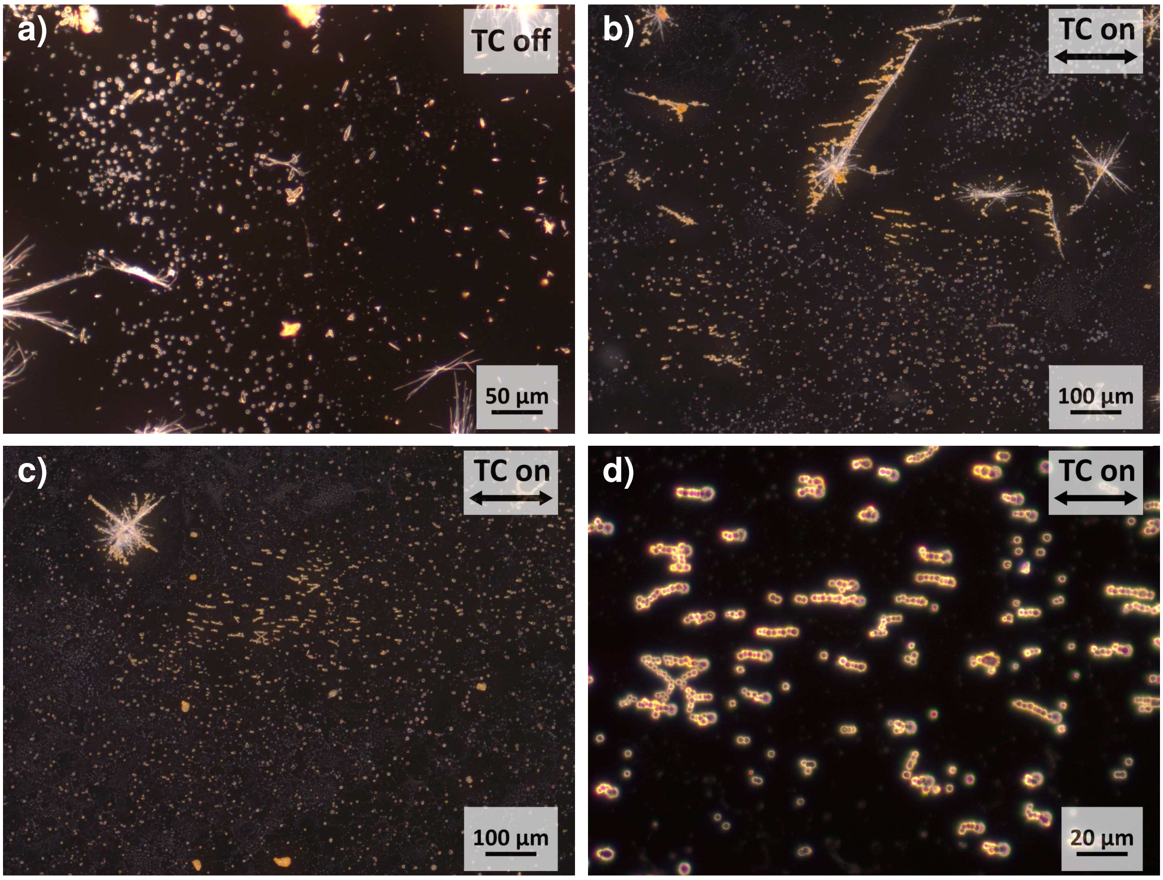

Figure 5.34: Circular aggregates **NDI-C8** created during the trials which mainly focused on the predominantly formed needles. Spheres formed in areas close to the border of the dried droplets; (a) no electric field: circular structures without horizontal aggregation, 20x magnification; (b) the electric field presumably forced circular structures apart from the needle around which they formed, 10x magnification; (c-d) detail micrographs of the spherical structures influenced by the electric field, in 10x and 50x magnification, respectively.

During the trials with the **NDI-C8** needles, another intriguing phenomenon appeared. In the fringe areas of surfaces cast without prior sonication round shapes were observed. These were comparable to the ones created in methanol/dichloromethane (discussed in Chapter 5.2.4.2). Figure 5.34 (a) shows these structures without the influence of the electric field. Figures 5.34 (b–d) show the structure under the influence of the electric field while casting.

In Figure 5.34 (b) it can be seen that the small structures are influenced by the electric field and were pulled them away from a needle, around which they presumably first aggregated.

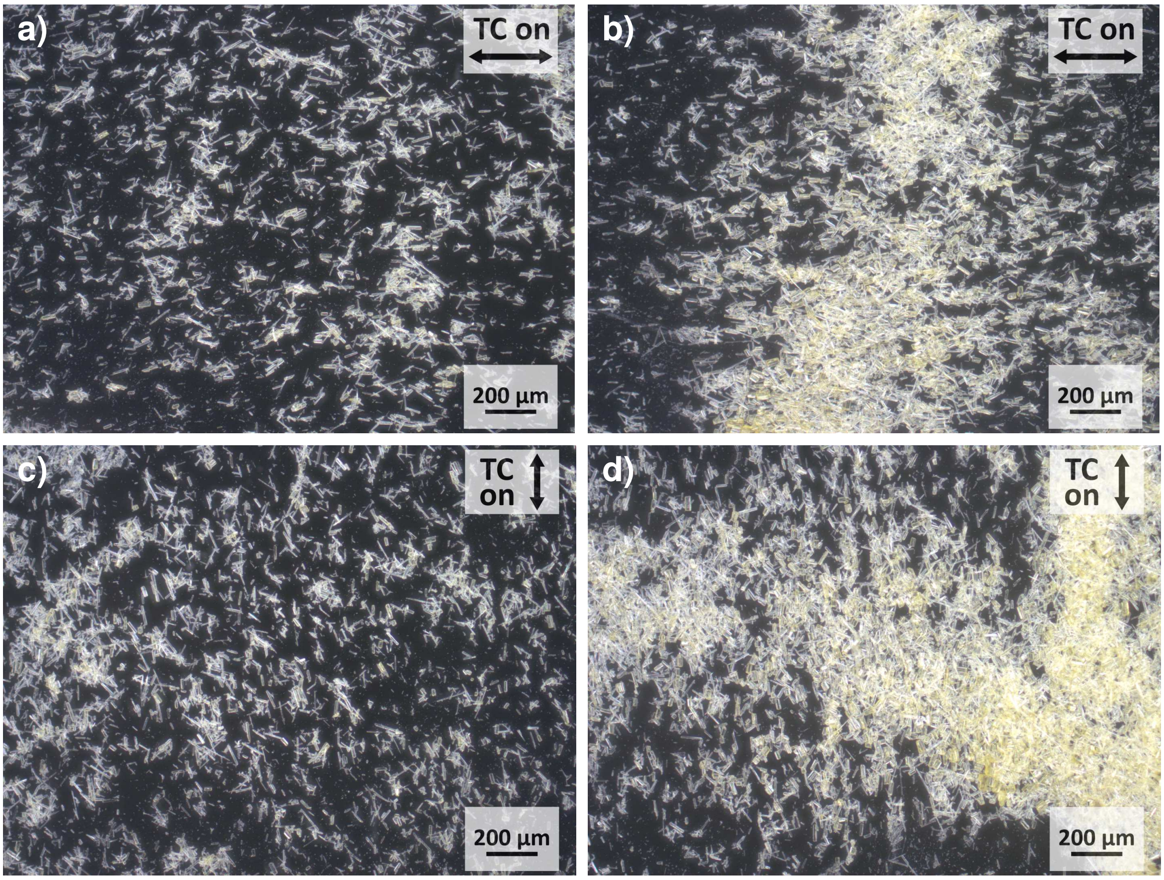

Figure 5.35: Surfaces generated with **NDI-C8** needles which were sonicated for 2 min prior to drop-casting in the electric field. The micrographs were taken with the electric field lines during drop-casting aligned to the horizontal as well as the vertical axis of the picture, 5x magnification; (a) field lines during drop-casting in horizontal axis, lighter area, (b) horizontal, denser area, (c) vertical, lighter area, (d) vertical, denser area.

The orientation analysis algorithm was put to the test in the following case. A sample of **NDI-C8** needles was sonicated for 2 min before drop-casting, with the prospect of generating more regular surfaces consisting of smaller needle fragments. Normally, images were taken at the center of the droplet. In this case, there were areas with more structures (called "denser") and with fewer structures (called "lighter") adhered to the surface. As both areas were close to the center, micrographs were taken of each. Sonication had reduced the aspect ratio of the precipitate drastically, so the effect of the TC was less obvious on the individual structures. Nevertheless, orientation analysis was carried out and again confirmed a prevalent orientation of the structures parallel to the direction of the electric field. In these cases, the effect was not instantly obvious to the naked eye. To test the reliability of the computational method and to ascertain that there is no bias of the algorithm towards horizontal structures, a trial was carried out, in which the microscope images were either taken in the familiar way,

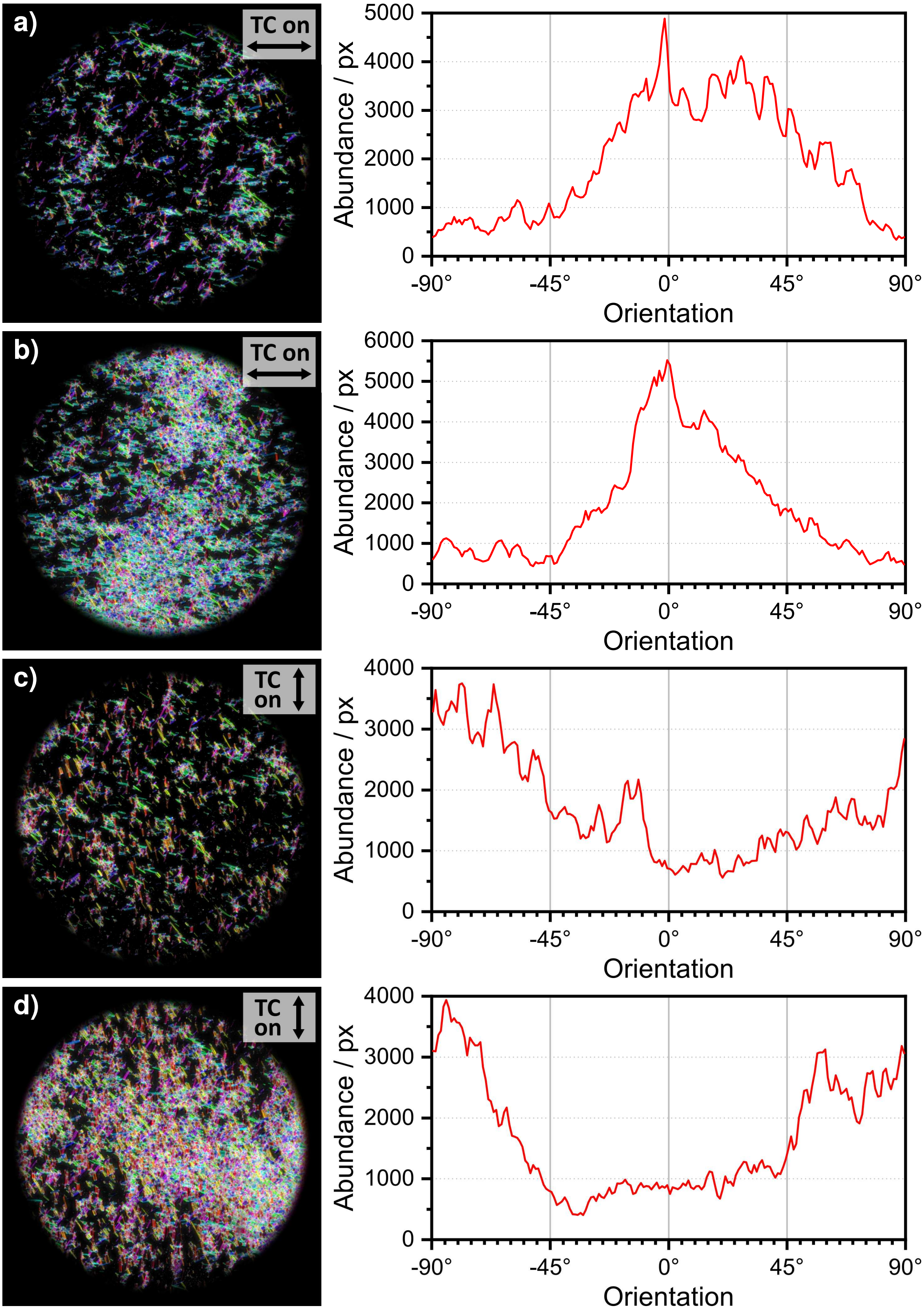

Figure 5.36: Orientation analysis of the micrographs depicted in Figure 5.35, σ = 2 px. (a) Field lines during drop-casting in horizontal axis, lighter area, (b) horizontal, denser area, (c) vertical, lighter area, (d) vertical, denser area.

with the electric field lines during drop-casting aligned to the horizontal axis of the picture, or additionally with the electric field lines aligned vertically in respect to the picture. The images are shown in Figure 5.35, the orientation analyses are depicted in Figure 5.36.

The results confirm that there is no bias of the algorithm towards a particular orientation, as the histograms are congruent with each other. When there was a horizontal alignment of the electric field lines, maxima are close to 0°, while for vertical alignment the maxima are close to 90°.

5.3 Chapter Summary: Use and Limitations of Teslaphoresis

In this chapter, two TESLA coils and their assemblies have been described. One model is built from the ground up, with the exception of the power source. The other model is a modification of an inexpensive, commercially available TC and can be replicated by exchanging the antenna for one described in this work. Both models worked, the first one is more resilient but less effective, while the second model is more effective but more prone to burning out. Most of the trials have been done with the second model and should therefore be able to be easily reproduced.

Several approaches to advance the development of anisotropic surfaces via teslaphoresis have been presented. Some compound/solvent combinations show an obvious influence of the electric field that was generated. Other combinations did not react to the electric field, but reduce the future margin for error by showing the limitations of the technique.

Table 5.4 shows solvents ordered by polarizability. The values are experimental values taken from the “Computational Chemistry Comparison and Benchmark DataBase”[104]. After the trials undertaken so far, the results are in line with the limitations of dielectrophoresis covered in Chapter 3.5: A low polarizability of the solvent is beneficial. This can be a disadvantage when working with organic compounds, as solvents of low polarizability are often of high polarity. When utilizing this new technique, other solvent restrictions have to be taken into account as well. The solvent needs to evaporate at room temperature and quickly enough to prevent an overheating of the electric apparatus. And last but not least, the solvent should be of low toxicity. Working within ventilated hoods is not possible, as the electric field of the TC can endanger electric circuits approximately a meter away from the antenna, and should therefore not be within the reach of conductive materials.

The most promising solvent for these trials was acetonitrile, with a low polarizability, compatibility with organic substances, good evaporation behavior and low toxicity. Water was of

Table 5.4: Solvents used in TC experiments, sorted by polarizability, and whether the substances solved or suspended within have proven susceptible to the electric field.

Solvent	Polarizability[104] / Å^3	Susceptible
Water	1.50[105]	yes
Methanol	3.21[106]	yes[a]
Acetonitrile	4.28[106]	yes
Dichloromethane	6.66[106]	yes[a]
2-Propanol	6.67[106]	no
1,2-Dichloroethane	8.00[106]	unclear
Carbon disulfide	8.75[104]	weakly[b]
n-Hexane	11.63[106]	no
Toluene	11.86[106]	no

[a] MeOH and DCM were positively tried only in combination; it is possible that during the drop-casting process the less volatile MeOH enabled susceptibility

[b] CNTs showed only slight alignment

disadvantage, as the higher boiling point and higher enthalpy of vaporization caused droplets to linger up to half an hour before evaporation, in addition to its obvious disability to solubilize or even suspend many organic compounds. Dichloromethane and methanol only yielded desired results in cases when a combination of both solvents was used. In those cases, it is not clearly dismissable, that methanol—as the less volatile solvent with the lower polarizability—remained during evaporation and enabled the influence of the electric field. The solvent with the highest polarizability that has successfully been tried is carbon disulfide, although it enabled the orientation of carbon nanotubes only weakly. The two solvents with higher polarizabilities, hexane and toluene, yielded no desired results.

Table 5.5: A list of compounds in order of appearance in this work, and their susceptibility towards the TC so far.

Compound	Susceptibility	Chapter
CNTs and derivatives	yes	5.2.2
Diamide gelator **CF7**	no	5.2.3.1
Dipolar compound **1**	no	5.2.3.2
Pyrene compounds **2–4**	no	5.2.3.3
Oligothiophene **5TG**	unclear	5.2.3.4
NDI-C8 spheres	yes	5.2.4.2
NDI-C8 needles	yes	5.2.4.3

Table 5.5 shows an overview of the compounds utilized within the scope of this work. With the largest π systems, the CNTs are still the compounds that are most receptive towards the electric field of the TC. Fluorination seems to diminish the susceptibility to the TC in

carbon disulfide, but in Pluronic water and acetonitrile, it does not change the receptivity compared to non-substituted carbon nanotubes, by qualitative estimation. A surprising class of compounds was found to be susceptible to the TC as well: The crown ether substituted NDI derivative **NDI-C8** can, depending on the solvent, precipitate in different shapes. Either as spheres of roughly 0.5–5 µm in diameter if drop-cast from a mixture of dichloromethane and methanol. Or as needles with strongly varying sizes (with diameters mostly in the range of 1–10 µm and lengths up to hundreds of micrometers) if precipitated in acetonitrile. While drop-casting, both kinds seem to be influenced by the electric field and afford superstructures parallel to the electric field lines. Although these surfaces generated are not yet densely enough coated to test for anisotropic properties like directional wettability, it is a step into the direction of combining this technique with other materials.

An initial assumption, that the structures need a high aspect ratio to be susceptible to the electric field, needs to be revised: The **NDI-C8** spheres have spherical symmetry and therefore an aspect ratio of unity and yet aggregate in the direction parallel to the electric field. It is unclear whether **NDI-C8** on the surface exhibits semiconductivity. A crystal structure measured in the past with a single crystal from DMF showed a discontinuous π system. Powder diffraction on the **NDI-C8** needles used in this work showed that the compound crystallizes differently from acetonitrile, and shows different patterns. Therefore, it might be possible that the material exhibits a continuous π system and higher charge mobility.

Overall, the scope of compounds showing a response to the electric field of a TC could be expanded from solely CNTs to small organic molecules in the case of **NDI-C8**. In the case of **5TG**, further control experiments are needed, but first results seemed promising. Carbon nanotubes can show differently strong reactions to the field when fluorinated, which presumably originates from the resulting lower polarizability. This presumably depends on the polarizability of the solvent itself.

6 Perfluorinated Side Chain Length Effects in Supramolecular Xerogels

6.1 Motivation

In previous work conducted by Q. WEI and C. SCHLAICH in the SCHALLEY group[7,137], it was found that compound **CF7**, consisting of a cyclohexane ring substituted at 1,2-position with amide groups and perfluorinated *n*-heptyl chains, gelated in diethyl ether. When a gel of this compound and diethyl ether was drop-cast onto a glass surface and the solvent evaporated, a fibrous xerogel remained on the surface. This xerogel adhered surprisingly stably onto the surface and most notably, led to superhydrophobic properties. Even under a continuous water stream, it stayed affixed to the substrate. This seems counterintuitive, considering the contrast between the large and non-polar perfluorinated moieties of **CF7** and the polar properties of glass, which consists of SiO_2 and free OH groups at the interface.

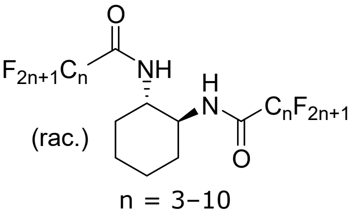

Figure 6.1: The basic scaffold of compounds **CF3**–**CF10**.

When instead of the perfluoroheptyl side chains, perfluoropropyl chains were used, the compound (**CF3**) did not gelate anymore. Therefore, upon evaporation, no fibrous network remained. This compound precipitated in the form of more rigid and short aggregates. Consequently, the stability of the coating on the surface was lower and it was washed away easily in comparison.

These previous findings lead to a larger scale comparison of different side chain lengths conducted within this work. The morphology, water-repellent properties and stability on the surface of the aforementioned compounds with perfluorinated side chain lengths ranging from three to ten carbon atoms will be investigated. The structures are shown in Figure 6.1.

Furthermore, H. SATO and co-workers noticed an odd-even effect when working with similar compounds, as stated in the background of this work. The critical gelation temperature of the enantiopure analogues of compounds **CF6–CF9** exhibited an alternation in hexafluorobenzene: low - high - low - high. The racemic compounds did not exhibit this effect. In this work, diethyl ether will be used, therefore other structures are likely to be present. Not the gelation temperature, but rather the hydrophobicity and stability of the created coatings will be investigated for an odd-even effect.

6.2 Synthesis of Compounds CF3–CF10

Compounds **CF3–CF10** were synthesized with the acid chloride of the side chains. Depending on commercial availability, either directly from the acid chloride (**CF3** and **CF6–CF8**), or by first creating the acid chloride from the carboxylic acid (**CF4**, **CF5**, **CF9**, **CF10**). The reactant for the core part was in all cases (±)-*trans*-diaminocyclohexane (DACH).

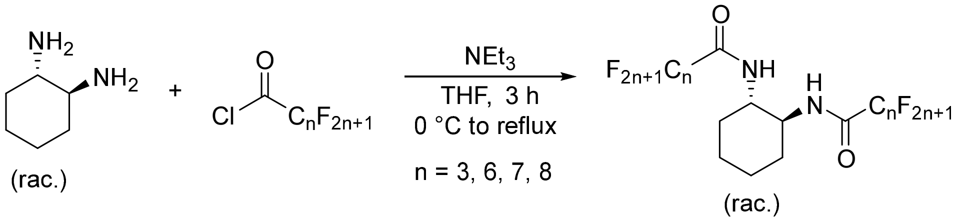

Scheme 6.1: The reaction scheme based on the acid chloride, leading to **CF3** (60 % yield), **CF6** (75 % yield), **CF7** (87 % yield), **CF8** (82 % yield).

The reactions with the fluorinated carboxylic acid chlorides are shown in Scheme 6.1. Under inert conditions, DACH was dissolved in THF and NEt_3 was added. The acid chloride of respective chain length was dissolved in THF and added dropwise at 0 °C. The mixture was heated to reflux conditions and a white precipitate formed visibly. After three hours of heating, this precipitate was collected by filtration. After the washing procedure, the yields were in the range of 60−82 %.

The remaining compounds were synthesized with the respective commercially available fluorinated carboxylic acids. These were dissolved in THF and excess thionyl chloride was added to convert the acid to the acid chloride. From this point on, the details of the syntheses for the different compounds diverged, due do improvements between the iterations. A generalized reaction procedure is shown in Scheme 6.2.

For **CF4**, after thirty minutes at room temperature, the mixture was added to a solution of DACH and NEt_3 in THF at 0 °C. The mixture was then stirred for 22 h at room temperature. After filtration and washing, this route afforded 15 % yield.

For **CF5**, after stirring the carboxylic acid and thionyl chloride for thirty minutes at room temperature, excess thionyl chloride was removed *in vacuo*, together with side products and

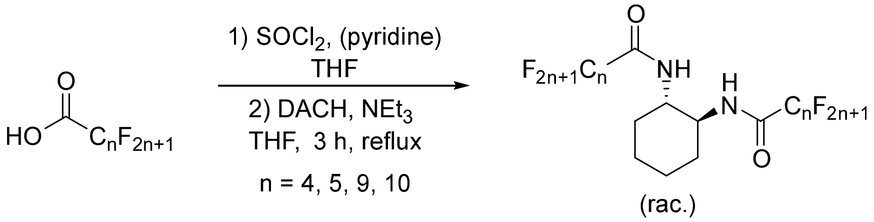

Scheme 6.2: The reaction scheme starting from the carboxylic acid. For **CF4** and **CF5**, no pyridine was added, and the reactions yielded 15 % and 11 %, respectively. The procedure was improved and pyridine added for **CF9** and **CF10**, which yielded 64 % and 71 %, respectively.

the solvent. The resulting acid chloride was dissolved in THF and added into a solution of DACH and NEt_3 in THF. After three hours of heating to reflux temperature, the usual washing procedure afforded **CF5** in 11 % yield.

For **CF9** and **CF10**, the carboxylic acids were added together with pyridine and an excess of thionyl chloride, with no additional solvent. After heating to 85 °C for two hours, the thionyl chloride, along with side products and solvent, was removed *in vacuo* while heating to 80 °C. The resulting acid chloride was dissolved in THF, added to a solution of DACH and NEt_3 in tetrahydrofurane and heated to reflux temperature for three hours. The usual washing procedure afforded **CF9** in 64 % and **CF10** in 71 % yield. This method proved most effective and might offer higher yields for the other compounds as well.

6.3 Comparison of the Melting Points

The most mentioned property when discussing the odd-even effect is the melting point, because the effects are most expressed in the solid state. The homologous series of the alkanes shows a stepwise increase of melting points from odd to even numbers, but a stagnation from even to odd numbers. To test for an odd-even effect, the melting points of **CF3–CF10** were measured. The compounds were dissolved in Et_2O, which was evaporated again. This was done because in trials shown later, Et_2O is used for the coatings, in case the solvent influences the solid state and thus the melting points. The results are shown in Table 6.1 and Figure 6.2.

Compounds **CF3–CF5** do not possess a melting point at atmospheric pressure. Gradually increasing sublimation speeds could be observed for increasing temperatures. The number given corresponds to the temperature at which the fine powder cleared from the walls of the capillary. At a certain temperature, the compounds changed color from white to yellow to brown. **CF5** melted in the moment of color change (225 °C), turning into a brown liquid. It is not clear if the decomposition product melts, lowers the melting point, or **CF5** itself

Table 6.1: Melting, sublimation and decomposition temperatures.

Compound	Melting range/°C	Sublimation / °C	Decomposition / °C
CF3		230	265
CF4		220	245
CF5	(225)[a]	210	225
CF6	210.1–210.3		
CF7	197.5–198.3		
CF8	189.8–190.6		
CF9	188.5–188.8		
CF10	184.4–185.3		

[a] Melts during decomposition.

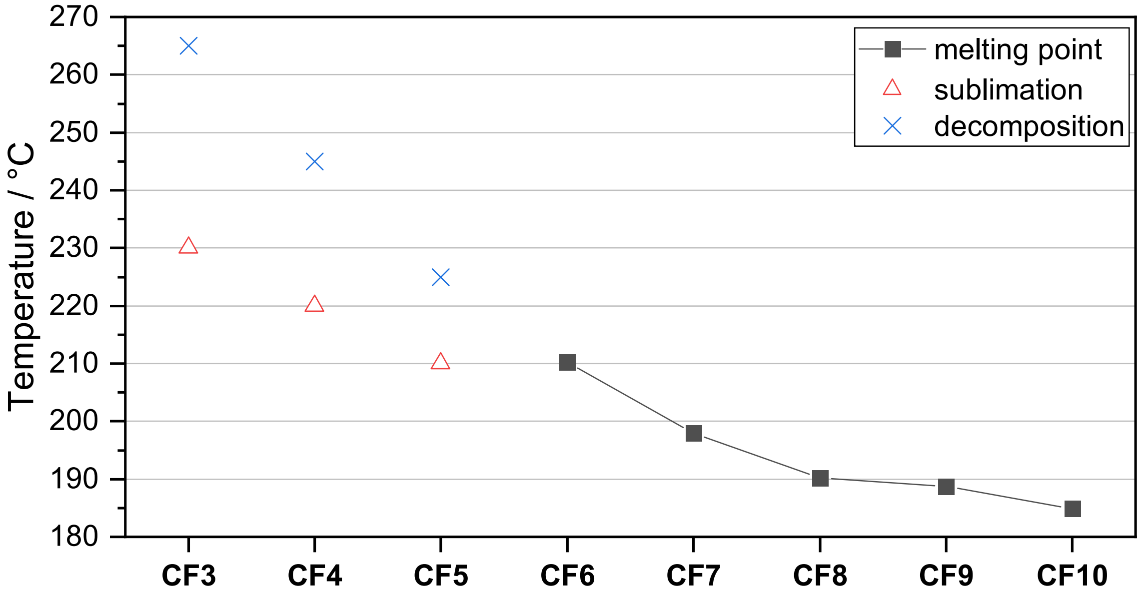

Figure 6.2: The plotted data of Table 6.1. The melting point is the average of the measured melting range.

melts at this temperature. It can be seen that sublimation and decomposition temperatures decrease in a linear fashion with increasing temperature.

For **CF6**, slight sublimation is visible, but the compound melts before the walls of the capillary become clear. Like the decomposition and sublimation temperatures, the melting range decreases with increasing chain length. This is contradictory to what is expected from non-fluorinated alkyl substituents. There, dispersion forces cause stronger intermolecular interactions and higher melting points with increasing chain lengths. Here, the melting ranges decrease approximately linearly with increasing side chain length until **CF8**, stagnate to **CF9** and decrease slightly to **CF10**. As the side chain length increases, the only weakly interacting perfluorinated fraction of the molecule increases, while the stronger H-bonds between the amide groups and the dispersion forces between the cyclohexyl moieties provide less interaction per molecule volume. Overall, no odd-even effect in melting points could be observed.

6.4 Coating Morphologies on Glass

Surfaces of the compounds were created by drop-casting according to the details given in the experimental section. Macroscopic examples of the structures created on glass cover slips are shown in Figure 6.3. The coated surfaces were analyzed by optical microscopy. The given magnifications denote the objective that was used; the actual magnification can be deducted from the scale bar. Scanning electron microscopy was used for more detailed structural information. The macroscopic appearance of the coatings was photographed with a classical camera. Specialized analytical methods are described in the respective chapters.

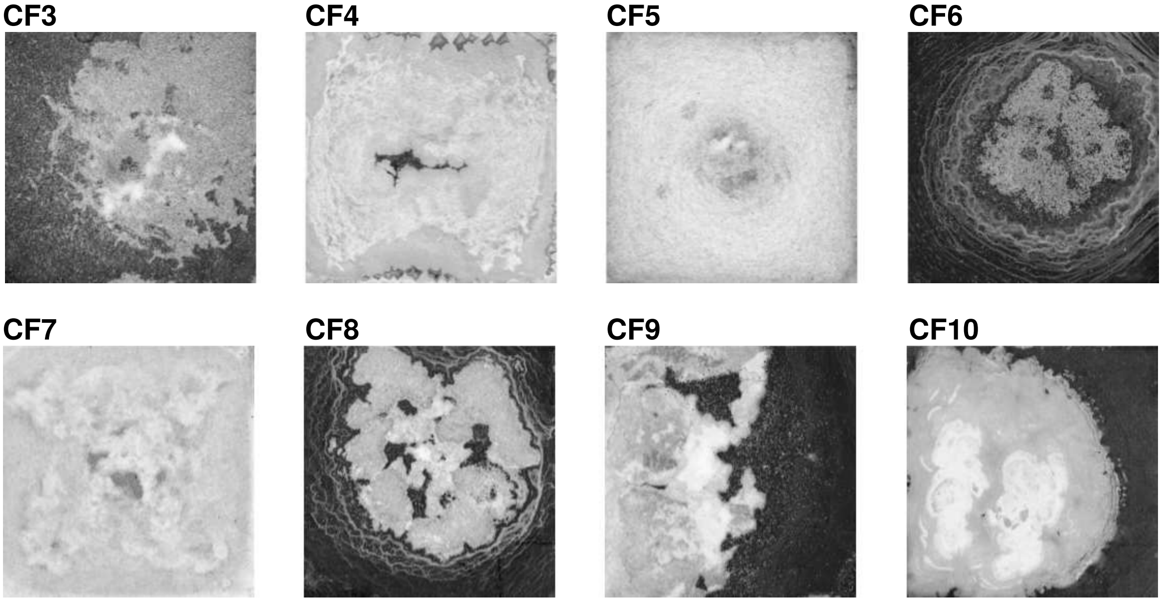

Figure 6.3: Macroscopic photographs of the glass cover slips coated with **CF3**–**CF10**.

CF3 does not form fibrous aggregates, but rather edged rods of crystalline appearance. They consist of smaller arrays, as seen from the inset of the SEM image. These smaller fibrils have diameters of around 0.20 µm, while the larger aggregates have diameters of up to 12 µm. The length of the aggregates varies in the range of approximately 5.0–100 µm, with the median around 30–35 µm. Macroscopically, **CF3** forms irregular coatings on the glass cover slips, with more strongly coated, opaque areas in the center and only very thin and transparent coating towards the outside of the substrate.

The structures generated by **CF4** were very short, and in optical microscope images, resemble the structures generated by **CF3**. SEM images reveal that they consist of very thin and

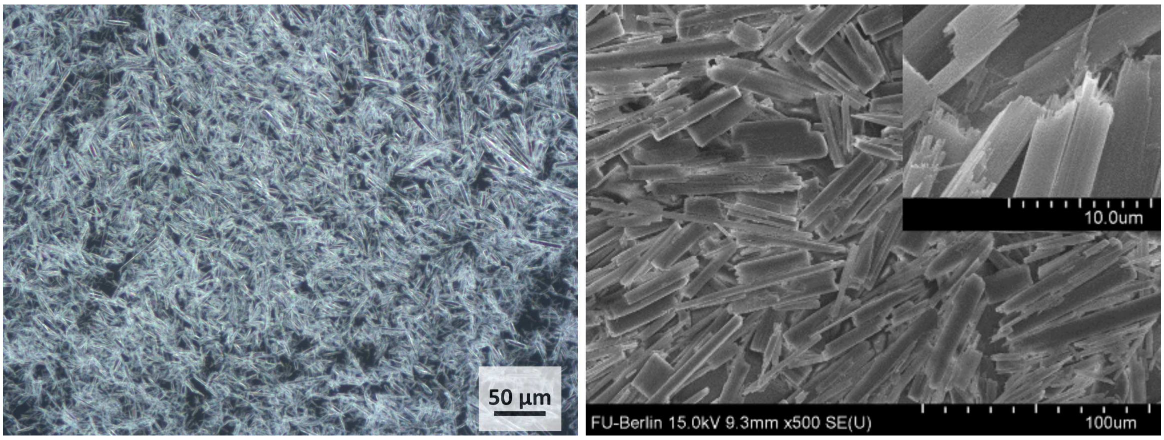

Figure 6.4: The morphology of drop-cast **CF3** on glass; shown are an optical microscope image (20x magnification) and SEM image with the detailed structure in the inset.

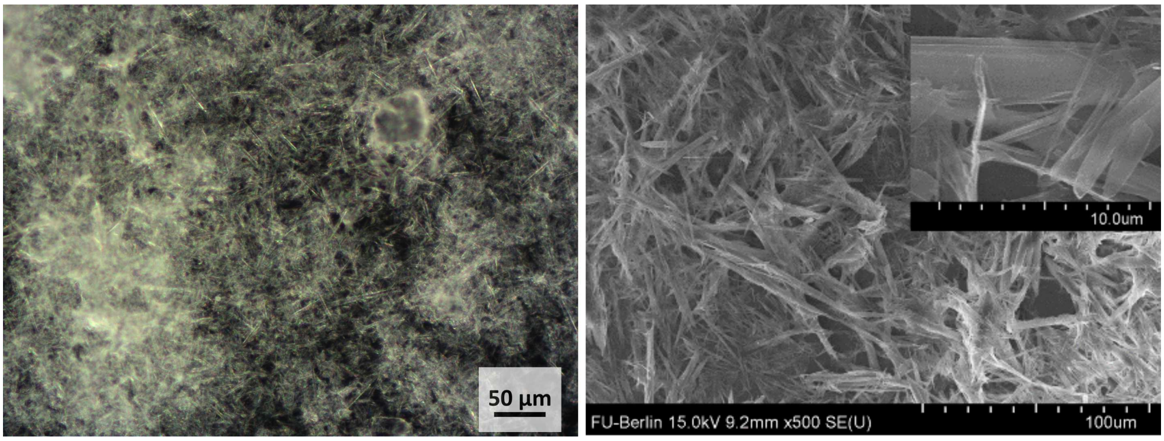

Figure 6.5: The morphology of drop-cast **CF4** on glass; shown are an optical microscope image (20x magnification) and SEM image with the detailed structure in the inset.

flexible aggregates with diameters of 0.10–4.0 µm and lengths of 5.0–110 µm. In between there occasionally exist larger, more rigid rods. Macroscopically, dense and opaque coatings with occasional gaps were formed.

CF5 (like later **CF7**) forms an entangled fibrous network, with no clear starting and end points of the thin structures. The individual filaments have diameters of around 0.20 µm. It forms dense and opaque coatings, comparable with **CF7**.

CF6 forms structures on the surface that appear very crystalline. The individual crystals have a lower aspect ratio than previous ones, with widths of 1.0–26 µm and lengths of 2.3–70 µm. The macroscopic appearance of the coatings is irregular and partially transparent, with denser central areas. Those central areas do not reach the opacity of **CF5** or **CF7**.

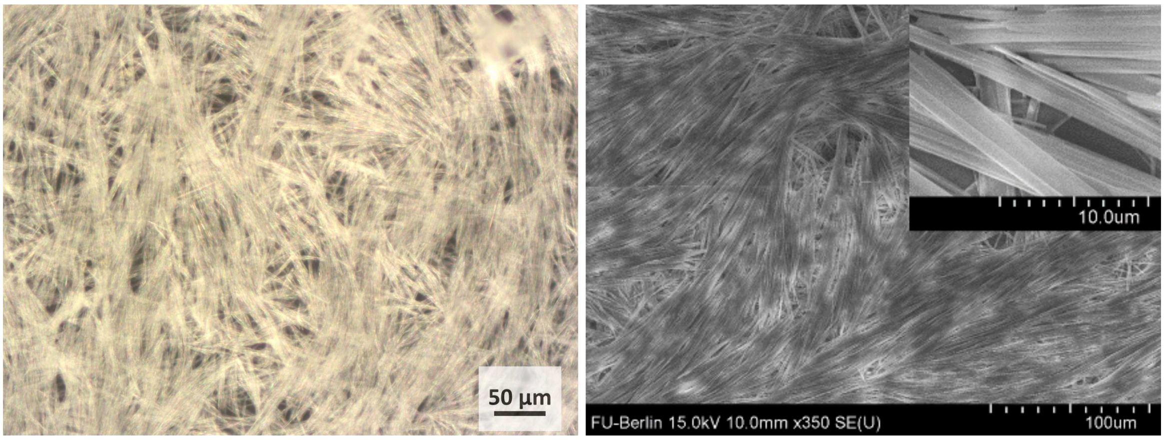

Figure 6.6: The morphology of drop-cast **CF5** on glass; shown are an optical microscope image (20x magnification) and SEM image with the detailed structure in the inset.

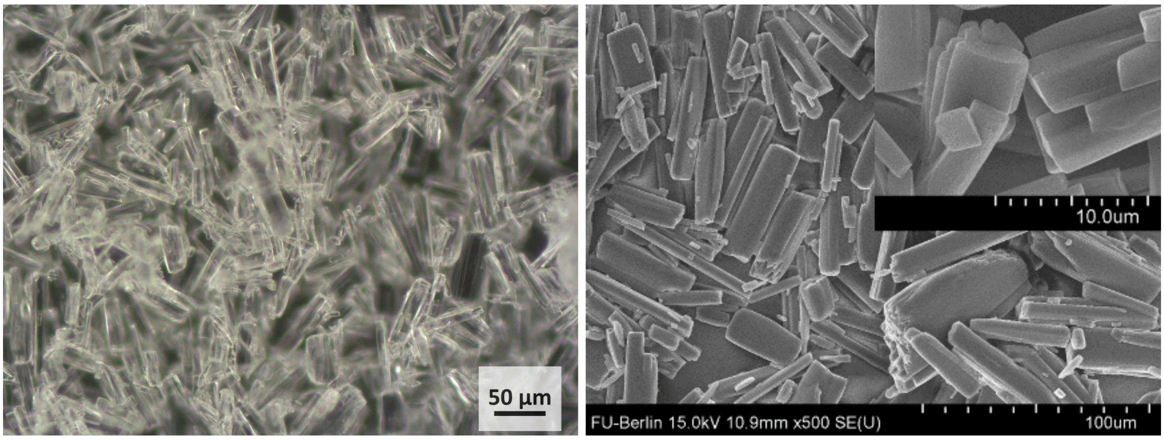

Figure 6.7: The morphology of drop-cast **CF6** on glass; shown are an optical microscope image (20x magnification) and SEM image with the detailed structure in the inset.

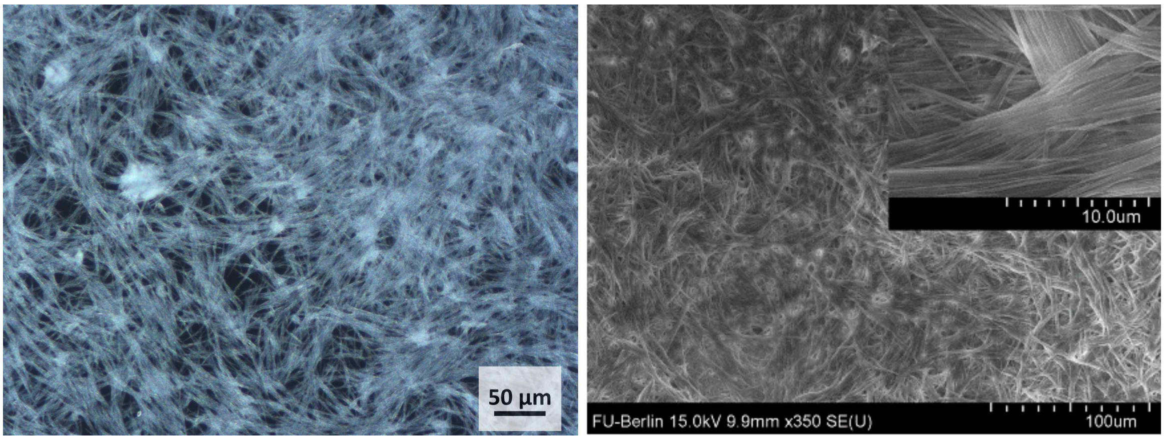

Figure 6.8: The morphology of drop-cast **CF7** on glass; shown are an optical microscope image (20x magnification) and SEM image with the detailed structure in the inset.

CF7 coatings, like **CF5**, consist of very long, flexible filaments of indeterminable length, with diameters of approximately 0.10 µm. Macroscopically, as reported before[7], this compound forms opaque, regular coatings on glass substrates.

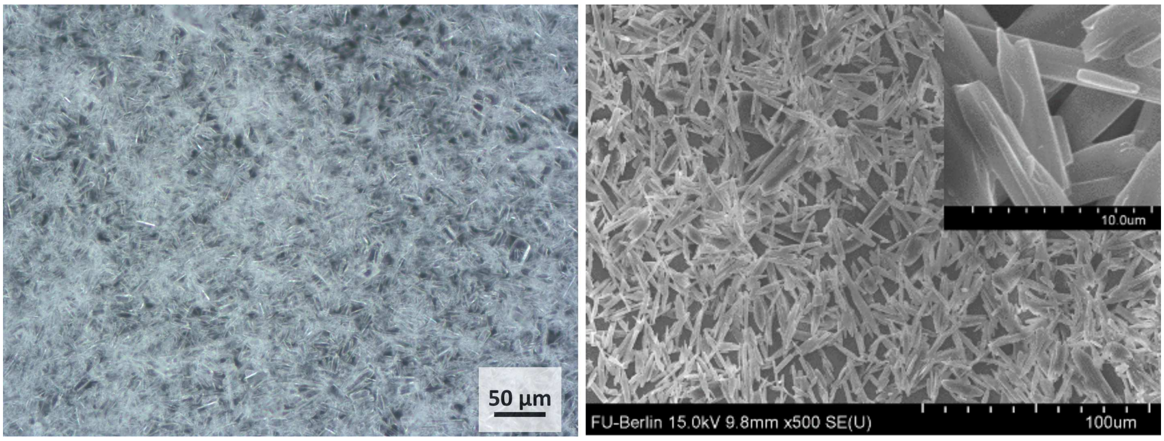

Figure 6.9: The morphology of drop-cast **CF8** on glass; shown are an optical microscope image (20x magnification) and SEM image with the detailed structure in the inset.

Coatings of **CF8** appear very crystalline, as it was the case with **CF6** before, although the individual structures are noticeably smaller. SEM images show widths of 0.40–5.6 µm. The individual structures have tapered ends, as opposed to those of **CF6**, where they terminate at right angles. The coatings were irregular, comparable to **CF6**, but with more opaque dense areas.

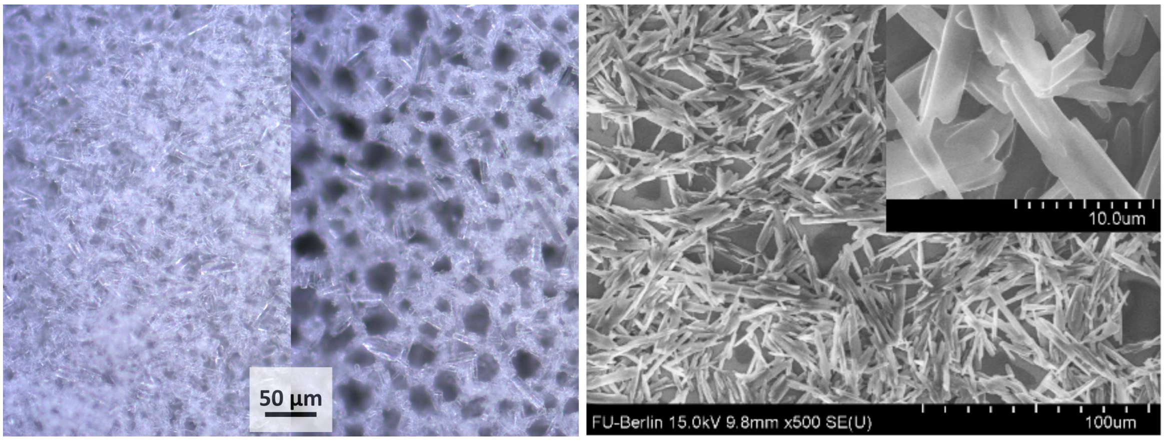

Figure 6.10: The morphology of drop-cast **CF9** on glass; shown are (left) a collage of two optical microscope images (20x magnification) and (right) an SEM image with the detailed structure in the inset.

The surfaces of **CF9** exhibited different morphologies. Depending on the batch, they were either continuous and dense or showed regular gaps. Both morphologies are depicted in Figure 6.10. SEM images reveal a similarity to **CF8**, which is peculiar concerning the difference in properties which will be discussed in the following sections. The explanation is given by SEM images: The individual microscopic aggregates appear fused to each other, creating a continuous network. SEM shows that the individual structures are 6.5−40 µm in length and 1.0−4.5 µm in width. Macroscopically, the coatings were very irregular, showing areas of little to no coating and thick and opaque areas.

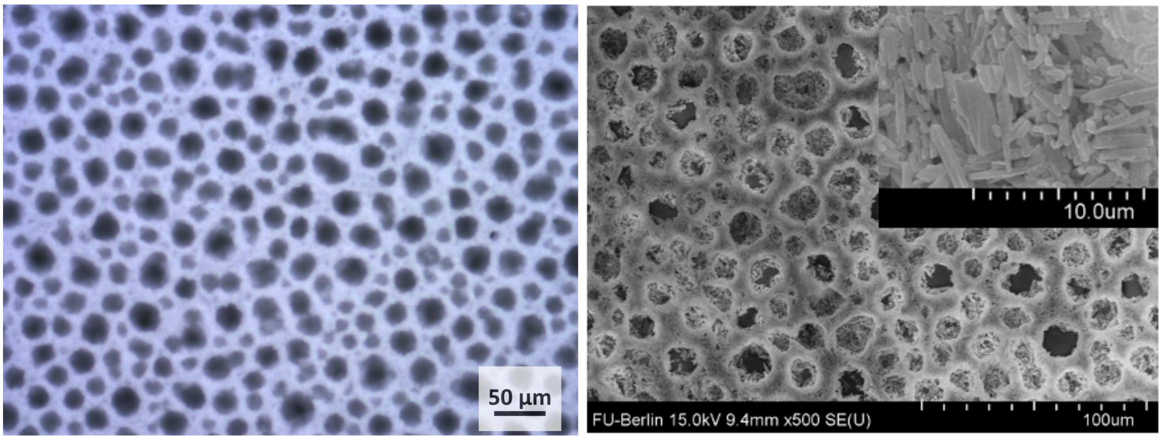

Figure 6.11: The morphology of drop-cast **CF10** on glass; shown are an optical microscope images (20x magnification) of two separate samples and SEM image with the detailed structure in the inset.

Coatings from **CF10** consistently showed a perforated structure. This is already visible in the optical microscope images shown in Figure 6.11. SEM images show that the individual structures were very small, with an average diameter of 0.70 µm and lengths of 0.20−5 µm. Those small aggregates further assembled into superstructures, which resemble two-dimensional pores. It is presumed that this is due to a solvent effect: Because of the long perfluorinated chains, the compound is less soluble in the polar Et_2O. Entropically driven, this leads to islands of solvent during evaporation, which result in round, hollow shapes upon complete evaporation. The macroscopic appearance of the coatings was irregular, with three distinct opacities: Very dense and opaque areas are surrounded by a large area of medium opacity, surrounded by an area of very thin and transparent coating.

For immediate comparison of the surfaces, the previously discussed images of **CF3–CF10** are shown directly next to each other in Figure 6.12 (optical micrographs) and Figure 6.13 (SEM images).

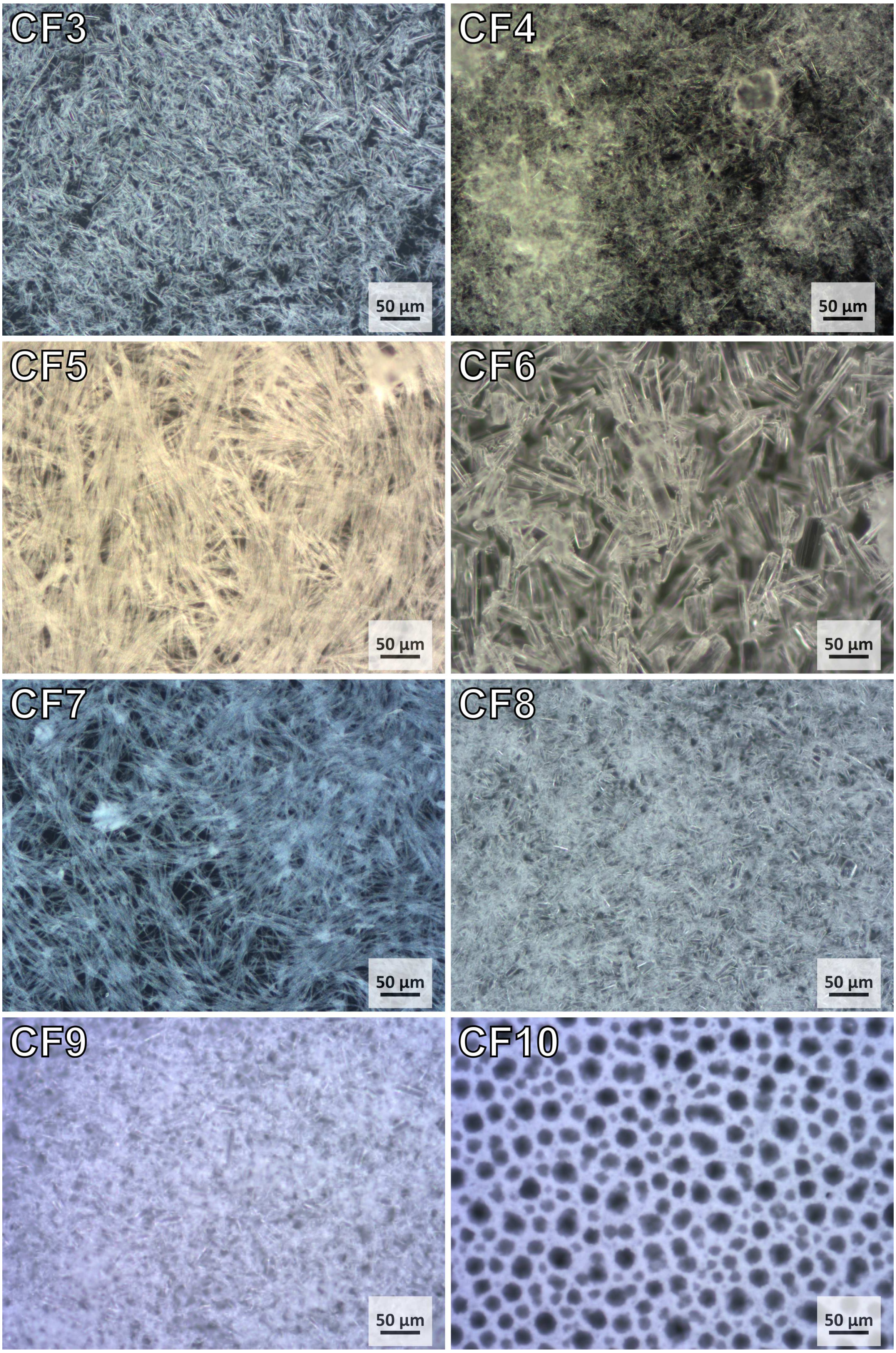

Figure 6.12: Optical microscope images of the coatings created by drop-casting **CF3–CF10**. Images are identical with the optical microscope images in Figures 6.4 to 6.11 and are repeated for better overview.

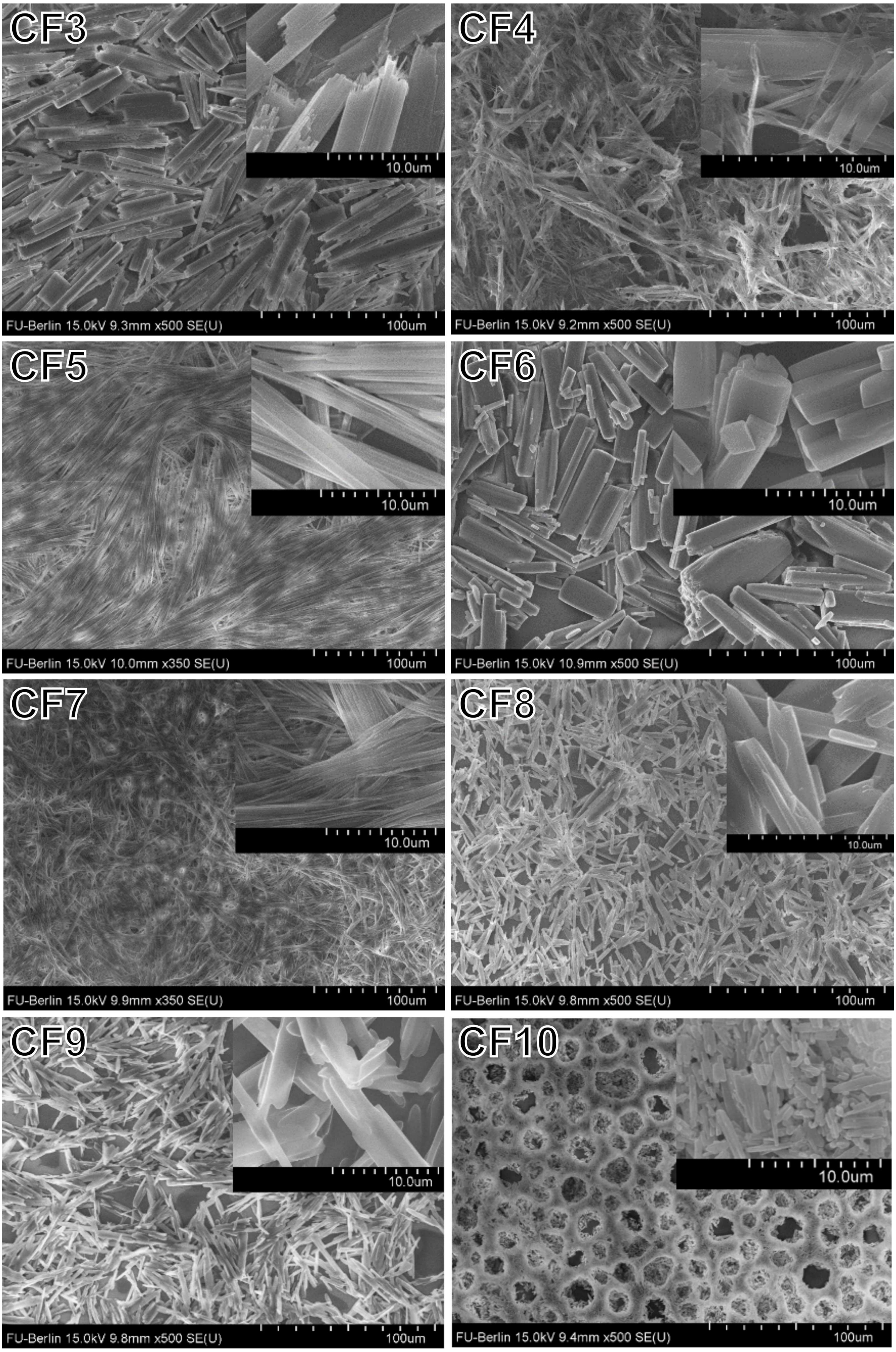

Figure 6.13: SEM images of the coatings created by drop-casting **CF3–CF10**. Images are identical with the SEM images in Figures 6.4 to 6.11 and are repeated for better overview.

Due to the suspected solvent dependence of the pore sizes in **CF10** surfaces, the solvent mixture was varied. Azeotropes containing Et_2O and one other solvent were chosen to avoid changes in solvent composition during the evaporation process. The used mixtures and results are shown in Figure 6.14 and Table 6.2. Expectedly, the solvent mixture influences the pore size. In pure Et_2O, the smallest pores are formed, with a mean area of 72.9 μm^2 and the pores occupying 33 % of the space. When a 60:40 solvent combination of DCM/Et_2O was used, the mean area increased to 422 μm^2. The pore area could be extended to over 1110 μm^2 by utilizing a mixture of Et_2O (98.7 %) and water (1.3 %).

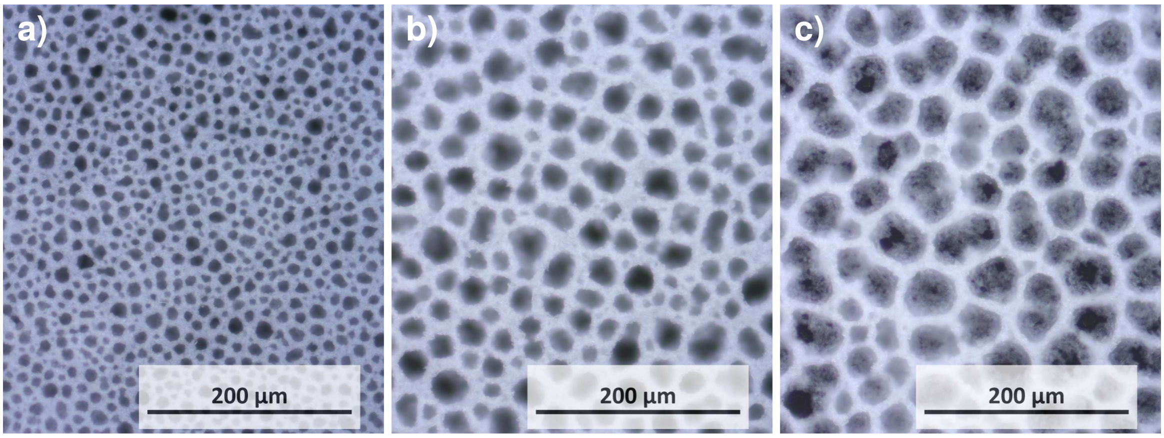

Figure 6.14: Optical microscope images of surfaces coated with **CF10** in different volumetric solvent ratios: (a) Pure Et_2O, (b) DCM/Et_2O 60:40, (c) Et_2O/water 98.7:1.3. The pore size varies depending on the solvent.

Table 6.2: The change in pore sizes of **CF10** upon variation of the solvent mixture.

Solvent mixture	Mean pore surface ± SD / μm^2	Pore ratio
Pure Et_2O	72.9 ± 52.2	33.3 %
DCM/Et_2O 60:40	422 ± 301	42.3 %
Et_2O/H_2O 98.7:1.3	1120 ± 652	42.7 %

6.5 Comparison of Crystallinities

Comparison of the morphologies by optical and scanning electron microscopy showed that the aggregates can differ largely concerning their structures. For example, the coating of **CF6** is very edgy, with thick aggregates of low aspect ratio, while **CF7** forms long, thin, flexible fibers of indeterminable length. These different morphologies indicate differences in crystallinity of the precipitate, which in turn might influence the stability on the surface. To quantify the crystallinity, surface X-ray diffraction (SXRD) measurements were carried out. This technique allows the determination of diffraction patterns of substances on the glass cover slips that were also used for most of the trials.

Similar to XRPD, amorphous materials do not show any any distinct reflections. Microcrystalline materials however show sharp peaks in the diffractogram. Both conditions can be prevalent concurrently. Therefore, for calculation of the crystallinity, the integral of the amorphous portion of the diffractogram was subtracted from the integral of the whole diffractogram. This leaves the integral of the crystalline peaks themselves. The percentage given is their portion of the whole area.

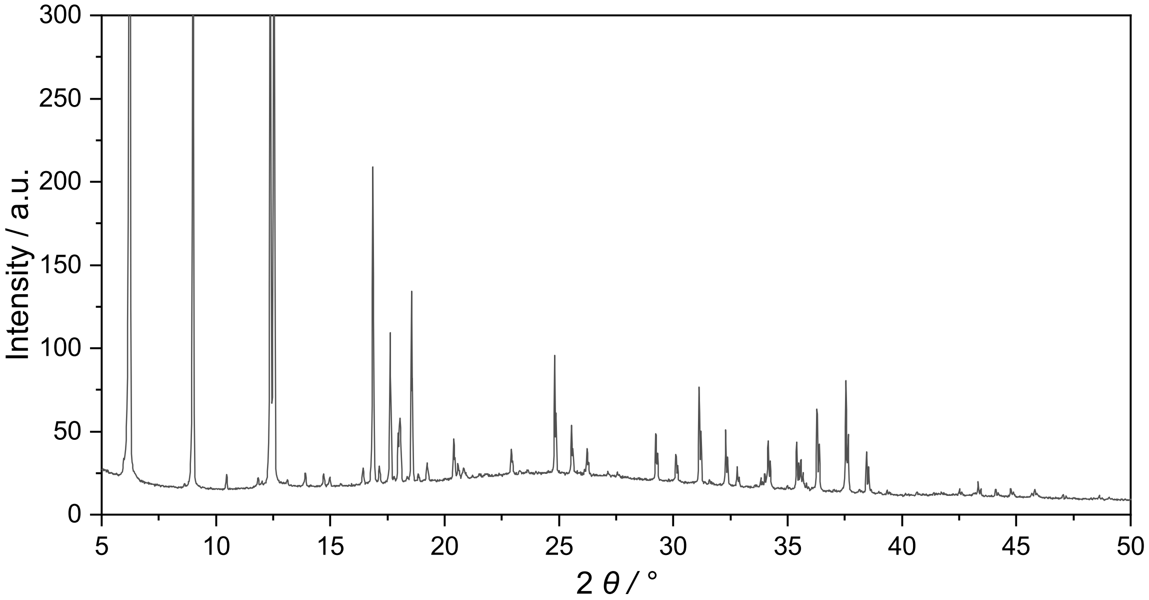

Figure 6.15: X-ray diffractogram of a **CF6** surface. The peak maxima reach as high 1136 a.u.; the scale was shortened for enhanced visibility of the reflections of lower intensity.

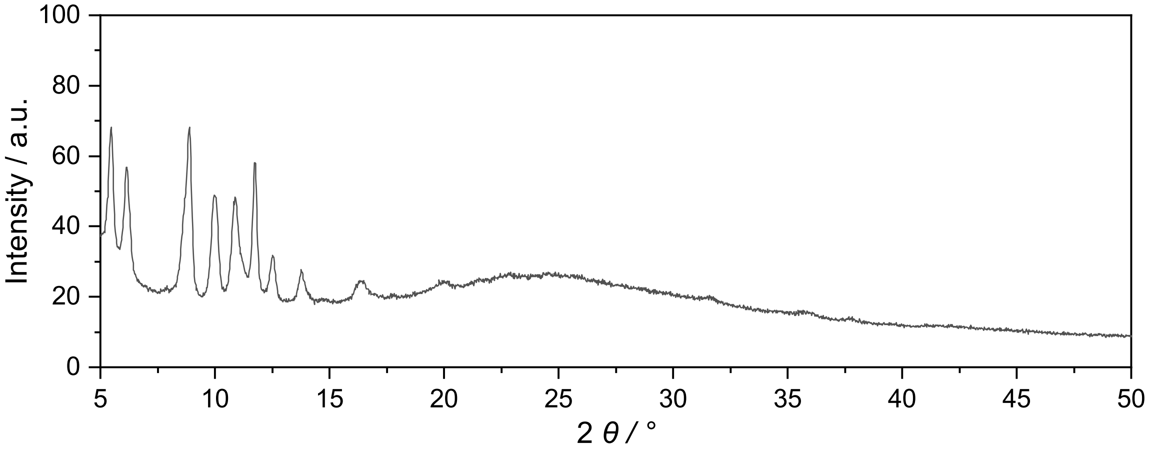

Figure 6.16: X-ray diffractogram of a **CF7** surface. It shows fewer reflections than the **CF6** surface.

Figure 6.15 shows the diffractogram for the sample coated with **CF6**, and Figure 6.16 shows the surface coated with **CF7**. The values for the control surface consisting of cleaned glass substrate are already subtracted. The vertical axes show the reflection intensity in arbitrary units. It can be seen that **CF6** exhibits more and sharper reflections than **CF7**. For the degree of crystallinity, values of 84.3 % for **CF6** and 78.3 % for **CF7** were calculated.

The difference shows that a varying morphology goes along with varying degrees of crystallinity. It is suspected that more flexible (less crystalline) structures exhibit a higher stability on the surface, which will be determined later in this work. For conclusive results a more comprehensive comparison, including the compounds of other chain lengths, has to be conducted.

6.6 Wettability: Static and Dynamic Contact Angles

For comparison of the wettabilities, as a first step, static CAs were measured between the coatings on glass and water droplets. The instrumental details can be found in the experimental section of this work. For better comparability, contact angles were determined on the most opaque area of the surfaces, if possible. Figure 6.17 shows an exemplary droplet profile for each of the surfaces.

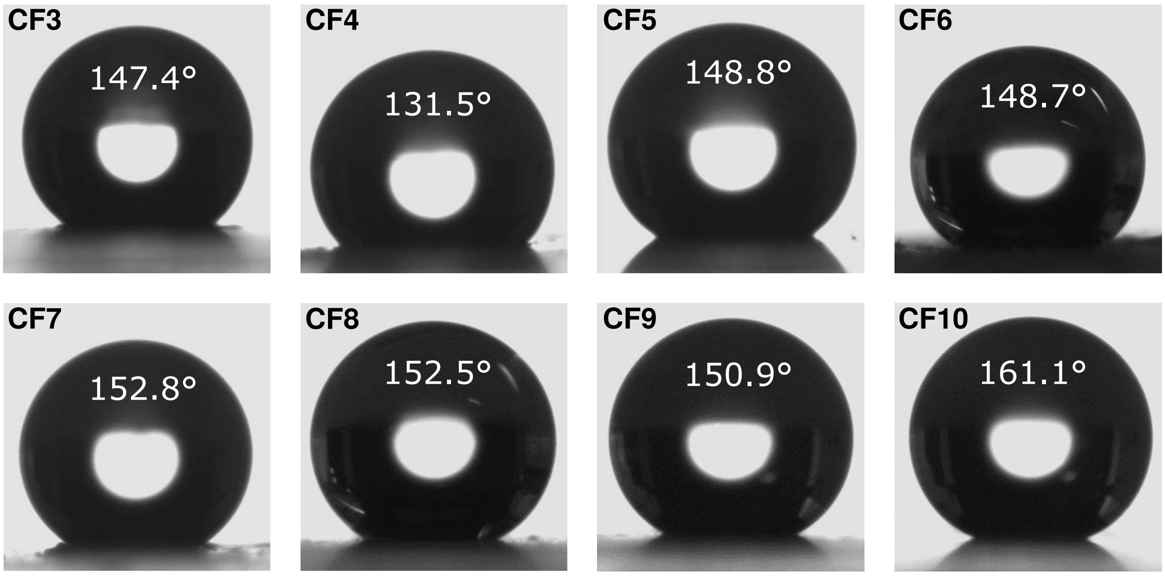

Figure 6.17: Profile pictures of exemplary water droplet shapes on the coated surfaces from which static CA were calculated.

Figure 6.18 shows a diagram with the static water contact angles of the different surfaces. All surfaces show hydrophobicity (CAs above a value of 90°). All surfaces but **CF4** and **CF10** have the threshold for superhydrophobicity (150°, marked by a dotted line) within their

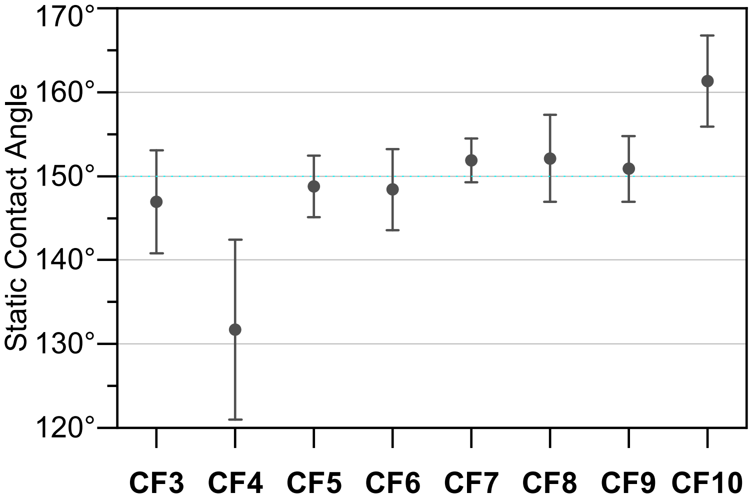

	Static CA / °
CF3	146.9 ± 6.1
CF4	131.7 ± 10.7
CF5	148.8 ± 3.7
CF6	148.4 ± 4.8
CF7	151.9 ± 2.6
CF8	152.1 ± 5.2
CF9	150.9 ± 3.9
CF10	161.3 ± 5.4

Figure 6.18: The diagram shows the static CA for the different surfaces. The dotted line indicates the threshold of superhydrophobicity (150°). The given uncertainty equals the standard deviation. The table shows the plotted values.

standard deviation, with **CF4** being below and **CF10** being consistently above the threshold. Starting from a fluorinated side chain length of seven carbon atoms, namely **CF7**, the mean value is above the threshold for superhydrophobicity.

To differentiate between pinning and non-pinning droplets, the CA alone does not suffice. It has to be substantiated by the contact angle hysteresis (CAH), which is the difference between the dynamic contact angles: advancing contact angle ($\mathrm{CA}_{\mathrm{max}}$) and receding contact angle ($\mathrm{CA}_{\mathrm{min}}$). Alternatively, a tilting angle (TA) can be stated. As the measurement of dynamic CAs is instrumentally more facile, they are preferred over measuring TAs whenever possible. For dynamic CAs, droplets were not fitted by Laplace-Young fitting but rather by ellipse fitting, due to the computational effort of analyzing videos. Therefore, the values can differ from the static CAs. The dynamic CAs of surfaces **CF3–CF10** are plotted in Figure 6.19 and listed in Table 6.3, together with the calculated CAHs. The given uncertainty denotes the standard deviation. The most regular CAHs were measured with **CF7** and **CF10**, as seen by the low standard deviation. **CF7** exhibits the lowest CAH. The CAHs of surfaces **CF4**, **CF6** and **CF8** surpass the 10° mark, with **CF4** exhibiting the strongest pinning with a mean CAHs of more than 20°, also showing the highest variation of values.

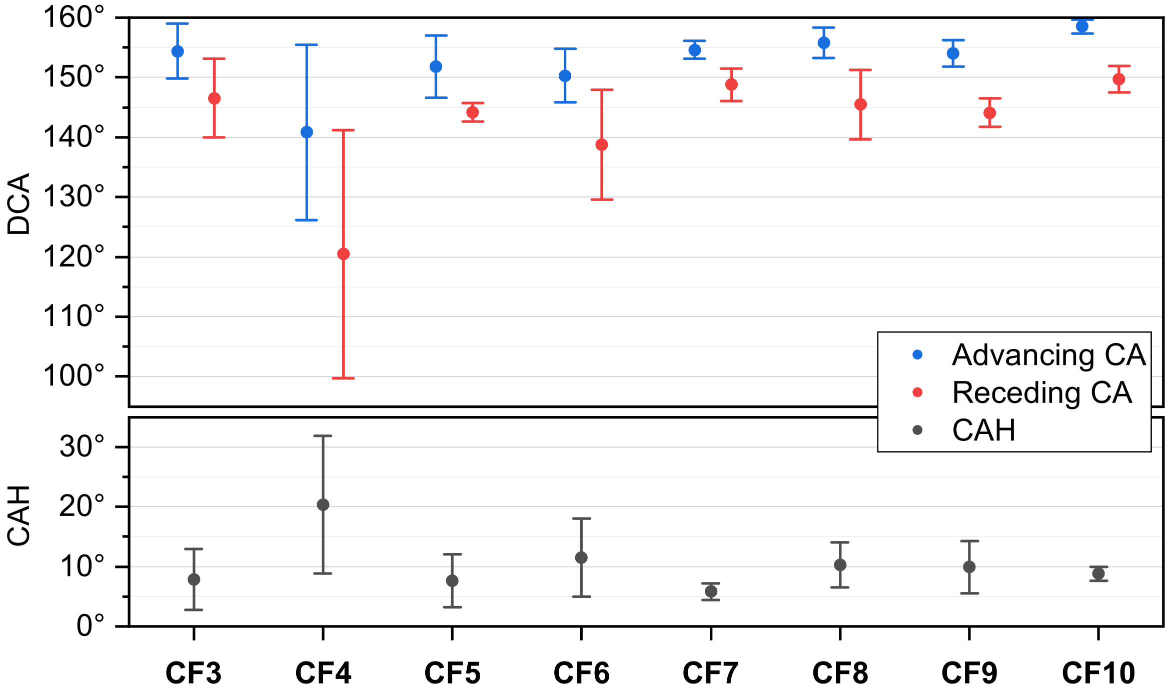

Figure 6.19: Graph of the advancing CAs (blue, left), the receding CAs (red, right) and the contact angle hysteresiscontact angle hystereses (CAHs) (grey). Bars represent the standard deviation.

Table 6.3: Dynamic CA of **CF3–CF10** surfaces. Numbers are degree values. The given uncertainty represents the calculated standard deviation.

Compound	CA_{max}	CA_{min}	CAH
CF3	154.4 ± 3.7	146.5 ± 5.4	7.9 ± 4.2
CF4	140.8 ± 12.0	120.5 ± 16.9	20.3 ± 9.4
CF5	151.8 ± 4.2	144.2 ± 1.2	7.6 ± 3.6
CF6	150.3 ± 3.6	138.8 ± 7.5	11.5 ± 5.3
CF7	154.6 ± 1.2	148.8 ± 2.2	5.8 ± 1.1
CF8	155.8 ± 2.1	145.5 ± 4.7	10.3 ± 3.0
CF9	154.0 ± 1.8	144.1 ± 1.9	9.9 ± 3.6
CF10	158.5 ± 1.0	149.7 ± 1.8	8.8 ± 0.9

6.7 Stability on Glass Surfaces

6.7.1 Static Contact Angle Variation

To compare the stability of the coated surfaces, an apparatus was constructed to allow for consistent and reproducible water output. Four liters of water were channeled through a dripping funnel onto the surface for each flushing cycle. The stability tests were iterated for several rounds to compare the material loss after each flushing cycle. The details are described in the experimental section of this work.

A first indicator of the degradation is the change of the static contact angle on the surface. Water flushing was repeated five times, and static CAs were recorded in between. The given uncertainty represents the standard deviation calculated from nine values per data point, after omitting the highest and lowest value. The results are presented in Figure 6.20 and Table 6.4. In the figure, the color of the dot represents the number of washing cycles, while the position on the horizontal indicates the side chain length. Measured by this standard, it can be seen that **CF3**, **CF6**, and **CF8** are performing poorly in terms of stability. **CF4** exhibits a comparatively low CA, which remains stable. **CF5**, **CF7** and **CF9** exhibit large contact angles even after five rounds of flushing, while **CF10** outperforms the other coatings and remains clearly superhydrophobic throughout five flushing cycles. While **CF6** seems to recuperate from the damage, this can likely be traced back to statistical effects. Although overall nine measurements on three different samples have been taken for each value (details are described in the experimental section of this work), the surface is very irregular and thus can lead to a strong variation of results.

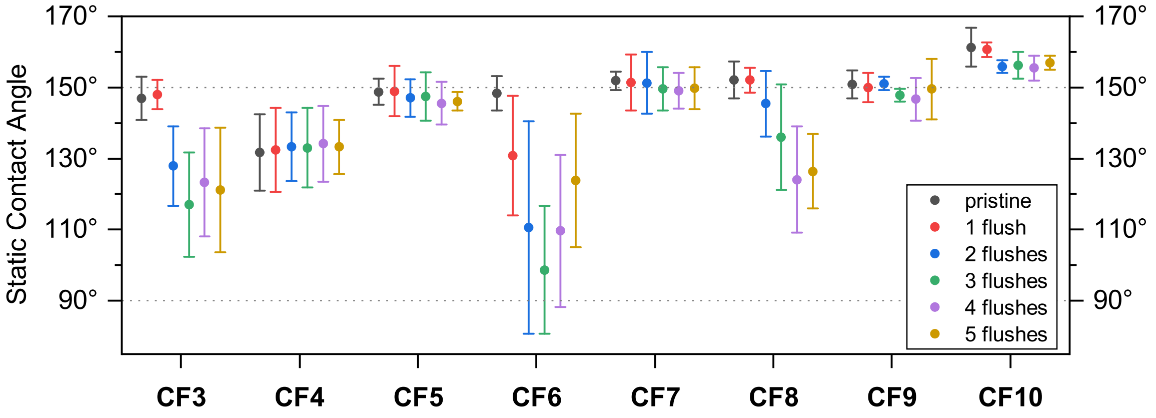

Figure 6.20: Static CAs of coated **CF*n*** surfaces in the process of stability testing via water flushing. The error bars represent the standard deviation. The colors indicate the number of 4 L flushing cycles before measuring the CA.

To rationalize the results about general static CAs and their stability after flushing, it is speculated that even with the more helical structure of perfluorinated chains, there could

Table 6.4: Arithmetic mean values of the static CA of the stability test results shown in Figure 6.20. Numbers are degree values.

Compound	Pristine	1 Flush	2 Flushes	3 Flushes	4 Flushes	5 Flushes
CF3	147.4	147.5	128.0	117.5	123.8	121.8
CF4	131.5	133.3	134.0	133.1	134.0	133.2
CF5	148.8	149.5	146.4	147.8	145.4	145.0
CF6	148.7	124.8	111.0	102.1	110.3	122.0
CF7	152.8	151.9	151.3	149.4	149.0	149.5
CF8	152.5	151.5	141.1	135.2	124.1	127.2
CF9	150.9	150.4	151.1	147.5	146.4	149.6
CF10	161.1	160.2	156.1	156.0	155.4	157.5

be an odd-even effect involved. It appears—if the extreme chain lengths **CF3** and **CF10** are left out of the comparison—that there is a alternation between "good" and "poor" behavior on the surface. **CF4** is less hydrophobic than the other compounds, **CF5** is close to superhydrophobic and stably so, **CF6** is easily washed off, **CF7** is superhydrophobic and remains stable, **CF8** is washed off easily and **CF9** is superhydrophobic and stable.

6.7.2 Dynamic Contact Angle Variation

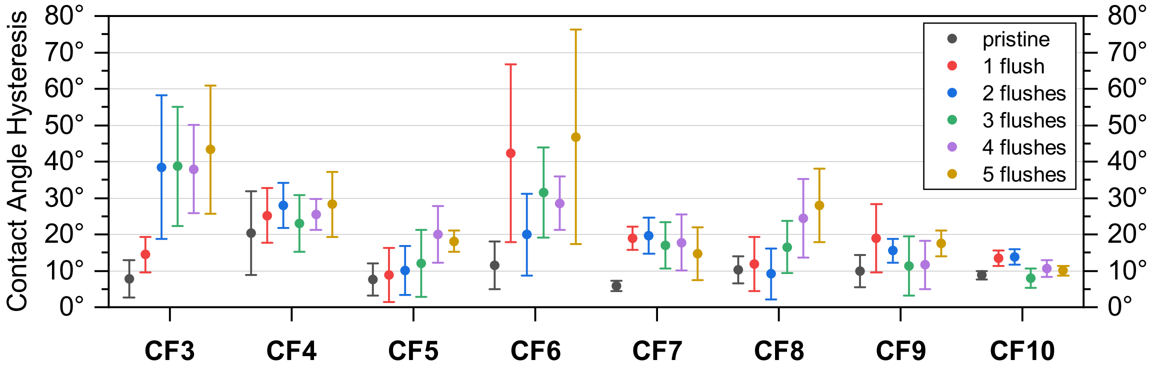

Figure 6.21: CAHs of coated **CF*n*** surfaces in the process of stability testing via water flushing. The error bars represent the standard deviation. The colors indicate the number of 4 L flushing cycles before measuring the dynamic CAs and calculating the hysteresis.

The CAHs from the trials are depicted in Figure 6.21, with their arithmetic mean values presented in Table 6.5. Exemplary, the underlying dynamic CAs after five flushing cycles are shown in Table 6.6 and can be compared with the values on the pristine surface shown prior in Table 6.3. The differences between the surfaces reinforce the same impression as before. **CF3** and **CF6** show the strongest droplet pinning after five flushing cycles, with mean values surpassing 40°. There is a very strong variation in the values, hinting to uneven surfaces. This is also assumed to be the reason that the value decreases again after the second flushing of the **CF6** surface. **CF8** also shows a rise in the CAH, reaching a value of 28°. **CF4** also has a CAH of 28°, although this value is approximately static, beginning from the pristine surface throughout the flushing cycles. Surfaces coated with **CF5**, **CF7** and **CF9** stay under the 20° mark, surpassed again by **CF10**, which even after five flushing cycles shows a CAH of only 10°.

Table 6.5: Arithmetic mean values of the CAH of the stability test results shown in Figure 6.21. Numbers are degree values.

Compound	Pristine	1 Flush	2 Flushes	3 Flushes	4 Flushes	5 Flushes
CF3	7.9	14.5	38.5	38.7	37.9	43.3
CF4	20.3	25.2	28.0	23.0	25.6	28.3
CF5	7.6	8.9	10.1	12.0	20.9	18.1
CF6	11.5	42.3	20.0	31.4	28.6	46.8
CF7	5.8	18.9	19.6	17.0	17.7	14.7
CF8	10.3	11.9	9.2	16.5	24.4	28.0
CF9	9.9	19.0	15.5	11.3	11.7	17.5
CF10	8.8	13.5	13.8	8.0	10.6	10.0

Table 6.6: Mean values of the advancing and receding contact angles resulting in the CAH of the stability test results shown in Figure 6.21. Exemplarily presented is the data after the fifth flushing cycle. Numbers are degree values. The given uncertainty represents the the standard deviation calculated from nine values per data point, after masking each the highest and lowest value.

Flushed surface	CA_{max}	CA_{min}	CAH
CF3	132.7 ± 12.8	89.3 ± 25.7	43.3 ± 14.4
CF4	139.4 ± 7.8	111.1 ± 14.4	28.3 ± 7.3
CF5	153.1 ± 4.6	134.9 ± 2.3	18.1 ± 2.4
CF6	134.2 ± 16.2	87.5 ± 25.9	46.8 ± 24.1
CF7	150.4 ± 5.6	135.6 ± 11.4	14.7 ± 5.9
CF8	126.6 ± 18.8	98.6 ± 25.7	27.9 ± 8.2
CF9	154.3 ± 0.6	136.8 ± 3.0	17.5 ± 2.9
CF10	158.5 ± 0.8	148.5 ± 0.4	10.0 ± 1.1

6.7.3 Gravimetric Determination of Material Loss

As wettability experiments only offer limited insight about the abrasion of the coatings, other analytical methods were applied. To answer the question about the amount of material that was removed from the surfaces, during the washing cycles, a gravimetric determination of the material loss was carried out. The surfaces were weighed before flushing, then after flushing dried under ambient conditions over night and weighed again for each cycle. Figure 6.22

shows the plot of the data presented in Table 6.7. For a better overview, the values will be discussed using the arithmetic mean. The standard deviations are shown in the plot and in the table.

CF3 loses one third of the coating during the first flush and between three and six percent after each additional cycle. **CF4** appears mostly stable; less than ten percent are washed off in the first flush and approximately one percent after each additional round. **CF5** is an exception; the findings are in contrast with the previous studies. It was expected that the surface is stable, as the CAs remained high and the CAHs low throughout the stability test. The opposite was the case, and after losing approximately 30 percent during the initial flushing, further 30 percent were removed during the next four cycles. It is surprising that the water repellency stayed intact with only 40 percent of material left on the surface. It is hypothesized that the coating is washed off layer by layer, with the remaining residue being continuous enough to prevent water droplets from penetrating the surface. The remaining surfaces behave more expectedly. **CF6** is the least stable, losing almost half of the material during the initial flush and ten percent more during the next cycles. **CF7** is comparatively stable and loses less than 15 percent during all five cycles. In this case the comparatively large standard deviation should be noted, as the surfaces behaved more variably compared to the other "stable" surfaces (**CF4**, **CF9** and **CF10**). **CF8** is unstable and loses half the material during the five flushing cycles. **CF9** is stable, losing only a mean of ten percent of material and shows a low standard deviation compared to **CF7**. Surfaces cast from **CF10** again outperform the other surfaces, as they show a mere five percent of material loss with the smallest deviation in the trial series.

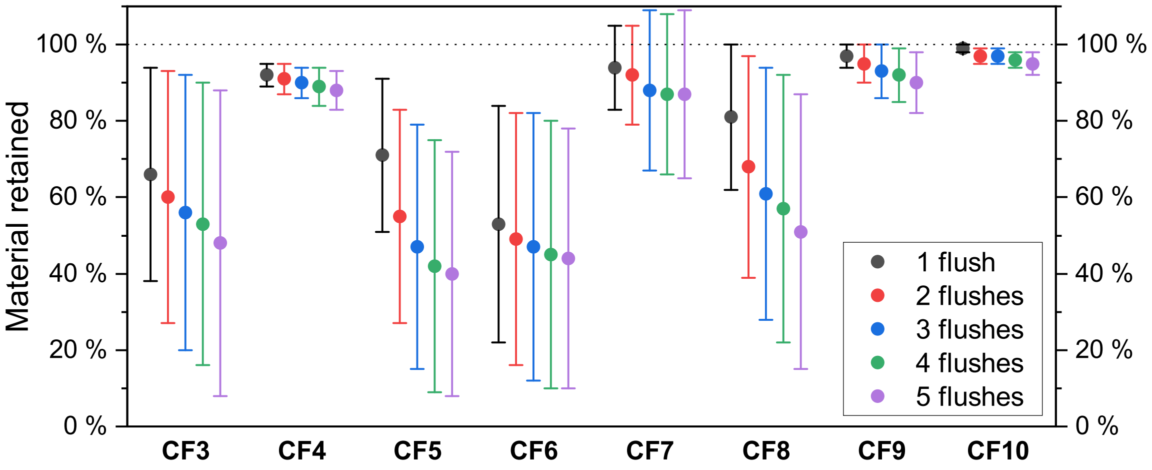

Figure 6.22: Remaining material during stability testing **CF3–CF10**, when weighed in between the flushing cycles, normalized to a starting value of 100 %.

Table 6.7: Numerical values of the graph shown in Figure 6.22. The given uncertainties are the standard deviations resulting from three measurements on three different surfaces per value.

Compound	1 Flush	2 Flushes	3 Flushes	4 Flushes	5 Flushes
CF3	66 ± 28 %	60 ± 33 %	56 ± 36 %	53 ± 37 %	48 ± 40 %
CF4	92 ± 3 %	91 ± 4 %	90 ± 4 %	89 ± 5 %	88 ± 5 %
CF5	71 ± 20 %	55 ± 28 %	47 ± 32 %	42 ± 33 %	40 ± 32 %
CF6	53 ± 31 %	49 ± 33 %	47 ± 35 %	45 ± 35 %	44 ± 34 %
CF7	94 ± 11 %	92 ± 13 %	88 ± 21 %	87 ± 21 %	87 ± 22 %
CF8	81 ± 19 %	68 ± 29 %	61 ± 33 %	57 ± 35 %	51 ± 36 %
CF9	97 ± 3 %	95 ± 5 %	93 ± 7 %	92 ± 7 %	90 ± 8 %
CF10	99 ± 1 %	97 ± 2 %	97 ± 2 %	96 ± 2 %	95 ± 3 %

6.7.4 Digital Quantification of Morphology Changes

When subjected to water flushing, not only the CAs and the weight of the surfaces changed, but also the macroscopic appearance of the coated surfaces. Thicker coatings were white and opaque, and turned more transparent upon removal of substance. Also, in some cases, different areas of coated surface were covered with changing amounts of substance. To quantify these changes on a surface, and to estimate relative coating thicknesses, a new method was devised: Photographs were taken of the surfaces under consistent conditions and computationally evaluated. The details are described in Chapter 4.3. This method, coined morphology evolution analysis (MEA), outputs histograms showing the brightness of the pixels on the horizontal axis and the number of the pixels on the vertical axis. Because of the relationship between surface thickness and opacity, this can be used to estimate surface thicknesses. One exemplary surface has been analyzed for each on the compounds, on a pristine surface and after one to five flushing cycles, respectively. The analyses will be discussed in order of side chain length.

The surface with **CF3**, shown in Figure 6.23, has two obviously distinct but broad areas of different brightness in its pristine state, which are marked with letters in the graph. A brighter peak at a value of 162 (b) and a darker area at brightness 88 (c) can be spotted instantly and mark areas of two different thicknesses. In the center of the photograph, a small but distinct brighter area can be seen, which corresponds to a small shoulder (a) on the right end of the histogram. When flushed once, the bright areas (a) and (b) are almost completely removed and add to area (c). This peak grows sharper and higher during the next flushing cycle, as brighter pixels and presumably thicker areas become thinner, but do not fall further below in brightness than peak (c). During the third flush, the area is shifted further to the left. During the fourth flush, no obvious change occurs, which is in line with the gravimetric data. The fifth flush again thins the surface and results in peak (d) at a brightness value of 75.

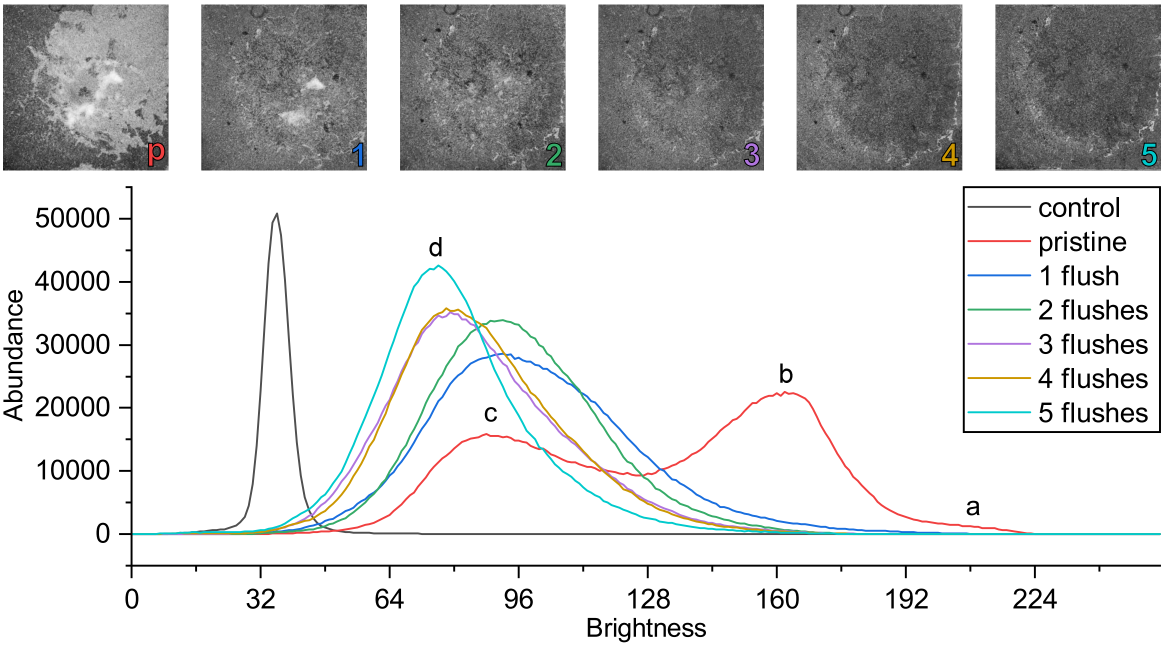

Figure 6.23: MEA showing the abundance of differently bright pixels of a picture of a **CF3** coated surface, indicating different thicknesses.

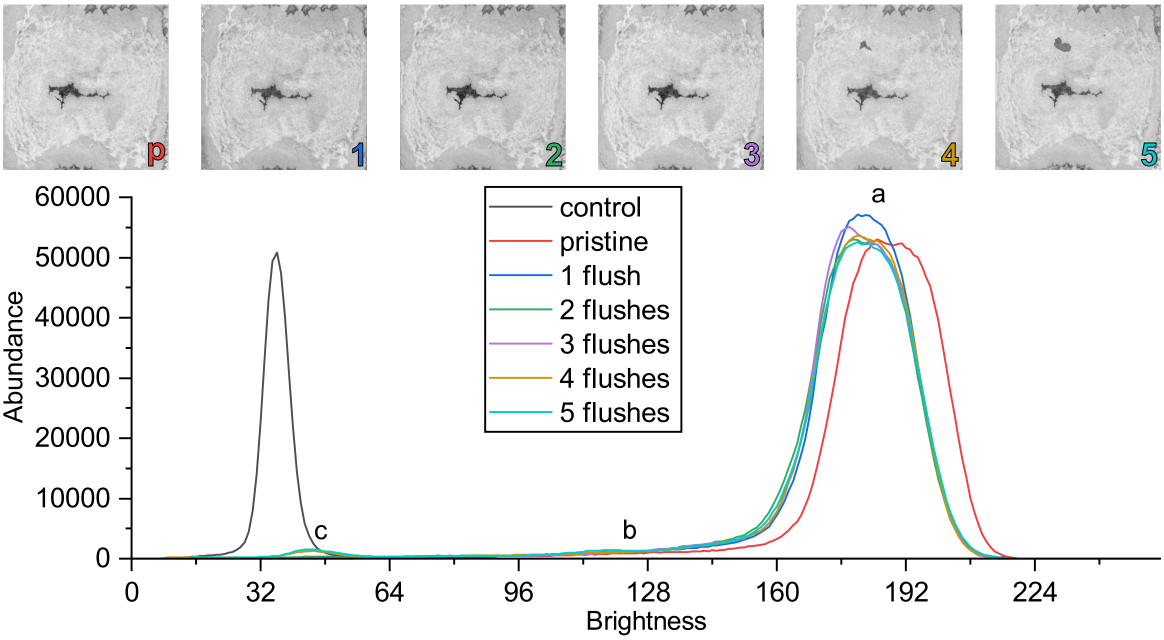

Figure 6.24: MEA showing the abundance of differently bright pixels of a picture of a **CF4** coated surface, representing different thicknesses.

The MEA of **CF4** shows a different situation, depicted in Figure 6.24. The photographs result in one very distinct peak (a) at a value of 188 and one small shoulder (b) at a value of around 120, which corresponds to the only thinly coated gap in the middle of the coating. On the first flush, the maximum is shifted slightly to the left and becomes sharper, which presumably corresponds to an only slightly thinner coating of more regular thickness. Peak (a) then lessens slightly in abundance during the next flushing cycles as the material only gets marginally thinner. This was corroborated by the gravimetric measurements. Very small areas were removed from the surface almost completely, resulting in the emergence of a small peak (c) close to the glass reference value.

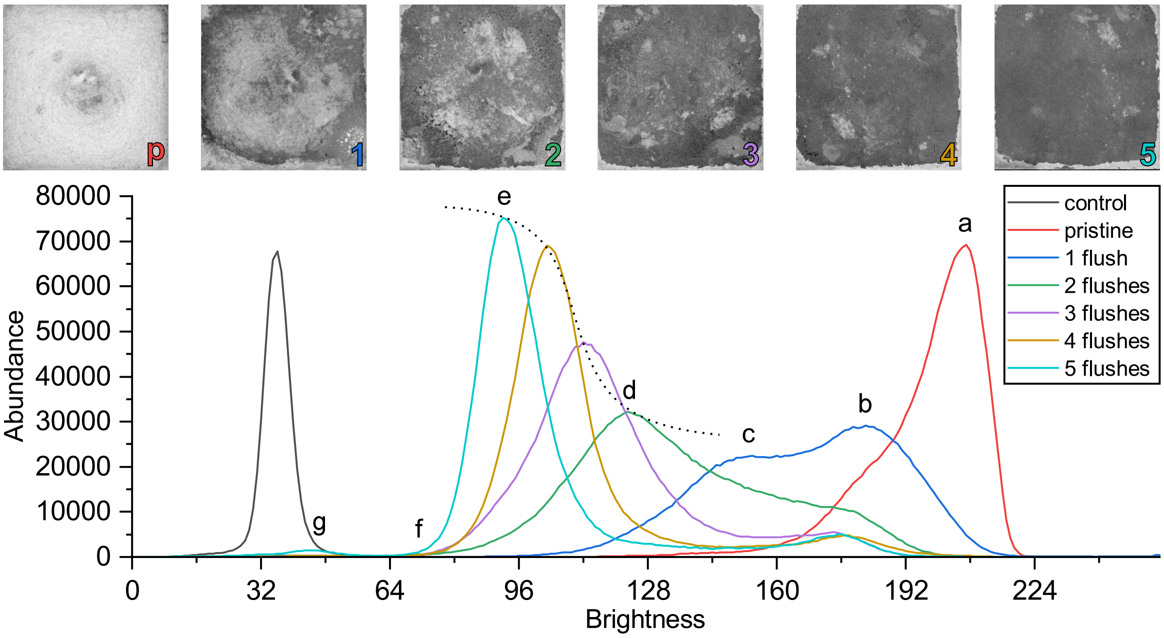

Figure 6.25: MEA showing the abundance of differently bright pixels of a picture of a **CF5** coated surface, representing different thicknesses. The dotted line guides the eye through the asymptotic change of a peak through flushing cycles 2–5.

The MEA of **CF5**, shown in Figure 6.25, depicts a more complex situation. The pristine surface shows an asymmetric peak (a) at brightness 206, with a steep slope at its right hand side and a more gradual decline on its left hand side. The asymmetry can indicate that at this brightness the maximum value is reached at which the thicknesses can be differentiated. After the first water flush, peak (a) disappears to give rise to lower thicknesses with a peak (b) at brightness 182 and a shoulder (c) at a value of 152. The second flush again shifts the peak to a point of lower brightness and corresponding thickness (d) at a value of 122, and a shoulder to the right hand side. The remaining three flushing cycles gradually lead to a sharpening of the peak and shifting to the dark end. Two features of these curves become apparent. If the peak values are connected as represented by the dotted curve to guide the eye, it appears as if peak (e) at brightness 92 is towards the end of an asymptotic rise into the direction of lower brightness. This and the fact that the leftmost ends of the peaks of flushing cycles two to five coincide at approximately the same value (f) indicate that there might be a maximum amount of substance that can be washed off by this stability testing method. This corroborates with the gradually decreasing differences in the gravimetric measurements. Only small parts of the surface are removed completely, giving rise to peak (g) close to the glass reference peak. This was seen with surfaces of the compound **CF4** before.

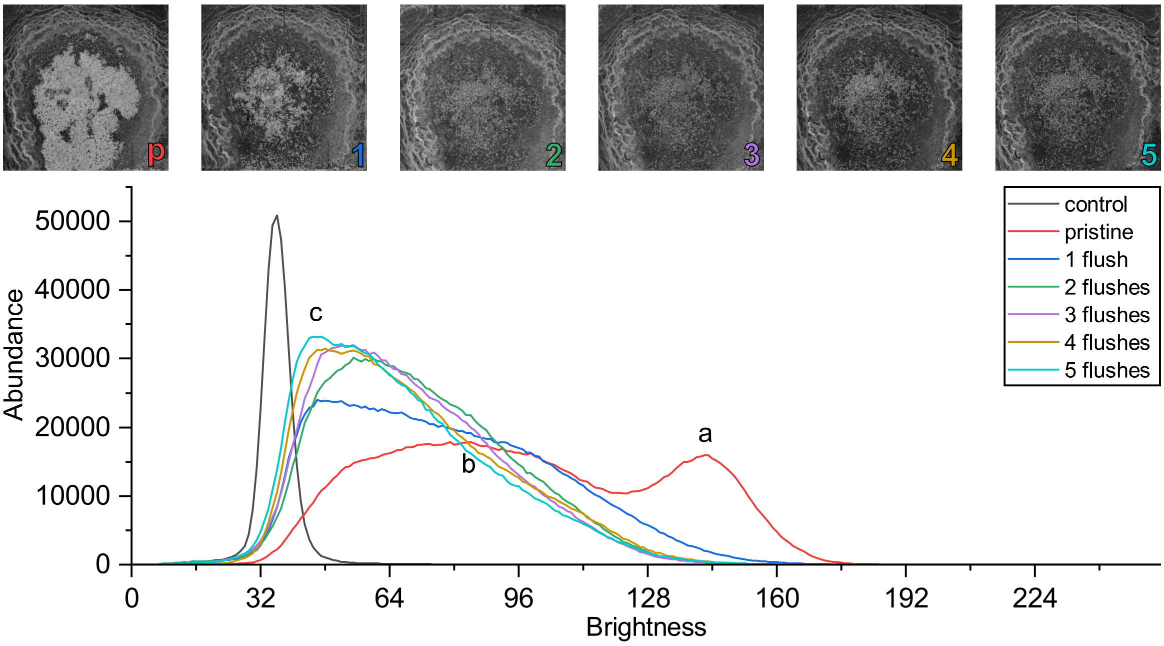

Figure 6.26: MEA showing the abundance of differently bright pixels of a picture of a **CF6** coated surface, representing different thicknesses.

The analysis of the **CF6** surface (Figure 6.26) in its pristine state shows a distinct peak (a) at a brightness of 142 and a very broad peak starting at its left hand slope and reaching to the far dark end of the histogram. It should be noted that the peak heights are very low with pixel numbers under 2×10^4, compared to the previous analyses which showed peak heights of about $5–7 \times 10^4$. Only **CF3** surfaces showed similarly low peaks. This indicates a broad distribution of the thicknesses, as the overall number of pixels that are analyzed is constant. The jagged nature of the coating is also visible in the peak shapes, as they are not as smooth in comparison, but rugged. After the first flush, peak (a) disappears and the broad peak (b) shifts towards the dark end, resulting in peak (c), with a broad asymmetric slope at its right hand side. The asymmetric peak shape might in this case indicate the dark end of the reliable spectrum, as it was seen in **CF5** with the bright end. Further flushing raises peak (c) and flattens the right hand slope, but results in very little change, as corroborated by the gravimetric analysis.

The MEA of **CF7** (Figure 6.27) shows a very narrow peak at brightness 191. Compared to the shape of the glass reference peak it might indicate a very uniform coating, as the aspect ratio

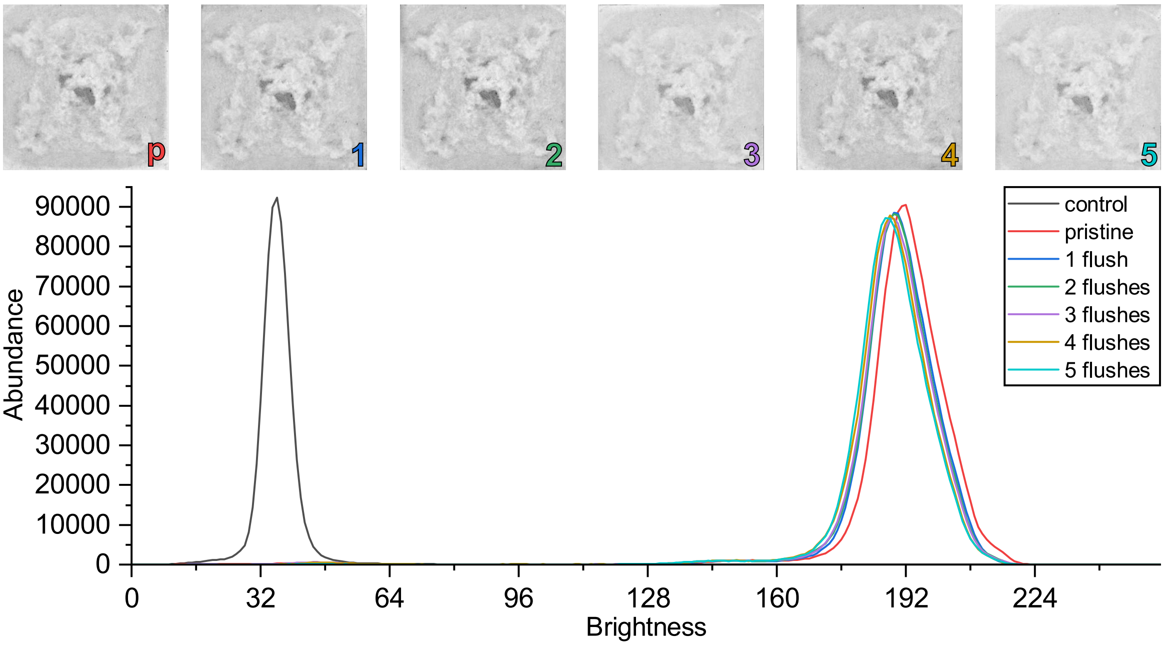

Figure 6.27: MEA showing the abundance of differently bright pixels of a picture of a **CF7** coated surface, representing different thicknesses.

comes close to the uncoated case. It should be noted that the peak is at the very bright end of the histogram and might therefore not reliably take into account thicknesses that surpass the barrier, from which the coating does not become more opaque and might therefore be not a reliable rendering of the real situation. Although the peak shape is symmetrical, and the peak is at lower brightness than the asymmetric peak of **CF5**, which is presumably at the bright end of the measurable spectrum. The peak has a very low shoulder between values 120–160, this shows the less densely coated areas of the not completely homogenous surface. Flushing does not change the appearance of either peak or surface greatly, the peak shifts to marginally lower brightness values but largely remains similar. This again is corroborated by gravimetric analyses.

The histogram for **CF8**, seen in Figure 6.28, illustrates the irregular nature of the coatings that the photographs show. There are two large peaks, peak (a) at the bright end at a value of 159 and peak (c) at the dark end of the spectrum. Between those two peaks, there is an area of horizontal curve shape, indicating approximately equal distribution of all brightness values in between. The rugged curve shape again is an indicator for the uneven coating. After the first flush, peak (a) shifts towards the dark end and becomes lower in abundance. Notably, also peak (c) is reduced in abundance. The area between the peaks grows more abundant, indicating an equalizing distribution of coating material across the surface. During the next flush cycles, this results in peak (b) at a brightness value of 89. This translates to the picture, as it can be seen that the black and white areas equalize to a more general gray color. This histogram, which largely indicates a redistribution of coating, is difficult

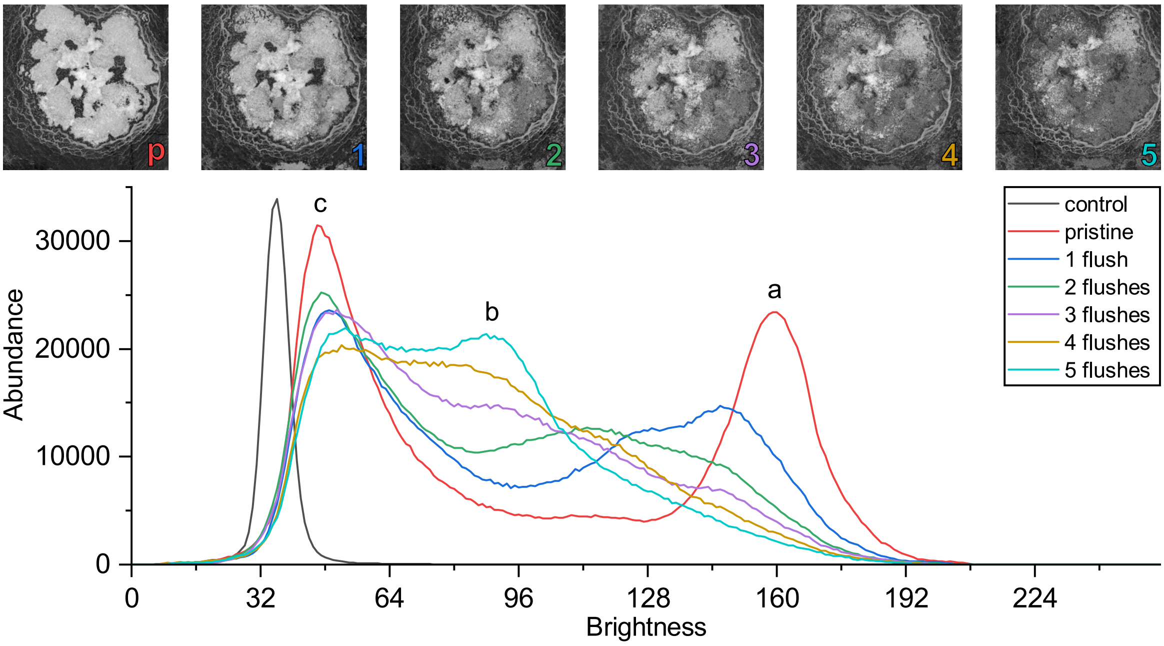

Figure 6.28: MEA showing the abundance of differently bright pixels of a picture of a **CF8** coated surface, representing different thicknesses.

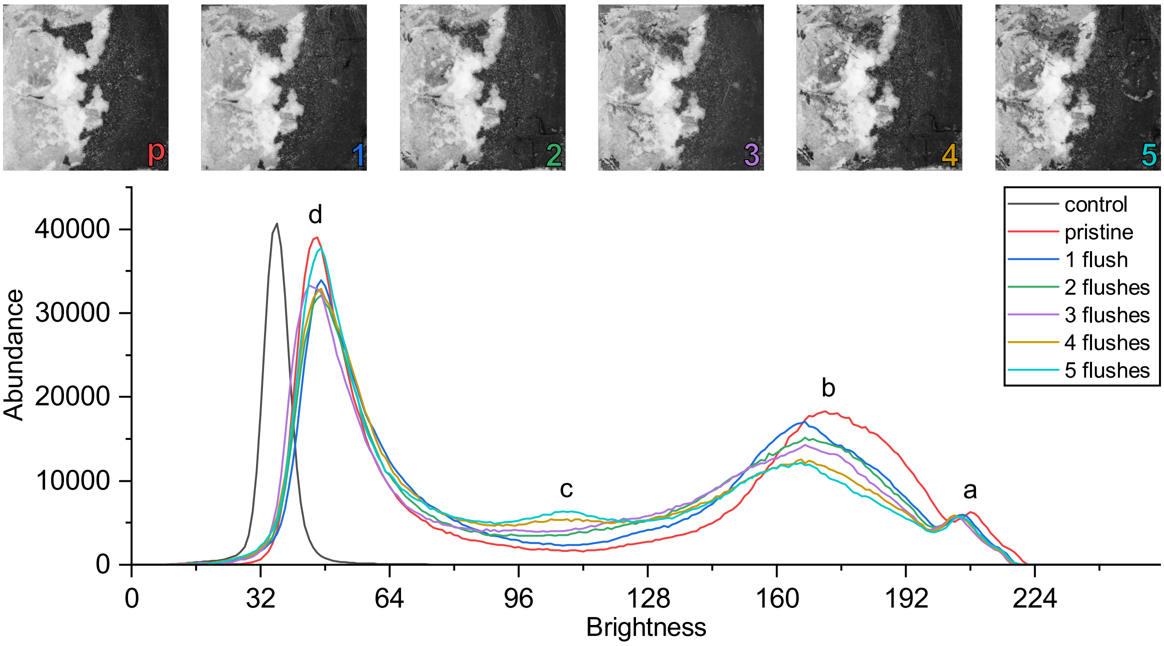

Figure 6.29: MEA showing the abundance of differently bright pixels of a picture of a **CF9** coated surface, representing different thicknesses.

to set in relation to the gravimetric measurements, which show a steady decline in coating weight. The removed material presumably corresponds to the decline in brighter areas in brightnesses above 110.

The MEA of **CF9** shows peak (a) with low abundance at a brightness of 208, directly below that peak (b) at 173 and towards the glass reference peak a high abundance of dark pixels (d) at a brightness value of 45. Upon flushing, the bright peaks (a) and (b) shift only slightly towards the dark end and peak (b) lowers in abundance. At the same time, a new peak (c) emerges at brightness 108, while initially peak (d) lowers in abundance. It is reminiscent of the redistribution phenomenon of the **CF8** surface. It can be seen in the left hand side of the photograph that the dark area as well as the bright area smoothen at their borders and become more gray, indicating a equalization of the thicknesses. Peak (d) interestingly recuperates towards the last flushing cycle, this phenomenon can not be explained.

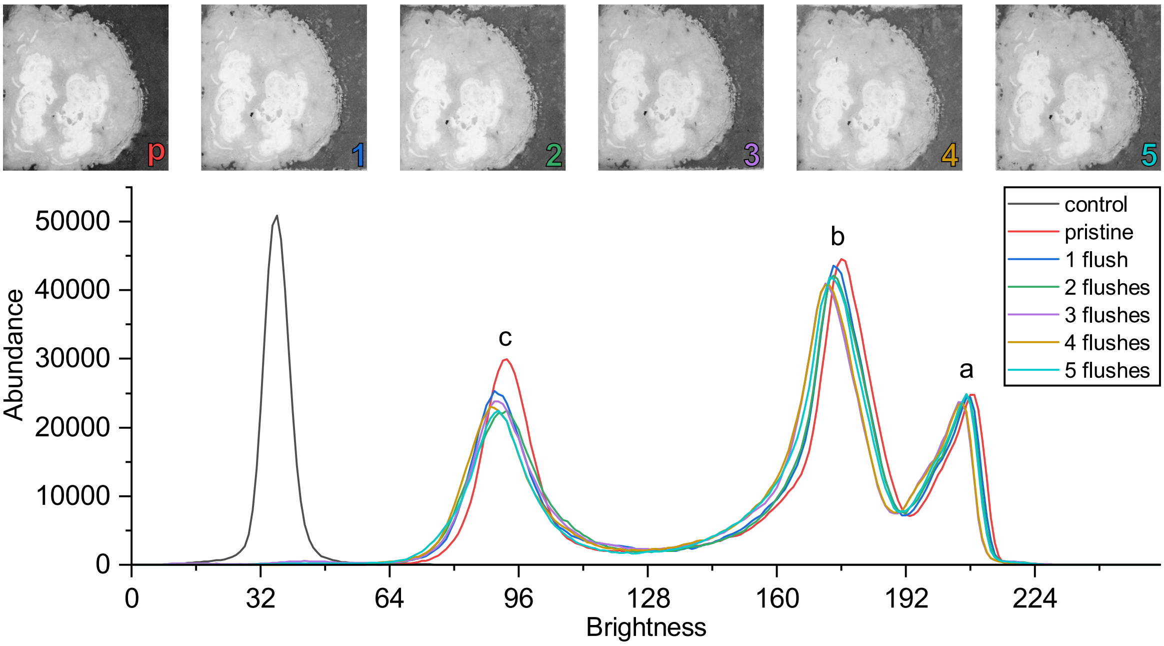

Figure 6.30: MEA showing the abundance of differently bright pixels of a picture of a **CF10** coated surface, representing different thicknesses.

The MEA of **CF10** (Figure 6.30) shows three distinct peaks at brightness values of 208 (a), 176 (b) and 93 (c). Peak (a) is asymmetric, presumably indicating the end of the reliable spectrum towards the bright end. All peaks shift only marginally in brightness during flushing. In abundance, they change differently. The brightest peak (a) lessens the least, peak (b) slightly more noticeably and peak (c) towards the dark end of the histogram most notably. This change is the largest during the first flush, as can be corroborated by the gravimetric measurements. From the photographs it can be seen that the dark area becomes more gray. This histogram interestingly suggests that this surface is more stable in the densely coated areas, while the coating in the lightly coated areas is washed away more easily. On the other hand, it might be an indicator showing the limitations of the technique, as a non-linear absorption of light might be a cause as well.

Overall, the results from this new method proved to be insightful. While the received values have to be evaluated carefully and may not refer linearly to the thicknesses of the coatings, they shed more light onto the abrasion behavior of each surface.

6.8 Lubricant Infusion

In the work of Q. Wei and C. Schlaich it was shown that due to the fibrous nature of the **CF7** surfaces, they can be used to entrap a lubricant on the surface. The hydrophobic lubricant Fluorinert® FC-70 (perfluoropentylamine) was used. By itself, it easily washes off a glass surface; when infused into the xerogel scaffold, it stays on the surface and enhances the hydrophobic properties.

For infusing trials, surfaces made with **CF7**, **CF9** and **CF10** were chosen because of their proven stability and hydrophobicity on the surface. **CF5** was also added to the list for its stable hydrophobicity, even though it did not perform well in gravimetric measurements. As an example for compounds with lower stability on the surface, **CF8** was added to the test line.

During contact angle measurements, lubricant climbs up a droplet due to capillary forces and makes a reliable contact angle measurement impossible. Therefore, in the case of lubricated surfaces, tilting angles, were used as a method of comparison. The pristine surfaces were measured as well for comparison of the TAs and the results are shown in Table 6.8. Results prior to stability testing were promising: TAs after lubrication were notably smaller than before. In the case of **CF5** and **CF7**, the tilting angles were reduced to two thirds of the original value. In the case of **CF8**, the value was more than halved. For **CF9** and **CF10**, the tilting angles of the infused surfaces were lower than one fifth of the value of the dry coatings. In the case of the infused **CF10**, the TA was as low as 2.2°.

Table 6.8: Tilting angles measured on pristine coating and coating infused with lubricant Fluorinert FC-70 before and after flushing once with the stability testing apparatus. Numbers are degree values.

	CF5	**CF7**	**CF8**	**CF9**	**CF10**
Pristine coating	20.2	18.6	14.6	20.2	12.3
Lubricant infused	14.0	12.0	5.9	3.7	2.2
Infused, flushed	>90	>90	>90	49.2	>90

Upon stability testing however, the coating and lubricant were removed from the surface together. This is in contrast to previous results, where a high stability of the lubricated **CF7** surface against water flow was reported. In this series, on all surfaces but **CF9**, this led to a pinning of the droplet, which would not roll off even with the glass surface in completely vertical position (90°). In the case of **CF9**, some damaged coating remained on the surface and the TA was 49°, which is far above a hydrophobic value.

Therefore, the results from literature[7] could neither be reproduced nor extended onto the surfaces produced with compounds of other side chain lengths. The lubricant acted as a solubilizing/desorption agent, which was removed by the mechanical force of water and aided the removal of the coatings. This might be due to a stronger force of the water stream used in this work when compared to the tap water stream from literature and corroborates the need for repeatable testing.

6.9 Anisotropic Wettability by Spin-Coating

During trials to use spin-coating for thinner layers **CF7**, a serendipitous discovery was made. When trying to achieve thinner coatings via spin-coating instead of drop-casting, the structures aligned preferentially from the center of the rotation outwards. This leads to anisotropic roughness: Orthogonal to the fiber direction, the roughness is higher than along the fiber direction. This is illustrated schematically in Figure 6.32 (b). Because CAs depend on the roughness of a surface, it was assumed that this might lead to anisotropic wettability as well.

Glass surfaces spin-coated with 5 mg mL^{-1} solutions of **CF7** in diethyl ether at a rotation speed of 10 000 min^{-1} proved too thin. When attempting to perform CA measurements on these surfaces, the droplet penetrated through the coating and spread over large areas of the surface. Therefore, first a basis of **CF7** was drop-cast (0.5–0.6 mL, 5 mg mL^{-1}) before spin-coating an upper layer for anisotropic structure. This was done at 10 000 min^{-1} from 25 mg mL^{-1} gelated solution in diethyl ether. Either three or five drops were cast upon the surface which was already in rotation. It was limited to small amounts, because the spin-coating process re-dissolved the **CF7** coating at the position of drop impact.

Figure 6.31 shows optical microscopic and SEM images of the surface created by spin-coating five drops and accompanying orientation analyses as used in Chapter 5. The SEM image was taken between the center and the left edge of the coating. It can be seen that the anisotropy created is visually not very prominent, although the orientation analysis reveals a preferential orientation from the center outwards.

As these CA measurements need a connotation about the angle at which the droplet was captured, the following semantics were used: “Orthogonal” denotes a line of view orthogonal to the created structures, *i.e.*, orthogonal to the hypothetical line between the coating center

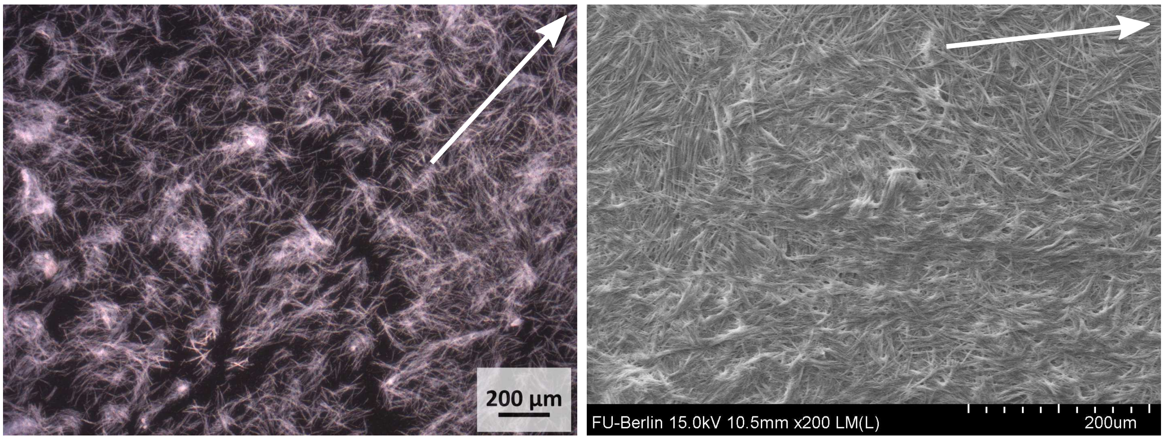

Figure 6.31: Optical microscopic and SEM image of a surface pre-coated by drop-casting 5 mg mL^{-1} **CF7** in Et$_2$O onto a round glass surface and spin-coating with 25 mg mL^{-1} solution at 10 000 min^{-1}. The optical microscope image was taken with the center of the plate in the upper right, the SEM image with the center to the right of the captured image. The white arrows illustrate the calculated predominant orientation and point roughly towards the direction of the center.

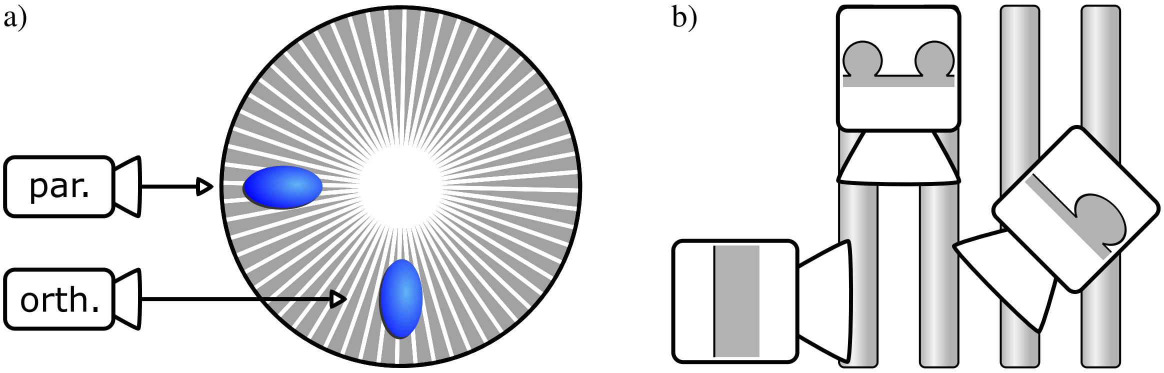

Figure 6.32: (a) Description of orthogonal and parallel viewing angles while measuring CAs on substrate spin-coated with **CF7**. The distortion of the droplets is exaggerated to illustrate the effect of anisotropic CAs. (b) Illustration of different roughnesses in different directions. The insets show the situation from three hypothetical viewpoints in the same z-level as the coating.

and the edge. “Parallel” denotes a line of view directly towards the center. This terminology is visually represented in Figure 6.32.

Five droplets were measured per surface, each individual droplet was measured from both viewing angles. Results are presented in Figure 6.33; the number next to the data points states the arithmetic mean value and standard deviation. Additionally, for each individual droplet, the difference between its parallel and orthogonal contact angle was calculated. These differences were positive without exception. For the surface created by using three drops while spin-coating, the mean difference was (4.8 ± 1.1)°, while for the surface created with five drops, the mean difference was (10.8 ± 4.9)°. The individual measurements are presented in Table 6.9

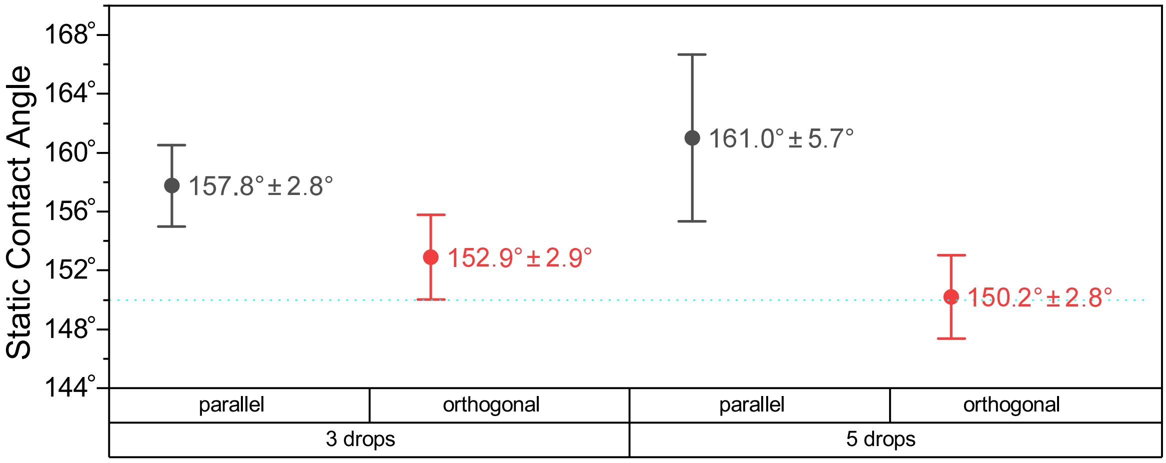

Figure 6.33: CAs on glass substrate coated by drop-casting and then spin-coating with varying amounts of **CF7**. Data points represent the mean value of five measurements each, the bars represent the standard deviation. It can be seen that into two directions the CAs differ depending on the amount of spin-coated substance.

Table 6.9: CAs on glass substrate coated by drop-casting and then spin-coating with varying amounts of **CF7**. Numbers represent degree values. Each water droplet was measured in two alignments. At a viewing angle parallel to the surface structure the contact angle was without exception larger, by varying degrees. In the bottom line the mean values and standard deviation are given.

	3 Drops ‖	3 Drops ⊥	3 Drops, Δ	5 Drops, ‖	5 Drops, ⊥	3 Drops, Δ
Droplet 1	154.1	149.6	4.5	160.7	150.0	10.7
Droplet 2	160.3	156.7	3.6	157.5	146.8	10.7
Droplet 3	155.7	150.5	5.2	153.7	150.5	3.2
Droplet 4	158.5	154.1	4.4	165.9	149.1	16.8
Droplet 5	160.2	153.7	6.5	167.2	154.6	12.6
Mean ± SD	157.8 ± 2.8	152.9 ± 2.9	4.8 ± 1.1	161.0 ± 5.7	150.2 ± 2.8	10.8 ± 4.9

Half the CA differences were reached as reported for rice leaves[138]. The clear trend shows that spin-coating can be used to create anisotropic wettability, if the hydrophobicity is created by fibrous coatings. Scaling this technique up might prove difficult due to the limiting setup, yet this insight can be used when utilizing other anisotropic coating methods with this compound class: For example coating the surface while creating a flux of the solution into one defined direction, by placing the substrate at an angle.

Table 6.10: Summary of the stability testing trials. Intervals are determined arbitrarily by subjectively evaluating trends of the data. Desirable properties are marked in green.

		CF3	**CF4**	**CF5**	**CF6**	**CF7**	**CF8**	**CF9**	**CF10**
Static CA	Initial[a]	h	l	h	h	h	h	h	h+
	Change[b]	h	l	l	h	l	h	l	l
	Variation[c]	h	m	l	h	l	h	l	l
CAH	Initial[d]	l	h	l	h	l	h	l	l
	Change[e]	h	l	h	h	l	h	l	l-
	Variation[f]	h	m	l	h	m	m	l	l
Weight	Change[g]	h	l	h	h	l	h	l	l
	Variation[h]	h	l	h	h	h	h	l	l

[a] high: 150° within SD range, high+: entire SD > 150° [b] low: difference <5° after 5 flushes
[c] medium: <20°, low: <10° after 5 flushes [d] low: <10° [e] low: <12°, low-: <2° after 5 flushes
[f] medium: <10°, low: <5° after 5 flushes [g] low: >85 % retained material after 5 flushes
[h] low: <10 % SD after 5 flushes.

6.10 Chapter Summary: The Role of the Fluorinated Side Chain Length

The length of the perfluorinated side chain plays a crucial role in the morphology of the created surfaces. These changes in morphology translate into different characteristics on the surface. This strongly affects the stability. The examples are condensed into Table 6.10. The results are grouped subjectively into different intervals; desired characteristics are marked green, meaning high contact angles, low contact angle hystereses and low abrasion. A small variation of the results is also desired for reliable behavior. While certainly the margins of the intervals used for grouping are set arbitrarily, they convey two implications. One is that the desired behavior increases at longer chain lengths. The second implication is that there seems to be an odd-even effect involved in terms of stability. Chain lengths with an even number of carbon atoms tend to form shorter aggregates with less entangling on the surface and therefore less stability.

There are exceptions to this. **CF3** seems very crystalline, even though it has an odd number of fluorinated carbon atoms. **CF4** creates very stable coatings, even without forming elongated fibers, although the surfaces are less hydrophobic than the others. The most notable exception is **CF10**: Following the trend, it should have created unstable coatings of lower hydrophobicity, but the opposite was the case. The small aggregates created superstructures of porous appearance on the surface, which surprisingly were very stable against water flow. The hydrophobicity and stability exceeded all other surfaces in this comparison.

Therefore an odd-even effect can only be suspected for the stability of surfaces **CF5–CF9**. **CF6** and **CF8** behaved very poorly in almost every aspect of the comparison. After stability testing, the hydrophobicity and retained material both decreased fundamentally. The measurements showed high variation, which, together with visual evaluation, showed the irregularity of the surfaces. On the other hand, **CF5** and **CF7** created very regular surfaces and, together with **CF9**, showed high contact angles, low contact angle hystereses and (with the exception of **CF5**) low abrasion with water.

7 Conclusion

This work addressed the fabrication of supramolecular materials as surface coatings. Two computational methods were used to enhance the analysis of microscopic and macroscopic images. For determining the ordered orientation of materials, the plug-in OrientationJ for ImageJ was used. A macro was scripted to allow for facile comparison of the order of aggregated structures from microscope images. For comparison of the thicknesses of surfaces, the thickness-dependent opacity of white **CF*n*** coatings was utilized. Photographs were taken of surfaces under standardized conditions, and a Python-based script[120] was used to quantify the different brightnesses on the surface. This allows for inferences about the surface thickness when other methods are unsuitable.

With the purpose of achieving anisotropy while drop-casting supramolecular surfaces, a TESLA coil was built. This technology had only be used recently for the ordering of CNTs and the method was coined teslaphoresis.[6] In this work, CNT trials were reproduced. The limitations of transferring the technology onto other materials are explored by utilizing it with a variety of supramolecular aggregators. The scope of the technique could successfully be extended upon an NDI derivative. Aggregates formed by compound **NDI-C8** are either of spherical or needle-like shape, and both are significantly influenced by the electric field of the TC, creating ordered aggregates on the centimeter scale.

Building on previous work[7], the use of compounds **CF*n*** for the fabrication of superhydrophobic surfaces was further investigated. Perfluorinated side chains of different lengths were used and their impact on the morphology of drop-cast aggregates was evaluated. For examination of the stability on the surfaces, an apparatus for repeatable and reproducable flushing with water was devised and the surfaces exhibited to several rounds of abrasion by water. Compound **CF10** with the longest perfluorinated chains showed the highest stability and the most desirable properties, as elaborated in the respective chapter summary.

Anisotropic wettability was achieved by preparing a layer of drop-cast **CF7** and spin-coating a layer with centrosymmetrically oriented **CF7** fibers on top. An angle-dependent difference in contact angles of over 10° could be obtained.

8 Experimental Section

8.1 General Methods

Reagents purchased from ABCR, Acros Organics, Alfa Aesar, Apollo Scientific, Fluorochem, Sigma Aldrich/Merck, TCI and VWR were used without further purification unless noted otherwise. Anhydrous solvents were either obtained from a MBRAUN MB-SPS-800 solvent system or from aforementioned sources. Deuterated solvents were purchased from Eurisotop. Ultrapure water was acquired from a Milli-Q® Reference Water Purification System.

The carbon nanotubes used are single-walled CNTs ordered from Sigma-Aldrich/Merck (chirality (6,5), carbon >90 %, carbon as SWNT >77 %, diameter 0.7–0.9 nm).

Reactions sensitive to water and/or air were carried out with Schlenk line techniques under argon (ALPHAGAZ 1 Ar, 99.999 % purity) or nitrogen (ALPHAGAZ 1 N2, 99.999 %.

Thin-layer chromatography (TLC) was performed on aluminum sheets coated with silica gel 60/F254 (Merck) or ALOX N/UV254 (Macherey-Nagel). Column chromatography was performed on silica gel 60 (40–60 nm, 230–400 mesh, Merck) or ALOX I, neutral (50–200 µm, Acros Organics).

^{1}H NMR, ^{13}C NMR, ^{19}F NMR and corresponding 2D NMR were recorded with instruments by Bruker (ECX 400, AV 500 and AVIII 700) or JEOL (ECX 400, ECP 500 and ECA 600). Chemical shifts are reported in ppm, and are referenced to residual non-deuterated solvent peaks in relation to the signal of tetramethylsilane. Coupling constants (J) are given in Hz. Multiplicities are denoted as follows: singlet (s), doublet (d), triplet (t), quartet (q), a subscript "br" indicates a broadened peak.

Electrospray ionization time-of-flight high resolution mass spectrometry (ESI-TOF-HRMS) was conducted with an Agilent 6210 ESI-TOF spectrometer.

Optical micrographs were recorded with a Zeiss AxioScope A1 microscope and an attached Axiocam 105 color camera using Zeiss ZEN core software. Unless otherwise noted, episcopal illumination with dark field contrasting was used. Objective magnifications were either 5x, 10x, 20x, or 50x. The camera adapter reduced the magnification by half. The actual magnification can be deducted from the scale bar. As an exception, the images in Chapters 5.2.3.1–5.2.3.3 were taken with a Nikon Eclipse Ni microscope with a Nikon DS-Ri2 camera.

Scanning electron microscopy was conducted on a Hitachi SU 8030. After preparation and drying, the samples were coated with a gold surface of 5 nm thickness with a Emscope SC 500 sputtering apparatus.

Melting points were measured with a Büchi B-545.

8.2 Preparation of Samples for Chapter 5

Samples for teslaphoresis were prepared as follows. Glass cover slips (22 mm × 22 mm × 0.13−0.16 mm, Menzel) were cleaned by subsequent immersion in freshly prepared piranha solution (H_2SO_4 / H_2O_2 (aq) 30 % 3:1) for 10 s, immersion and rinsing twice in Milli-Q water, immersion and rinsing in acetone and DCM and drying under either nitrogen or argon flow. A mark was drawn in one corner of the underside to indicate the direction of the electric field. The cover slips were then placed in about 3 cm distance to the antenna of the TC.

Unless otherwise noted, 20 µl of substance were transferred via EPPENDORF pipette onto the glass, and the TC switched on. When the droplet had evaporated, it was switched off again. If the time until complete evaporation was longer than 30 s, the coil was intermittently switched off and (after a cooling period) on again to avoid overheating. Solvents with evaporation times of less than 30 s were favored. The temperature of the coil was controlled via a laser thermometer, and when it surpassed 60 °C, the coil was switched off. A self-built cooling apparatus was used to radiate air onto the coil to slow the heating.

The surfaces were investigated with an optical microscope. The images of the surfaces were, unless denoted otherwise, always taken with the electric field line during the drop-casting process in the horizontal axis of the image. This is additionally illustrated by a label within the picture: “TC on” symbolizing that the TC was turned on during the drop-casting, with arrows indicating the field direction. “TC off” symbolized that the TC was turned off for comparison and control experiments.

8.3 Preparation of Samples for Chapter 6

Surfaces coated with compounds **CF3–CF10** were prepared by drop-casting. Glass cover slips (22 mm × 22 mm × 0.13−0.16 mm, Menzel) were immersed into a freshly prepared piranha solution (H_2SO_4 / H_2O_2 (aq) 30 % 3:1) for ten seconds. They were rinsed with Milli-Q water, immersed briefly in acetone and dried under ambient conditions. The solutions for drop-casting were prepared by dissolving 10 mg of the sample in 1 mL of Et_2O, followed by ultrasonication for ten minutes. Afterwards, the solutions were diluted to 5 mg mL^{-1}. Approximately 0.6 mL of the solution was transferred dropwise onto the center of a glass cover slip, enough to wet the whole surface, with the surface tension holding the liquid layer on top of the substrate. The solvent was left to evaporate under ambient conditions.

8.4 Standard Deviation

Uncertainties given in this work correspond to the standard deviation calculated by

$$SD = \sqrt{\frac{\sum_{i=1}^{n}(x_i - \overline{x})}{n-1}},$$

where n is the number of measurements, x_i are the values of the individual measurements and $\overline{x}$ the arithmetic mean of the values of one line of measurements.

8.5 Contact Angle Measurements and Fitting

Goniometric contact angle measurements were done with water on a “OCA series optical contact angle measuring and contour analysis system” by Dataphysics. Evaluation of the pictures was done with the supplied analysis software SCA 20. For static CAs, LAPLACE-YOUNG fitting was used to determine the contact angle from a digital photograph of the droplet profile and 3 µL of Milli-Q water were used. Unless otherwise noted, nine measurements were taken on three surfaces and the highest and lowest value were omitted.

For dynamic CAs, ellipse fitting was used, due to the computational effort of analyzing videos. The sessile drop (needle in) method was used. To an initial Milli-Q water droplet volume of 3 µL, water was added with a rate of 0.1 $\mu L\,s^{-1}$ until a volume of 6 µL was reached. The volume was then reduced with a rate of 0.1 $\mu L\,s^{-1}$ until the initial volume was reached. This process was recorded with 25 frames per second. CA_{max} and CA_{min} were calculated automatically. Overall three measurements were recorded for each value, on separate surfaces.

TAs were acquired by placing a scissor jack next to the analysis platform of the goniometer. A surface was placed on the intersection, so one end of the surface could be adjusted in height with the scissor jack. A droplet was placed on the surface and the height adjusted during video recording. The frame in which the droplet rolled off the surface was analyzed with ImageJ and the angle determined. The values given result from overall three measurements on separate surfaces.

8.6 Stability Testing by Water Flushing of Coated Surfaces

To test the stability of the coated surfaces, the following apparatus was used. A two-liter separation funnel was extended with an additional two-liter volume. Overall four liters of deionized water were then emptied within 57 ± 3 s onto a coated surface, which was held in place underneath by a sample holder on a wide-meshed metal net, allowing for quick draining of the water. This allowed for efficient rinsing without the build-up of a protective water layer. The height from the sample to the initial water surface was 55 cm, the opening of the separation funnel was 9 mm in diameter.

8.7 Synthetic Procedures for Chapter 5

Pyren-1-yl-carbamic acid dodecyl ester (2)

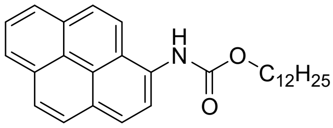

$C_{29}H_{35}NO_2$, $M_W = 429.60\,\mathrm{g\,mol^{-1}}$

1-Aminopyrene (506 mg, 2.33 mmol, 1 equiv) and 1,1′-carbonyldiimidazole (415 mg, 2.56 mmol, 1.1 equiv) were suspended in DCM (8 mL). The suspension was heated to 40 °C for 3 h. Dodecan-1-ol (868 mg, 4.66 mmol, 2 equiv) and DCM (2 mL) were added and the mixture heated to 45 °C for 16 h. TLC showed incomplete conversion and subsequently more solvent was added: DCM (10 mL), *n*-hexane (5 mL), chloroform (5 mL). Still a suspension, the mixture was heated to 45 °C for another 2 h and evaporated. DCM (100 mL) was added and the mixture was filtered. Column chromatography (*n*-hexane/DCM 1:1) yielded compound **2** (261 mg, 609 µmol, 26 %) as yellow solid.

^{1}H NMR (500 MHz, $CDCl_3$) δ = 8.52–7.95 (m, 9 H, Ar—H), 7.19 (s, 1 H, NH), 4.27 (t, J = 6.7 Hz, 2 H, OCH_2), 1.82–1.66 (m, 2 H, OCH_2CH_2), 1.63–1.13 (m, 18 H, CH_2), 0.92–0.85 (m, 3 H, CH_3).

The spectrum is in agreement with literature.[123]

Pentadecafluoro-*N*-(pyren-1-yl)octanamide (3)

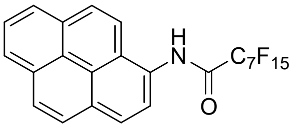

$C_{24}H_{10}F_{15}NO$, $M_W = 613.33\,\mathrm{g\,mol^{-1}}$

At 0 °C, NEt_3 (136 µL, 980 µmol, 1.40 equiv) was added to a solution of 1-aminopyrene (177 mg, 815 µmol, 1.15 equiv) in dry THF (3 mL). Pentadecafluorooctanoyl chloride (174 µL, 700 µmol, 1 equiv) was added dropwise. The mixture was stirred for 3 h at room temperature and the solvent evaporated. Filtration and thorough washing with DCM and water yielded compound **3** (416 µg, 680 µmol, 97 %) as colorless solid.

^{1}H NMR (700 MHz, $(CD_3)_2CO$) $\delta = 10.89$ (s, 1 H), 8.41–8.35 (m, 3 H), 8.31 (d, $J = 9.2$ Hz, 1 H), 8.28–8.23 (m, 3 H), 8.21 (d, $J = 8.1$ Hz, 1 H), 8.15 (t, $J = 7.6$ Hz, 1 H).

Due to poor solubility, no ^{13}C NMR was recorded.

HR-MS (ESI, pos. mode, MeCN): m/z calcd. for $C_{24}H_{10}F_{15}NO^+$ ($[M]^+$): 613.0523; found: 613.0542. m/z calcd. for $C_{24}H_{10}F_{15}NONa^+$ ($[M + Na]^+$): 636.0415; found 636.0439.

Pyren-1-yl-carbamic acid (1,1,2,2-tetrahydro)perfluorodecyl ester (4)

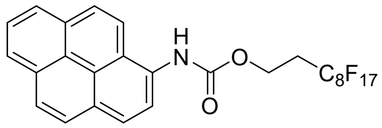

$C_{26}H_{14}F_{17}N$, $M_W = 707.38\,\mathrm{g\,mol^{-1}}$

To a solution of 1*H*,1*H*,2*H*,2*H*-perfluorodecan-1-ol (459 mg, 990 µmol, 3.1 equiv) in chloroform (5 mL), triphosgene (89.0 mg, 300 umol, 1 equiv) and pyridine (80 µL, 990 µmol, 3.1 equiv) were added. The mixture was cooled to 0 °C and let stir for 2 h. A solution of 1-aminopyrene (196 mg, 900 µmol, 3 equiv) and pyridine (85 µL, 1.05 mmol, 3.5 equiv) in chloroform (3 mL) was added dropwise at 0 °C. After 30 min, the mixture was let warm to room temperature and stirred for another 30 min. Chloroform (10 mL) and aqueous hydrochloric acid (1 M, 5 mL) were added. Because of poor solubility, more chloroform (120 mL) was added and it was washed with aqueous hydrochloric acid (1 M, 20 mL) and saturated aqueous $NaHCO_3$ (20 mL). Column chromatography yielded compound **4** (447 mg, 632 µmol, 70 %) as grayish solid.

^{1}H NMR (500 MHz, $CDCl_3$) $\delta = 8.33$ (s_{br}, 1 H), 8.22–7.92 (m, 8 H), 4.60 (t, $J = 5.9$ Hz, 2 H), 2.62 (s_{br}, 2 H).

Due to poor solubility, no ^{13}C NMR was recorded.

HR-MS (ESI, pos. mode, MeCN): m/z calcd. for $C_{27}H_{14}F_{17}NO_2Na^+$ ($[M + Na]^+$): 730.0645; found: 730.0602.

4-(N,N′-Dimethylamino)pyridinium-4-toluenesulfonate (DPTS)

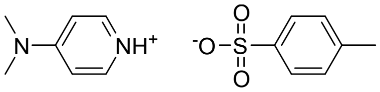

$C_{14}H_{18}N_2O_3S$, $M_W = 294.37\,\mathrm{g\,mol^{-1}}$

4-(Dimethylamino)-pyridine (3.05 g, 25.0 mmol, 1 equiv) and *p*-toluenesulfonic acid (4.75 g, 25.0 mmol, 1 equiv) were dissolved separately in THF (each 10 mL). Both solutions were combined, leading to precipitation of the crude product. Filtering and washing of the precipitate with *n*-hexane afforded DPTS (7.13 g, 24.2 mmol, 97 %) as colorless crystals.

^{1}H NMR (400 MHz, DMSO-*d6*) δ = 8.24–8.17 (m, 2 H, Ar-H), 7.53–7.45 (m, 2 H, Ar-H), 7.15–7.08 (m, 2 H, Ar-H), 7.00–6.94 (m, 2 H, Ar-H), 3.17 (s, 6 H, N(CH_3)$_2$, 2.28 (s, 3 H, Ar-CH_3).

The spectrum is in agreement with literature.[139]

Methyl 3,4,5-tris(dodecyloxy)benzoate (5)

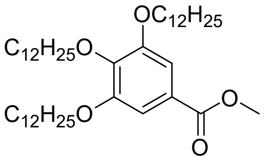

$C_{44}H_{80}O_5$, $M_W = 689.10\,\mathrm{g\,mol^{-1}}$

1-Bromododecane (7.80 mL, 32.6 mmol, 4 equiv) was added to a solution of methyl 3,4,5-trihydroxybenzoate (1.50 g, 8.14 mmol, 1 equiv), potassium carbonate (6.76 g, 48.8 mmol, 6 equiv) and 18-crown-6 (640 mg, 2.44 mmol, 0.3 equiv) in acetone (125 mL). After stirring for 18 h at 70 °C, the precipitate was filtered and dissolved in Et_2O (100 mL). After washing with a saturated, aqueous solution of sodium bicarbonate (3 × 100 mL), the organic phase was dried over magnesium sulfate and the solvent evaporated. Purification by column chromatography (SiO_2, *n*-pentane/DCM 8:1 to 1:1) afforded compound **5** (5.28 g, 7.66 mmol, 94 %) as wax-like, colorless solid.

^{1}H NMR (500 MHz, $CDCl_3$) $\delta = 7.25$ (s, 2 H, Ar-H), 4.04–3.98 (m, 6 H, OCH_2), 3.89 (s, 3 H, $COOCH_3$), 1.87–1.75 (m, 4 H, OCH_2CH_2), 1.80–1.68 (m, 2 H, OCH_2CH_2), 1.47 (tt, $J = 7.5$, 7.5 Hz, 6 H, $OCH_2CH_2CH_2$), 1.26 (s_{br}, 48 H, alkyl-H), 0.88 (t, $J = 6.9$ Hz, 9 H, alkyl-CH_3).

The spectrum is in agreement with literature.[124]

3,4,5-Tris(dodecyloxy)benzoic acid (6)

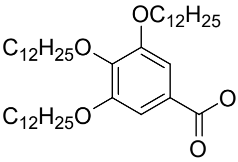

$C_{43}H_{78}O_5$, M_W = 675.08 g mol^{-1}

Without the need for inert conditions, compound **5** (4.95 g, 7.18 mmol, 1 equiv) and sodium hydroxide (3.00 g, 73.0 mmol, 10.2 equiv) were dissolved in a mixture consisting of THF (100 mL), water (100 mL) and MeOH (1 mL). After stirring for 22 h at 75 °C, the reaction mixture was acidified with aqueous hydrochloric acid (2 M, 50 mL). The aqueous residue, obtained by evaporation of the organic solvents, was extracted with DCM (3 × 100 mL). The combined organic phases were washed with aqueous hydrochloric acid (2 M, 3 × 75 mL) and dried over magnesium sulfate. Carboxylic acid **6** (4.76 g, 7.05 mmol, 98 %) was obtained as yellowish solid.

^{1}H NMR (400 MHz, $CDCl_3$) δ = 7.32 (s, 2 H, Ar-H), 4.08–3.99 (m, 6 H, OCH_2), 1.88–1.78 (m, 4 H, OCH_2CH_2), 1.78–1.70 (m, 2 H, OCH_2CH_2), 1.53–1.42 (m, 6 H, $OCH_2CH_2CH_2$), 1.40–1.20 (m, 48 H, alkyl-H), 0.94–0.82 (m, 9 H, alkyl-CH_3).

The spectrum is in agreement with literature.[124]

tert-Butyl(2-(3,4,5-tris(dodecyloxy)benzamido)-ethyl)-carbamate (7)

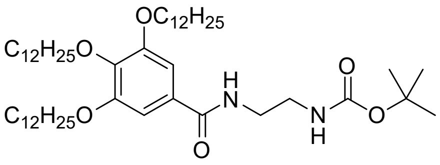

$C_{50}H_{92}N_2O_6$, $M_W = 817.28\,\mathrm{g\,mol^{-1}}$

Carboxylic acid **6** (1.40 g, 2.07 mmol, 1 equiv), EDCl (595 mg, 3.11 mmol, 1.5 equiv), DPTS (792 mg, 2.69 mmol, 1.3 equiv) and mono-BOC-protected ethane-1,2-diamine (431 mg, 2.69 mmol, 1.3 equiv) were dissolved in dry DCM (160 mL) and stirred for 16 h at room temperature. The reaction mixture was washed with aqueous hydrochloric acid (2 M, 3 × 100 mL) and dried over magnesium sulfate. Column chromatography (SiO_2, DCM to DCM/MeOH 100:2) gave compound **7** (1.52 g, 1.86 mmol, 90 %) as colorless solid.

^{1}H NMR (500 MHz, $CDCl_3$) δ = 7.05 (s, 2 H, Ar-H), 4.98 (s, 1 H, NH), 4.07–3.94 (m, 6 H, OCH_2) 3.58–3.48 (m, 2 H, $NHC\mathit{H}_2$), 3.43–3.35 (m, 2 H, $NHCH_2C\mathit{H}_2$), 1.85–1.77 (m, 4 H, $OCH_2C\mathit{H}_2$), 1.77–1.69 (m, 2 H, $OCH_2C\mathit{H}_2$), 1.51–1.43 (m, 6 H, $OCH_2CH_2C\mathit{H}_2$), 1.42 (s, 9 H, BOC-CH_3), 1.38–1.20 (m, 48 H, alkyl-H), 0.88 (t, J = 6.9 Hz, 9 H, alkyl-CH_3).

The spectrum is in agreement with literature.[124]

N-(2-Aminoethyl)-3,4,5-tris(dodecyloxy)benzamide (8)

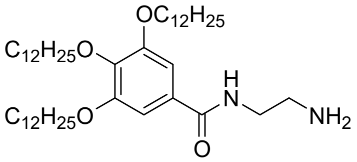

$C_{45}H_{84}N_2O_4$, M_W = 717.16 g mol^{-1}

To a solution of compound **7** (1.02 g, 1.24 mmol, 1 equiv) in chloroform (17 mL), an excess of trifluoroacetic acid (1.78 g, 15.6 mmol, 12.6 equiv) was added. After stirring for 5 h at 45 °C, the reaction mixture was neutralized with a saturated, aqueous solution of sodium bicarbonate. Drying the organic phase over magnesium sulfate and evaporation of the solvent gave primary amine **8** (0.77 g, 1.07 mmol, 86 %) as rose colored solid.

^{1}H NMR (500 MHz, $CDCl_3$) δ = 6.98 (s, 2 H, Ar-H), 6.55 (t, J = 5.0 Hz, 1 H, NH), 4.04–3.95 (m, 6 H, OCH_2), 3.48 (dt, J = 5.9, 5.9 Hz, 2 H, CONHCH_2), 2.94 (t, J = 5.9 Hz, 2 H, C$H_2$$NH_2$), 1.84–1.77 (m, 4 H, OCH_2CH_2), 1.77–1.70 (m, 2 H, OCH_2CH_2), 1.51–1.42 (m, 6 H, OCH_2CH_2CH_2), 1.40–1.19 (m, 48 H, alkyl-H), 0.88 (t, J = 6.9 Hz, 9 H, alkyl-CH_3).

The spectrum is in agreement with literature.[124]

5-Bromo-*N*-(2-(3,4,5-tris(dodecyloxy)benzamido)ethyl)-thiophene-2-carboxamide (9)

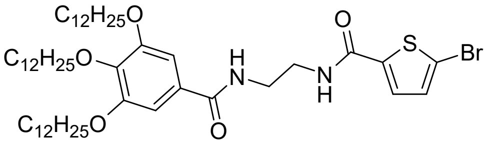

$C_{50}H_{85}BrN_2O_5S$, $M_W = 906.19\,\mathrm{g\,mol^{-1}}$

Primary amine **8** (768 mg, 1.07 mmol, 1 equiv), EDCl (308 mg, 1.60 mmol, 1.5 equiv), 5-bromothiophene-2-carboxylic acid (266 mg, 1.28 mmol, 1.2 equiv) and DPTS (409 mg, 1.39 mmol, 1.3 equiv) were dissolved in anhydrous DCM (100 mL). The reaction mixture was stirred for 19 h at room temperature. Subsequently, the reaction mixture was washed with a saturated, aqueous solution of sodium bicarbonate (3 × 100 mL). Column chromatography (SiO_2, DCM to DCM/MeOH 100:3) gave **9** (851 mg, 940 mmol, 88 %) as yellowish solid.

^{1}H NMR (500 MHz, $CDCl_3$) δ = 7.29 (s_{br}, 1 H, NH), 7.29 (d, J = 4.0 Hz, 1 H, thiophene-H), 7.08 (s_{br}, 1 H, NH), 7.01 (d, J = 4.1 Hz, 1 H, thiohene-H), 6.99 (s, 2H, Ar-H), 4.05–3.93 (m, 6 H, OCH_2), 3.67–3.60 (m, 4 H, NH(CH_2)$_2$NH), 1.85–1.76 (m, 4 H, OCH_2CH_2), 1.76–1.69 (m, 2 H, OCH_2CH_2), 1.51–1.42 (m, 6 H, $OCH_2CH_2CH_2$), 1.40–1.19 (m, 48 H, alkyl-H), 0.89 (t, J = 6.9 Hz, 9 H, alkyl-CH_3).

The spectrum is in agreement with literature.[124]

5,5′′-Bis(tributylstannyl)-2,2′:5′,2′′-terthiophene (10)

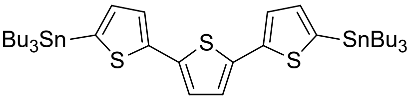

$C_{36}H_{60}S_3Sn_2$, $M_W = 826.48\,\mathrm{g\,mol^{-1}}$

5,5′′-Dibromo-2,2′:5′,2′′-terthiophene (75.4 mg, 186 µmol, 1 equiv) was dried in high vacuum and dissolved in freshly distilled THF (5 mL). At −78°, *tert*-butyllithium (480 µL, 817 µmol, 4.4 equiv) was added dropwise. After stirring at −78 °C for 2 h, tributyltin chloride (239 mg, 735 µmol, 3.96 equiv) was added *via cannula*. The mixture was slowly let to room temperature while stirring for 18 h. At 0 °C, water (2 mL) was added dropwise. The aqueous phase was extracted with Et_2O (3 × 3 mL) and the organic phase washed with water (3 × 3 mL). NMR analysis showed that product **10** (98.0 mg, 119 µmol, 63 %) was contaminated with the thiophene starting material in a ratio of 1.6 to 1. For stability reasons, and because the impurity should not impede the next reaction, and the product was processed as-is.

^{1}H NMR (500 MHz, $CDCl_3$) δ = 7.30−7.27 (m, 2 H), 7.09−7.05 (m, 4 H), 1.64−1.56 (m, 12 H), 1.39−1.32 (m, 12 H), 1.14−1.10 (m, 9 H), 0.95−0.87 (m, 12 H).

The spectrum is in agreement with literature.[134]

Oligothiophene Gelator 5TG

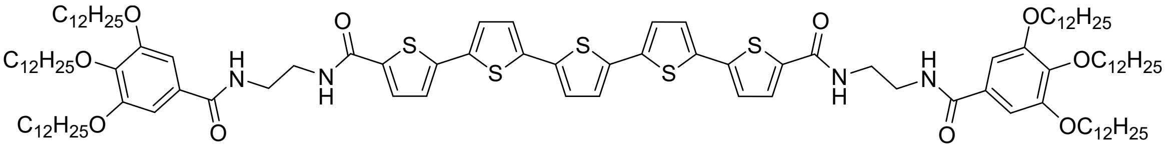

$C_{112}H_{176}N_4O_{10}S_5$, M_W = 1898.94 g mol^{-1}

Compound **9** (235 mg, 259 µmol, 2.2 equiv) was dissolved in DMF (10 mL). Terthiophene derivative **10** (157 mg, 117 µmol, 1 equiv, values calculated for the pure compound in the mixture) was purified in high vacuum and dissolved in DMF (10 mL), and added to the other solution. The mixture was degassed during three freeze-pump-thaw cycles. Tetrakis(triphenylphosphane)palladium(0) (13.6 mg, 11.7 µmol, 10 mol%) was added and the mixture heated to 100 °C for 19 h. The mixture was filtered through a short silica plug and recrystallized in chloroform/MeOH 9:1 (10 mL), affording **5TG** (131 mg, 69.0 µmol, 59 %) as orange solid.

^{1}H NMR (600 MHz, $CDCl_3/CD_3OD$ 9:1) δ = 8.19–8.10 (m, 2 H), 8.00–7.94 (m, 2 H), 7.45–7.37 (m, 2 H), 7.07–7.05 (m, 2 H), 7.04–6.97 (m, 6 H), 6.96–6.90 (m, 4 H), 3.95–3.89 (m, 8 H), 3.89–3.84 (m, 4 H), 3.52–3.41 (m, 8 H), 1.74–1.65 (m, 8 H), 1.65–1.57 (m, 4 H), 1.41–1.30 (m, 12 H), 1.29–1.04 (m, 96 H), 0.84–0.66 (m, 18 H).

NMR signals are broadened due to aggregation. The spectrum is in agreement with literature.[124]

8.8 Synthetic Procedures for Chapter 6

trans-N,N′-1,2-cyclohexanediylbis(perfluorobutanamide) (CF3)

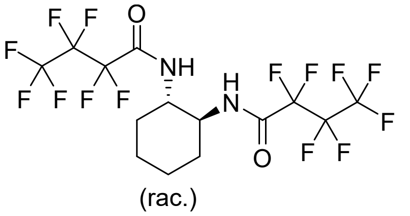

$C_{14}H_{12}F_{14}N_2O_2$, $M_W = 506.23\,\text{g mol}^{-1}$

At 0 °C, perfluorobutyryl chloride (605 mg, 2.60 mmol, 2.00 equiv) was dissolved in THF (5 mL) and added to a solution of (±)-*trans*-diaminocyclohexane (148 mg, 1.30 mmol, 1.00 equiv) and NEt_3 (0.45 mL) in THF (2.5 mL). After stirring for 30 min, the solution was heated to reflux for 3 h. After cooling to room temperature, the resulting precipitate was filtered and washed with aqueous HCl solution (0.1 M, 100 mL) and DCM (200 mL). **CF3** (398 µg, 786 µmol, 60 %) was obtained as a colorless powder.

^{1}H NMR (600 MHz, $(CD_3)_2CO$) $\delta = 8.44$ (s, 2 H), 4.03–3.92 (m, 2 H), 2.01–1.96 (m, 2 H), 1.83–1.75 (m, 2 H), 1.68–1.56 (m, 2 H), 1.41–1.31 (m, 2 H).

^{19}F NMR (565 MHz, $(CD_3)_2CO$) $\delta = -81.53$ (t, $J = 8.9$ Hz, 6 F), −120.97 to −121.11 (m, 4 F), −127.58 to −128.83 (m, 4 F).

The spectra are in agreement with literature.[7]

trans-N,N′-1,2-cyclohexanediylbis(perfluoropentanamide) (CF4)

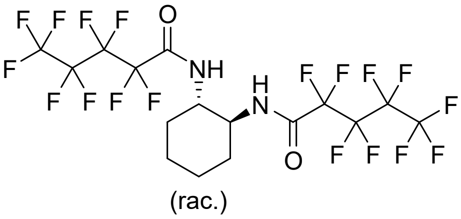

$C_{16}H_{12}F_{18}N_2O_2$, $M_W = 606.25\,\mathrm{g\,mol^{-1}}$

Nonafluorovaleric acid (687 mg, 2.60 mmol, 2.00 equiv) and an excess of thionyl chloride (5.7 mL) were stirred in THF (2.5 mL) for 30 min at room temperature. The solution was added dropwise at 0 °C to a solution of (±)-*trans*-diaminocyclohexane (148 mg, 1.30 mmol, 1.00 equiv) and NEt_3 (0.45 mL) in dry THF (3 mL) and stirred for 22 h. After washing with aqueous HCl solution (0.1 M, 100 mL) and DCM (200 mL), **CF4** (121 mg, 199 µmol, 15 %) was acquired as colorless powder.

^{1}H NMR (600 MHz, $(CD_3)_2CO$) $\delta = 8.46$ (s, 2 H), 4.03–3.93 (m, 2 H), 2.02–1.96 (m, 2 H), 1.84–1.75 (m, 2 H), 1.68–1.57 (m, 2 H), 1.42–1.30 (m, 2 H).

^{19}F NMR (565 MHz, $(CD_3)_2CO$) $\delta = -81.87$ (t, $J = 10.0$ Hz, 6 F), −120.29 (t, $J = 11.6$ Hz, 4 F), −123.92 to −124.08 (m, 4 F), −126.50 to −126.62 (m, 4 F).

The spectra are in agreement with literature.[86]

trans-*N*,*N′*-1,2-cyclohexanediylbis(perfluorohexanamide) (CF5)

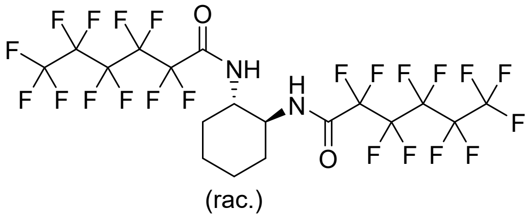

$C_{18}H_{12}F_{22}N_2O_2$, $M_W = 706.26\,\mathrm{g\,mol^{-1}}$

Undecafluorohexanoic acid (816 mg, 2.60 mmol, 2.00 equiv) and an excess of thionyl chloride (5.7 mL) were stirred in dry THF (2.5 mL) for 30 min at room temperature. Side products and excess thionyl chloride were removed in high vacuum. It was redissolved in THF (2.5 mL) and at 0 °C added dropwise to a solution of (±)-*trans*-diaminocyclohexane (148 mg, 1.30 mmol, 1.00 equiv) and NEt_3 (0.45 mL) in dry THF (3 mL). The solution was heated to reflux for 3 h. After washing with aqueous HCl solution (0.1 M, 100 mL) and DCM (200 mL), **CF5** (97.2 mg, 138 µmol, 11 %) was acquired as colorless powder.

^{1}H NMR (600 MHz, $(CD_3)_2CO$) δ = 8.45 (s, 2 H), 4.04–3.92 (m, 2 H), 2.03–1.97 (m, 2 H), 1.85–1.74 (m, 2 H), 1.69–1.57 (m, 2 H), 1.42–1.31 (m, 2 H).

^{19}F NMR (565 MHz, $(CD_3)_2CO$) δ = −81.68 (t, J = 10.0 Hz, 6 F), −119.94 to −120.24 (m, 4 F), −122.96 to −123.33 (m, 8 F), −126.71 to −126.98 (m, 4 F).

The spectra are in agreement with literature.[86]

trans-*N*,*N*′-1,2-cyclohexanediylbis(perfluoroheptanamide) (CF6)

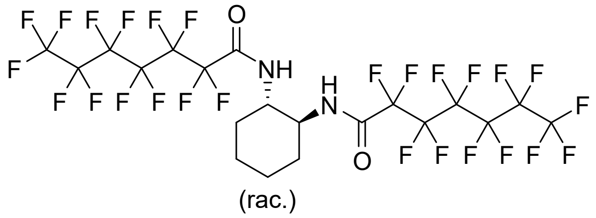

$C_{20}H_{12}F_{26}N_2O_2$, $M_W = 806.28\,\mathrm{g\,mol^{-1}}$

At 0 °C, perfluoroheptanolyl chloride (995 mg, 2.60 mmol, 2.00 equiv) was dissolved in THF (5 mL) and added to a solution of (±)-*trans*-diaminocyclohexane (148 mg, 1.30 mmol, 1.00 equiv) and NEt_3 (0.45 mL) in THF (2.5 mL). After stirring for 30 min, the solution was heated to reflux for 3 h. After cooling to room temperature, the resulting precipitate was filtered and washed with aqueous HCl solution (0.1 M, 100 mL) and DCM (200 mL). **CF6** (782 mg, 970 µmol, 75 %) was obtained as a colorless powder.

^{1}H NMR (600 MHz, $(CD_3)_2CO$) δ = 8.46 (s_{br}, 2 H), 4.03–3.95 (m, 2 H), 2.03–1.97 (m, 2 H), 1.84–1.76 (m, 2 H), 1.68–1.57 (m, 2 H), 1.42–1.31 (m, 2 H).

^{19}F NMR (565 MHz, $(CD_3)_2CO$) δ = −81.67 (t, J = 10.4 Hz, 6 F), −120.02 (dt, J = 52.5, 13.5 Hz, 4 F), −122.29 (s_{br}, 4 F), −122.91 to −123.10 (m, 4 F), −123.37 (s_{br}, 4 F), −123.75 (t, J = 14.1 Hz, 4 F).

The ^{19}F NMR is in agreement with the literature.[85]

trans-N,N′-1,2-cyclohexanediylbis(perfluorooctanamide) (CF7)

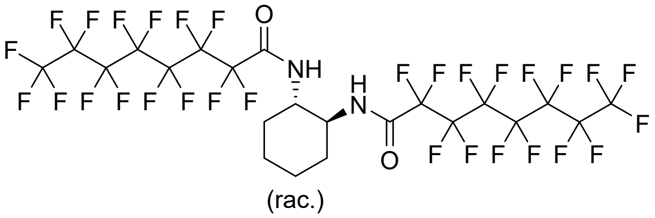

$C_{22}H_{12}F_{30}N_2O_2$, $M_W = 906.29\,\mathrm{g\,mol^{-1}}$

At 0 °C, perfluorooctanoyl chloride (2.34 g, 5.40 mmol, 2.00 equiv) was dissolved in dry THF (5 mL) and added to a solution of (±)-*trans*-diaminocyclohexane (308 mg, 2.70 mmol, 1.00 equiv) and NEt_3 (0.9 mL) in dry THF (5 mL). After stirring for 30 min, the solution was heated to reflux for 3 h. After cooling to room temperature, the resulting precipitate was filtered and washed with aqueous HCl solution (0.1 M, 100 mL) and DCM (200 mL). **CF7** (2.13 g, 2.35 µmol, 87 %) was obtained as a colorless powder.

^{1}H NMR (600 MHz, $(CD_3)_2CO$) $\delta = 8.52$ (s_{br}, 2 H), 4.07–3.98 (m, 2 H), 2.06–2.00 (m, 2 H, 1.88–1.78 (m, 2 H), 1.70–1.61 (m, 2 H), 1.42–1.37 (m, 2 H).

^{19}F NMR (565 MHz, $(CD_3)_2CO$) $\delta = -81.63$ (t, $J = 10.3$ Hz, 6 F), −119.36 to −120.64 (m, 4 F), −122.11 (s_{br}, 4 F), −122.56 (s_{br}, 4 F), −122.95 (s_{br}, 4 F), −123.26 (s_{br}, 4 F), −126.66 to −126.81 (m, 4 F).

The spectra are in agreement with literature.[7]

trans-*N*,*N′*-1,2-cyclohexanediylbis(perfluorononanamide) (CF8)

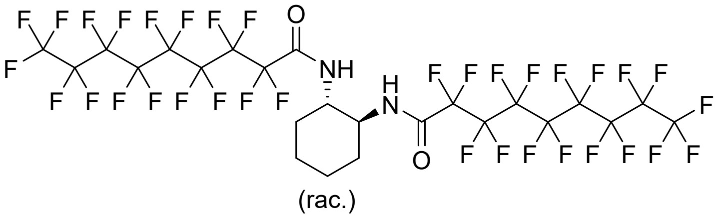

$C_{24}H_{12}F_{34}N_2O_2$, $M_W = 1006.31\,\mathrm{g\,mol^{-1}}$

At 0 °C, Perfluorononanoyl chloride (1.25 g, 2.60 mmol, 2.00 equiv) was dissolved in dry THF (2.5 mL) and added to a solution of (±)-*trans*-diaminocyclohexane (148 mg, 1.30 mmol, 1.00 equiv) and NEt_3 (0.45 mL) in dry THF (5.5 mL). After stirring for 15 min, the solution was heated to reflux for 3 h. After cooling to room temperature, the resulting precipitate was filtered and washed with aqueous HCl solution (0.1 M, 100 mL) and DCM (200 mL). **CF8** (1.07 g, 1.06 µmol, 82 %) was obtained as a colorless powder.

^{1}H NMR (600 MHz, $(CD_3)_2CO$) δ = 8.46 (s_{br}, 2 H), 4.03–3.95 (m, 2 H), 2.03–1.98 (m, 2 H, 1.84–1.75 (m, 2 H), 1.67–1.56 (m, 2 H), 1.39–1.33 (m, 2 H).

^{19}F NMR (565 MHz, $(CD_3)_2CO$) δ = −81.62 (t, J = 10.2 Hz, 6 F), −119.25 to −120.61 (m, 4 F), −122.04 (s_{br}, 4 F), −122.37 (s_{br}, 8 F), −122.81 to −122.99 (m, 4 F), −123.21 (s_{br}, 4 F), −126.62 to −126.76 (m, 4 F).

The spectra are in agreement with literature.[86]

trans-N,N′-1,2-cyclohexanediylbis(perfluorodecanamide) (CF9)

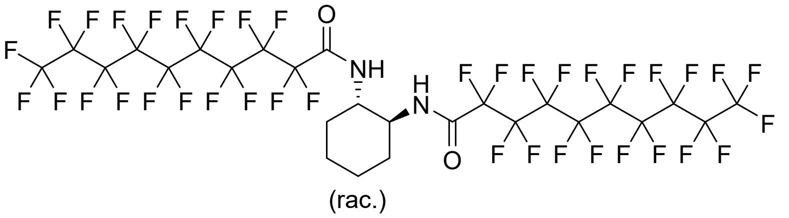

$C_{26}H_{12}F_{38}N_2O_2$, $M_W = 1106.33\,\mathrm{g\,mol^{-1}}$

Perfluorodecanoic acid (3.58 g, 6.95 mmol), pyridine (40 µL) and thionyl chloride (3.5 mL) were heated to 85 °C for 2 h without additional solvent. When cooling to room temperature, the acid chloride separated in the lower phase. The upper phase was removed with a glass pipette and the the remaining impurities evaporated in high vacuum while heating to 80 °C. The resulting perfluorodecanoic acid chloride (2.92 g, 5.48 mmol, 2.00 equiv) was dissolved in dry THF (10 mL) and, at 0 °C, added dropwise to a solution of (±)-*trans*-diaminocyclohexane (313 mg, 2.74 mmol, 1.00 equiv) and NEt_3 (0.9 mL) in dry THF (6 mL). The solution was heated to reflux for 3 h. After washing with aqueous HCl solution (0.1 м, 100 mL) and DCM (200 mL), **CF9** (1.95 g, 1.76 mmol, 64 %) was acquired as colorless powder.

^{1}H NMR (600 MHz, $(CD_3)_2CO$) δ = 8.49 (s_{br}, 2 H), 4.04–3.94 (m, 2 H), 2.00 (s, 2 H, 1.84–1.76 (m, 2 H), 1.67–1.56 (m, 2 H), 1.42–1.31 (m, 2 H).

^{19}F NMR (565 MHz, $(CD_3)_2CO$) δ = −80.64 (t, J = 9.8 Hz, 6 F), −118.13 to −119.81 (m, 4 F), −120.95 to −121.56 (m, 16 F), −121.93 (s_{br}, 4 F), −121.33 (s_{br}, 4 F), −122.25 (s_{br}, 4 F), −125.72 (s_{br}, 4 F).

The spectra are in agreement with literature.[86]

trans-N,N′-1,2-cyclohexanediylbis(perfluoroundecanamide) (CF10)

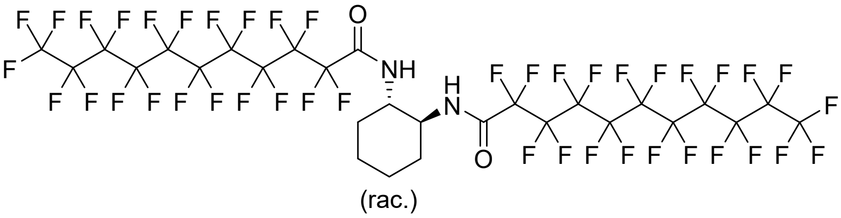

$C_{28}H_{12}F_{42}N_2O_2$, $M_W = 1206.34\,\mathrm{g\,mol^{-1}}$

Perfluoroundecanoic acid (5.26 g, 9.33 mmol), pyridine (45 µL) and thionyl chloride (4.5 mL) were heated to 85 °C for 2 h. When cooling to room temperature, the acid chloride separated in the lower phase and solidified upon cooling. The upper phase was removed with a glass pipette. The resulting perfluoroundecanoic acid chloride (3.26 g, 5.60 mmol, 2.00 equiv) was dissolved in dry THF (5 mL) and, at 0 °C, added dropwise to a solution of (±)-*trans*-diaminocyclohexane (320 mg, 2.80 mmol, 1.00 equiv) and NEt_3 (0.9 mL) in dry THF (9 mL). The solution was heated to reflux for 3 h. After washing with aqueous HCl solution (0.1 м, 100 mL) and DCM (200 mL), **CF10** (2.39 g, 1.98 mmol, 71 %) was acquired as colorless powder.

^{1}H NMR (600 MHz, $(CD_3)_2CO$) δ = 8.49 (d_{br}, J = 5.6 Hz, 2 H), 4.02–3.96 (m, 2 H), 2.00 (s, 2 H), 1.86–1.75 (m, 2 H), 1.68–1.56 (m, 2 H), 1.28 (s_{br}, 2 H).

^{19}F NMR (565 MHz, $(CD_3)_2CO$) δ = −81.00 (t, J = 9.7 Hz, 6 F), −112.82 (t, J =12.2 Hz, 4 F), −121.23 (s_{br}, 8 F), −121.79 (s_{br}, 12 F), −121.97 (s_{br}, 4 F), −122.79 (s_{br}, 4 F).

HR-MS (ESI, pos. mode, MeCN): m/z calcd. for $C_{28}H_{12}F_{42}N_2O_2Na^+$ ($[M + Na]^+$): 1229.0120; found: 1229.0131. m/z calcd. for $C_{28}H_{12}F_{42}N_2O_2K^+$ ($[M + K]^+$): 1244.9860; found 1244.9873.

Bibliography

(1) Barthlott, W.; Neinhuis, C. *Planta* **1997**, *202*, 1–8.

(2) Li, W.; Amirfazli, A. *Soft Matter* **2008**, *4*, 462–466.

(3) Shin, S.; Seo, J.; Han, H.; Kang, S.; Kim, H.; Lee, T. *Materials* **2016**, *9*, 116.

(4) Bhushan, B.; Her, E. K. *Langmuir* **2010**, *26*, 8207–8217.

(5) Feng, L.; Zhang, Y.; Xi, J.; Zhu, Y.; Wang, N.; Xia, F.; Jiang, L. *Langmuir* **2008**, *24*, 4114–4119.

(6) Bornhoeft, L. R.; Castillo, A. C.; Smalley, P. R.; Kittrell, C.; James, D. K.; Brinson, B. E.; Rybolt, T. R.; Johnson, B. R.; Cherukuri, T. K.; Cherukuri, P. *ACS Nano* **2016**, *10*, 4873–4881.

(7) Wei, Q.; Schlaich, C.; Prévost, S.; Schulz, A.; Böttcher, C.; Gradzielski, M.; Qi, Z.; Haag, R.; Schalley, C. A. *Adv. Mater.* **2014**, *26*, 7358–7364.

(8) Liu, B.; Pappas, C. G.; Ottelé, J.; Schaeffer, G.; Jurissek, C.; Pieters, P. F.; Altay, M.; Marić, I.; Stuart, M. C.; Otto, S. *J. Am. Chem. Soc.* **2020**, *142*, 4184–4192.

(9) Van der Waals, J. D., *Over de Continuiteit van den Gas-en Vloeistoftoestand*; Sijthoff: Leiden/NL, 1873.

(10) Diederich, F. *Angew. Chem. Int. Ed.* **2007**, *46*, 68–69.

(11) Rowlinson, J. *Nature* **1973**, *244*, 414–417.

(12) Fischer, E. *Ber. Dtsch. Chem. Ges* **1894**, *27*, 2985–2993.

(13) Ariga, K.; Kunitake, T., *Supramolecular Chemistry - Fundamentals and Applications*; Springer: Heidelberg, 2006.

(14) Percec, V., *Hierarchical Macromolecular Structures: 60 Years after the Staudinger Nobel Prize II*; Springer: Cham/CH, 2013.

(15) Pedersen, C. J. *J. Am. Chem. Soc.* **1967**, *89*, 7017–7036.

(16) Pedersen, C. J. *Angew. Chem. Int. Ed. Engl.* **1988**, *27*, 1021–1027.

(17) Cram, D. J.; Cram, J. M. *Science* **1974**, *183*, 803–809.

(18) Cram, D. J. *Angew. Chem. Int. Ed. Engl.* **1988**, *27*, 1009–1020.

(19) Lehn, J.-M. *Angew. Chem. Int. Ed. Engl.* **1988**, *27*, 89–112.

(20) Huang, F.; Anslyn, E. V. *Chem. Rev.* **2015**, *115*, 6999–7000.

(21) Feringa, B. L. *Angew. Chem. Int. Ed.* **2017**, *56*, 11060–11078.

(22) Sauvage, J.-P. *Angew. Chem. Int. Ed.* **2017**, *56*, 11080–11093.

(23) Stoddart, J. F. *Angew. Chem. Int. Ed.* **2017**, *56*, 11094–11125.

(24) Steed, J. W.; Turner, D. R.; Wallace, K., *Core Concepts in Supramolecular Chemistry and Nanochemistry*; John Wiley & Sons: New York/USA, 2007.

(25) Goshe, A. J.; Crowley, J. D.; Bosnich, B. *Helv. Chim. Acta* **2001**, *84*, 2971–2985.

(26) Steed, J. W. *Chem. Commun.* **2011**, *47*, 1379–1383.

(27) Wilson, K. A.; Kellie, J. L.; Wetmore, S. D. *Nucleic Acids Res.* **2014**, *42*, 6726–6741.

(28) Riley, K. E.; Hobza, P. *Acc. Chem. Res.* **2013**, *46*, 927–936.

(29) Martinez, C. R.; Iverson, B. L. *Chem. Sci.* **2012**, *3*, 2191–2201.

(30) Lewis, M.; Bagwill, C.; Hardebeck, L.; Wireduaah, S., Modern Computational Approaches to Understanding Interactions of Aromatics In *Aromatic Interactions: Frontiers in Knowledge and Application*, Johnson, D. W., Hof, F., Eds.; The Royal Society of Chemistry: Cambridge/UK, 2017, pp 1–17.

(31) Würthner, F.; Kaiser, T. E.; Saha-Möller, C. R. *Angew. Chem. Int. Ed.* **2011**, *50*, 3376–3410.

(32) Hestand, N. J.; Spano, F. C. *Chem. Rev.* **2018**, *118*, 7069–7163.

(33) Klymchenko, A. S. *J. Nanosci. Lett.* **2013**, *3*, 21.

(34) Yagai, S.; Seki, T.; Karatsu, T.; Kitamura, A.; Würthner, F. *Angew. Chem. Int. Ed.* **2008**, *47*, 3367–3371.

(35) Ziffer, M. E.; Jo, S. B.; Liu, Y.; Zhong, H.; Mohammed, J. C.; Harrison, J. S.; Jen, A. K. Y.; Ginger, D. S. *J. Phys. Chem. C* **2018**, *122*, 18860–18869.

(36) Whitesides, G. M.; Grzybowski, B. *Science* **2002**, *295*, 2418–2421.

(37) Halley, J. D.; Winkler, D. A. *Complexity* **2008**, *14*, 10–17.

(38) Israelachvili, J. N., *Intermolecular and Surface Forces*; Academic Press: Cambridge/USA, 2011, pp 415–460.

(39) Shirtcliffe, N. J.; McHale, G.; Atherton, S.; Newton, M. I. *Adv. Colloid Interface Sci.* **2010**, *161*, 124–138.

(40) Good, R. J. *J. Adhes. Sci. Technol.* **1992**, *6*, 1269–1302.

(41) Adam, N. *Nature* **1957**, *180*, 809–810.

(42) Nishino, T.; Meguro, M.; Nakamae, K.; Matsushita, M.; Ueda, Y. *Langmuir* **1999**, *15*, 4321–4323.

(43) Miwa, M.; Nakajima, A.; Fujishima, A.; Hashimoto, K.; Watanabe, T. *Langmuir* **2000**, *16*, 5754–5760.

(44) Wenzel, R. N. *J. Phys. Chem.* **1949**, *53*, 1466–1467.

(45) Cassie, A.; Baxter, S. *T. Faraday Soc.* **1944**, *40*, 546–551.

(46) Gao, L.; McCarthy, T. J. *Langmuir* **2007**, *23*, 3762–3765.

(47) McHale, G. *Langmuir* **2007**, *23*, 8200–8205.

(48) Panchagnula, M. V.; Vedantam, S. *Langmuir* **2007**, *23*, 13242–13242.

(49) Seo, K.; Kim, M., Re-Derivation of Young's Equation, Wenzel Equation, and Cassie-Baxter Equation Based on Energy Minimization In *Surface Energy*, Aliofkhazraei, M., Ed.; InTechOpen: London/UK, 2015.

(50) Huhtamäki, T.; Tian, X.; Korhonen, J. T.; Ras, R. H. *Nat. Protoc.* **2018**, *13*, 1521–1538.

(51) Fitzgibbon, A.; Pilu, M.; Fisher, R. B. *IEEE T. Pattern Anal.* **1999**, *21*, 476–480.

(52) Liu, H.; Cao, G. *Sci. Rep.* **2016**, *6*, 23936.

(53) Ibach, H., *Physics of Surfaces and Interfaces*; Springer: Heidelberg/GER, 2006.

(54) Gladysz, J. A.; Curran, D. P.; Horváth, I. T., *Handbook of Fluorous Chemistry*; John Wiley & Sons: Weinheim/GER, 2006.

(55) Kirsch, P., *Modern Fluoroorganic Chemistry*; John Wiley & Sons: New York/USA, 2013.

(56) Bondi, A. *J. Phys. Chem.* **1964**, *68*, 441–451.

(57) Dragojlovic, V. *ChemTexts* **2015**, *1*, 14.

(58) Cormanich, R. A.; O'Hagan, D.; Bühl, M. *Angew. Chem. Int. Ed.* **2017**, *56*, 7867–7870.

(59) Boese, R.; Weiss, H.-C.; Bläser, D. *Angew. Chem. Int. Ed.* **1999**, *38*, 988–992.

(60) Badea, E.; Della Gatta, G.; D'Angelo, D.; Brunetti, B.; Rečková, Z. *J. Chem. Thermodyn.* **2006**, *38*, 1546–1552.

(61) Tao, F.; Bernasek, S. L. *Chem. Rev.* **2007**, *107*, 1408–1453.

(62) Baghbanzadeh, M.; Simeone, F. C.; Bowers, C. M.; Liao, K.-C.; Thuo, M.; Baghbanzadeh, M.; Miller, M. S.; Carmichael, T. B.; Whitesides, G. M. *J. Am. Chem. Soc.* **2014**, *136*, 16919–16925.

(63) Aoki, K.; Kudo, M.; Tamaoki, N. *Org. Lett.* **2004**, *6*, 4009–4012.

(64) Majumder, D. D.; Banerjee, R.; Ulrichs, C.; Mewis, I.; Goswami, A. *IETE Tech. Rev.* **2007**, *24*, 9–25.

(65) DeFranco, J. A.; Schmidt, B. S.; Lipson, M.; Malliaras, G. G. *Org. Electron.* **2006**, *7*, 22–28.

(66) Wolfe, D. B.; Love, J. C.; Whitesides, G. M., Nanostructures Replicated by Polymer Molding In *Encyclopedia of Nanoscience and Nanotechnology*, Nalwa, H. S., Ed.; Marcel Dekker: New York/USA, 2004, pp 2657–2666.

(67) Shimizu, T. *Polym. J.* **2003**, *35*, 1–22.

(68) Ma, M.; Mao, Y.; Gupta, M.; Gleason, K. K.; Rutledge, G. C. *Macromolecules* **2005**, *38*, 9742–9748.

(69) Liu, H.; Feng, L.; Zhai, J.; Jiang, L.; Zhu, D. *Langmuir* **2004**, *20*, 5659–5661.

(70) Han, J. T.; Zheng, Y.; Cho, J. H.; Xu, X.; Cho, K. *J. Phys. Chem. B* **2005**, *109*, 20773–20778.

(71) Jisr, R. M.; Rmaile, H. H.; Schlenoff, J. B. *Angew. Chem. Int. Ed.* **2005**, *44*, 782–785.

(72) Ji, J.; Fu, J.; Shen, J. *Adv. Mater.* **2006**, *18*, 1441–1444.

(73) Hurd, A. J.; Brinker, C. J. *Mater. Res. Soc. Symp. Proc.* **1990**, *180*, 575–582.

(74) Li, X.-Q.; Stepanenko, V.; Chen, Z.; Prins, P.; Siebbeles, L. D. A.; Würthner, F. *Chem. Commun.* **2006**, 3871–3873.

(75) Yan, M.; Chen, R.; Zhang, C.; Liu, Q.; Sun, G.; Liu, J.; Yu, J.; Lin, C.; Wang, J. *ACS Appl. Mater. Interfaces* **2020**, *12*, 39807–39816.

(76) Esteves, A. C. C.; Luo, Y.; van de Put, M. W. P.; Carcouet, C. C. M.; de With, G. *Adv. Funct. Mater.* **2014**, *24*, 986–992.

(77) Mampallil, D.; Eral, H. B. *Adv. Colloid Interface Sci.* **2018**, *252*, 38–54.

(78) Alemán, J.; Chadwick, A. V.; He, J.; Hess, M.; Horie, K.; Jones, R. G.; Kratochvíl, P.; Meisel, I.; Mita, I.; Moad, G. *Pure Appl. Chem.* **2007**, *79*, 1801–1829.

(79) Flory, P. *Faraday Discuss.* **1974**, *57*, 7–18.

(80) Terech, P.; Weiss, R. G. *Chem. Rev.* **1997**, *97*, 3133–3160.

(81) Jones, C. D.; Steed, J. W. *Chem. Soc. Rev.* **2016**, *45*, 6546–6596.

(82) Yu, S.-L.; Dou, X.-Q.; Qu, D.-H.; Feng, C.-L. *J. Mol. Liq.* **2014**, *190*, 94–98.

(83) Sangeetha, N. M.; Maitra, U. *Chem. Soc. Rev.* **2005**, *34*, 821–836.

(84) Wilson, P. W.; Lu, W.; Xu, H.; Kim, P.; Kreder, M. J.; Alvarenga, J.; Aizenberg, J. *Phys. Chem. Chem. Phys.* **2013**, *15*, 581–585.

(85) Sato, H.; Yajima, T.; Yamagishi, A. *Chem. Commun.* **2011**, *47*, 3736–3738.

(86) Yajima, T.; Tabuchi, E.; Nogami, E.; Yamagishi, A.; Sato, H. *RSC Adv.* **2015**, *5*, 80542–80547.

(87) Sasaki, T.; Egami, A.; Yajima, T.; Uekusa, H.; Sato, H. *Cryst. Growth Des.* **2018**, *18*, 4200–4205.

(88) Tawfick, S.; De Volder, M.; Copic, D.; Park, S. J.; Oliver, C. R.; Polsen, E. S.; Roberts, M. J.; Hart, A. J. *Adv. Mater.* **2012**, *24*, 1628–1674.

(89) Suh, A.; Yoon, D. K. *Sci. Rep.* **2018**, *8*, 1–8.

(90) Lee, S. G.; Lim, H. S.; Lee, D. Y.; Kwak, D.; Cho, K. *Adv. Funct. Mater.* **2013**, *23*, 547–553.

(91) Lescanne, M.; Colin, A.; Mondain-Monval, O.; Heuzé, K.; Fages, F.; Pozzo, J.-L. *Langmuir* **2002**, *18*, 7151–7153.

(92) Blell, R.; Lin, X.; Lindström, T.; Ankerfors, M.; Pauly, M.; Felix, O.; Decher, G. *ACS Nano* **2016**.

(93) Shklyarevskiy, I. O.; Jonkheijm, P.; Christianen, P. C. M.; Schenning, A. P. H. J.; Del Guerzo, A.; Desvergne, J.-P.; Meijer, E. W.; Maan, J. C. *Langmuir* **2005**, *21*, 2108–2112.

(94) Otsuka, I.; Abe, H.; Sumio, O. *Sci. Technol. Adv. Mater.* **2006**, *7*, 327–331.

(95) Simon, M.; Geim, A. *J. Appl. Phys.* **2000**, *87*, 6200–6204.

(96) Yoshio, M.; Shoji, Y.; Tochigi, Y.; Nishikawa, Y.; Kato, T. *J. Am. Chem. Soc.* **2009**, *131*, 6763–6767.

(97) Wang, Y.; Du, F.; Baune, M.; Thöming, J. *Microfluid. Nanofluidics* **2014**, *17*, 499–507.

(98) Bhushan, B., *Encyclopedia of Nanotechnology*; Springer: Dordrecht/NL, 2012, pp 534–543.

(99) `https://commons.wikimedia.org/wiki/File:LC_circuit_4_times_new_version.svg` (accessed Dec. 1, 2020).

(100) Turner, R. P., *LC Circuits*; HW Sams: Carmel/USA, 1980.

(101) `http://g3ynh.info/zdocs/refs/Tesla/Johnson2001_ssTeslacoil.pdf` (accessed Nov. 30, 2020).

(102) `https://commons.wikimedia.org/wiki/File:Tesla_coil.svg` (accessed Dec. 1, 2020).

(103) Stapfner, S.; Ost, L.; Hunger, D.; Reichel, J.; Favero, I.; Weig, E. M. *Appl. Phys. Lett.* **2013**, *102*, 151910.

(104) `https://cccbdb.nist.gov/exp1x.asp` (accessed Oct. 27, 2020).

(105) Olney, T. N.; Cann, N. M.; Cooper, G.; Brion, C. E. *Chem. Phys.* **1997**, *223*, 59–98.

(106) Gussoni, M.; Rui, M.; Zerbi, G. *J. Mol. Struct.* **1998**, *447*, 163–215.

(107) Leng, Y., *Materials Characterization: Introduction to Microscopic and Spectroscopic Methods*; John Wiley & Sons: New York/USA, 2009.

(108) Zhou, W.; Apkarian, R.; Wang, Z. L.; Joy, D., Fundamentals of Scanning Electron Microscopy In *Scanning Microscopy for Nanotechnology*; Springer: Cham/CH, 2006, pp 1–40.

(109) Püspöki, Z.; Storath, M.; Sage, D.; Unser, M., Transforms and Operators for Directional Bioimage Analysis: A Survey In *Focus on Bio-Image Informatics*; Springer: Cham/CH, 2016, pp 69–93.

(110) `http://bigwww.epfl.ch/demo/orientation/` (accessed Sept. 17, 2020).

(111) Schindelin, J.; Arganda-Carreras, I.; Frise, E.; Kaynig, V.; Longair, M.; Pietzsch, T.; Preibisch, S.; Rueden, C.; Saalfeld, S.; Schmid, B. *Nat. Methods* **2012**, *9*, 676–682.

(112) Rueden, C. T.; Schindelin, J.; Hiner, M. C.; DeZonia, B. E.; Walter, A. E.; Arena, E. T.; Eliceiri, K. W. *BMC Bioinformatics* **2017**, *18*, 529.

(113) Rezakhaniha, R.; Agianniotis, A.; Schrauwen, J. T. C.; Griffa, A.; Sage, D.; Bouten, C. V. C. v.; Van De Vosse, F. N.; Unser, M.; Stergiopulos, N. *Biomech. Model. Mechan.* **2012**, *11*, 461–473.

(114) Shah, F. A.; Zanghellini, E.; Matic, A.; Thomsen, P.; Palmquist, A. *Calcified Tissue Int.* **2016**, *98*, 193–205.

(115) Leucker, K.; Schubert, D. W. *Adv. Eng. Mater.* **2019**, *22*, 1900769.

(116) Kim, K.; Sikora, A.; Nakayama, K. S.; Nakazawa, H.; Umetsu, M.; Hwang, W.; Teizer, W. *Appl. Phys. Lett.* **2014**, *105*, 143701.

(117) Bermúdez-Ureña, E.; Kilchoer, C.; Lord, N. P.; Steiner, U.; Wilts, B. D. *iScience* **2020**, *23*, 101339.

(118) Clemons, T. D.; Bradshaw, M.; Toshniwal, P.; Chaudhari, N.; Stevenson, A. W.; Lynch, J.; Fear, M. W.; Wood, F. M.; Iyer, K. S. *RSC Adv.* **2018**, *8*, 9661–9669.

(119) `https://www.gluender.de/Miscellanea/MiscTexts/UtilitiesText.html` (accessed Sept. 17, 2020).

(120) Lee, P.-W. *The Impact of Perfluorinated Chain Length on Drop Cast Supramolecular Assemblies*, Master's Thesis, Freie Universität Berlin, 2020.

(121) `https://www.amazon.com/Sunnytech-Wireless-Transmission-Experiment-Desktop/dp/B01AWARUKU` (accessed Sept. 4, 2020).

(122) `https://www.aliexpress.com/item/32748948303.html` (accessed Sept. 4, 2020).

(123) Babu, P.; Sangeetha, N. M.; Vijaykumar, P.; Maitra, U.; Rissanen, K.; Raju, A. R. *Chem. Eur. J.* **2003**, *9*, 1922–1932.

(124) Stone, D. A.; Tayi, A. S.; Goldberger, J. E.; Palmer, L. C.; Stupp, S. I. *Chem. Commun.* **2011**, *47*, 5702–5704.

(125) Kumari, N.; Naqvi, S.; Kumar, R. *J. Mater. Sci.* **2018**, *53*, 4046–4055.

(126) Hupatz, H.; Gaedke, M.; Schröder, H. V.; Beerhues, J.; Valkonen, A.; Klautzsch, F.; Müller, S.; Witte, F.; Rissanen, K.; Sarkar, B. *Beilstein J. Org. Chem.* **2020**, *16*, 2576–2588.

(127) Faghani, A.; Gholami, M. F.; Trunk, M.; Müller, J.; Pachfule, P.; Vogl, S.; Donskyi, I.; Li, M.; Nickl, P.; Shao, J. *J. Am. Chem. Soc.* **2020**, *142*, 12976–12986.

(128) Cera, L.; Chiappisi, L.; Böttcher, C.; Schulz, A.; Schoder, S.; Gradzielski, M.; Schalley, C. A. *Adv. Mater.* **2016**, *29*, 1604430.

(129) Awasthi, D.; Kumar, K.; Knudson, S. E.; Slayden, R. A.; Ojima, I. *J. Med. Chem.* **2013**, *56*, 9756–9770.

(130) Xu, L.; Chen, Y.-C.; Chong, J.; Fin, A.; McCoy, L. S.; Xu, J.; Zhang, C.; Wang, D. *Angew. Chem. Int. Ed.* **2014**, *53*, 11223–11227.

(131) Fichou, D. *J. Mater. Chem.* **2000**, *10*, 571–588.

(132) Wang, M.; Zou, S.; Guerin, G.; Shen, L.; Deng, K.; Jones, M.; Walker, G. C.; Scholes, G. D.; Winnik, M. A. *Macromolecules* **2008**, *41*, 6993–7002.

(133) Bao, Z.; Chan, W. K.; Yu, L. *J. Am. Chem. Soc.* **1995**, *117*, 12426–12435.

(134) Brotas, G.; Costa, C.; Dias, S. I. G.; Costa, P. M. M.; Di Paolo, R. E.; Martins, J.; Farinhas, J.; Alcácer, L.; Morgado, J.; Matos, M.; Charas, A. *Macromol. Chem. Phys.* **2015**, *216*, 519–529.

(135) Finsy, R. *Langmuir* **2004**, *20*, 2975–2976.

(136) Israelachvili, J. N., *Intermolecular and Surface Forces*; Academic Press: Cambridge/USA, 2011, pp 515–520.

(137) Schlaich, C. *Preparation of Superhydrophobic Surfaces by Deposition of Supramolecular Gels*, Master's Thesis, Freie Universität Berlin, 2013.

(138) Kwon, D. H.; Huh, H. K.; Lee, S. J. *Exp. Fluids* **2014**, *55*, 1691.

(139) Wu, H.; Zhu, H.; Zhuang, J.; Yang, S.; Liu, C.; Cao, Y. C. *Angew. Chem. Int. Ed.* **2008**, *47*, 3730–3734.

Appendix

ImageJ Macros for Orientation Analysis

```
var dirImg;
var nameImg;
var datapath;
var otensor = 1;

macro "Set Contrast Action Tool [1] - icon:icon_contrast.png" {
       // only for SEM: run("Smooth"); run("Smooth"); run("Smooth");
       run("Brightness/Contrast...");
       setMinAndMax(60, 255);
       run("Apply LUT");
       setMinAndMax(0, 255);
       run("Close");
}

macro "Convert to 32 bit Action Tool [2] - icon:icon_32.png" {
       run("32-bit");
}

macro "Window and Save Action Tool [3] - icon:icon_window.png" {
       //create a directory of the name of the original file
       var dirImg = getDirectory("image");
       var nameImg = getTitle();
       nameImg = replace(nameImg, ".png", "");
       // for SEM replace previous line by: nameImg = replace(nameImg, ".
          tif", "");
       var datapath = dirImg + nameImg + File.separator;
       File.makeDirectory(datapath);
       // following values need to be adjusted if picture format is
          different
       if (selectionType()==-1) {
              run("Specify...", "width=1920 height=1920 x=1280 y=960 oval
                  constrain centered");
```

```
              // for SEM, replace last line by: run("Specify...", "width=889
                  height=889 x=196 y=0 oval constrain");
       }
       run("Windowing ", "percentage_flat=90 mean=Keep embed factor_2^=0");

       saveAs("png", datapath + nameImg + "_windowed");
}

macro "Change Orientation Analysis Tensor Action Tool [4] - icon:
    icon_tensor.png" {
       otensor = getNumber("Tensor: ", otensor);
}

macro "Orientation Analysis Action Tool [5] - icon:icon_oa.png" {
       run("OrientationJ Analysis", "tensor=" + otensor + " gradient=0 color
          -survey=on hsb=on hue=Orientation sat=Coherency bri=Original-
          Image radian=on ");
       saveAs("png", datapath + nameImg + "_OA_" + otensor + "px");
}

macro "Orientation Distribution Action Tool [6] - icon:icon_od.png" {
       run("OrientationJ Distribution", "tensor=" + otensor + " gradient=0
          radian=on histogram=on table=on min-coherency=70.0 min-energy=5.0
           ");
       wait(1000);
       saveAs("Results", datapath + nameImg + "_OD_70-5-" + otensor + "
          px_values.csv");
       close();
       Plot.makeHighResolution("HR-70-5-" + otensor + "px",4.0);
       wait(1000);
       saveAs("png", datapath + nameImg + "_OD_70-5-" + otensor + "px");
}

macro "Save as PNG Action Tool [s] - icon:icon_png.png" {
       saveAs("PNG");
}

macro "Save Edited Copy of Original in Analysis Folder[d]" {
       saveAs("png", datapath + nameImg + "-edit");
}
```

Assembly Process of the TESLA Coil, First Model

Figure A1 shows photographs of the assembly process of the first model of the TC. The chronological order is from top left to bottom right. In the first picture, the use of a template (in this case the bottom of an ERLENMEYER flask) to wind the primary coil can be seen. The second picture shows the winding of the secondary coil around a hollow polycarbonate cylinder. The third picture shows the hole drilled through the baseplate and the following two pictures show the attachment of the secondary coil to this plate. The sixth picture shows the antenna (also called top load). Wire with removed isolation was attached to it with conductive aluminum adhesive tape. The primary coil was attached to the base plate, as seen in picture seven. Picture eight shows the apparatus mounted in horizontal position, with the plasma generator connected to the first coil with conductive clamps (both obscured by the coil itself). The second clamp on the primary coil could be shifted to vary the effective number of coilings for achieving better resonance.

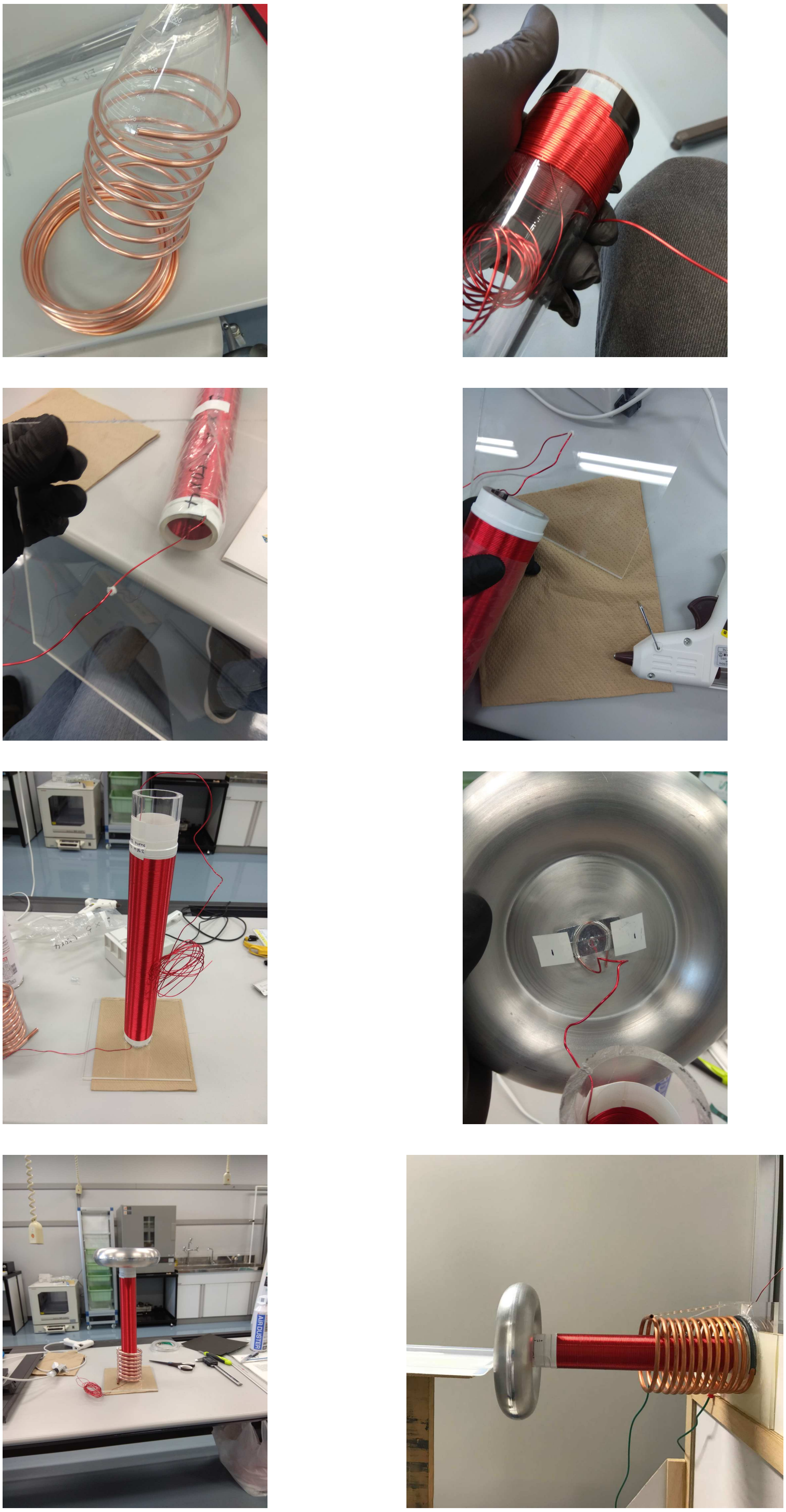

Figure A1: The assembly process of the first model of the TC.

Blueprint Tesla Coil Antenna, Second Model

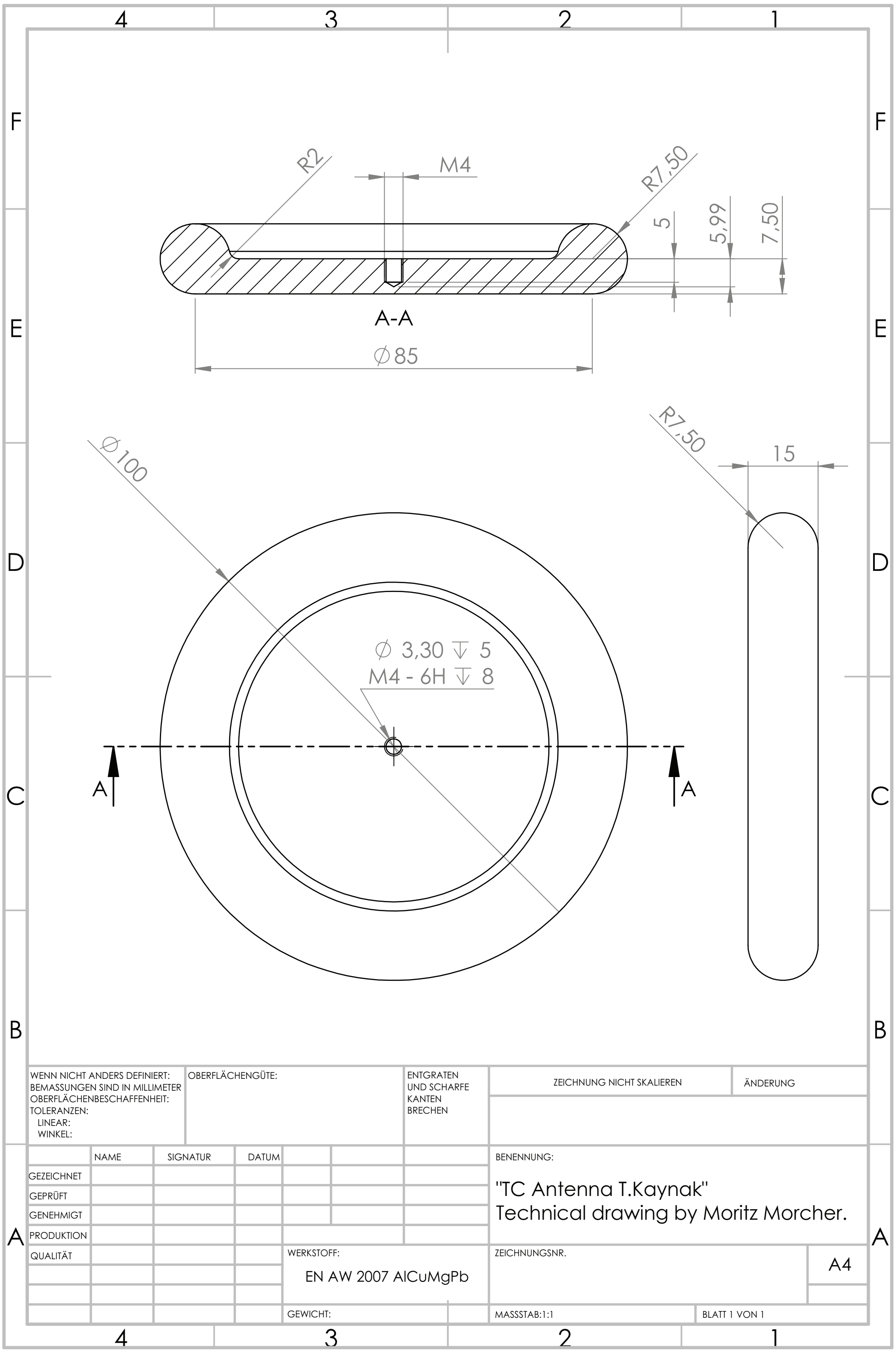

WENN NICHT ANDERS DEFINIERT:
BEMASSUNGEN SIND IN MILLIMETER
OBERFLÄCHENBESCHAFFENHEIT:
TOLERANZEN:
LINEAR:
WINKEL:

OBERFLÄCHENGÜTE:

ENTGRATEN UND SCHARFE KANTEN BRECHEN

ZEICHNUNG NICHT SKALIEREN

ÄNDERUNG

	NAME	SIGNATUR	DATUM
GEZEICHNET			
GEPRÜFT			
GENEHMIGT			
PRODUKTION			
QUALITÄT			

BENENNUNG:

"TC Antenna T.Kaynak"
Technical drawing by Moritz Morcher.

WERKSTOFF:

EN AW 2007 AlCuMgPb

ZEICHNUNGSNR.

A4

GEWICHT:

MASSSTAB:1:1

BLATT 1 VON 1